ARMY RESEARCH LABORATORY

Anisotropic Effective Moduli of Microcrack Damaged Media

by George A. Gazonas

ARL-SR-191 **January 2010**

NOTICES

Disclaimers

The findings in this report are not to be construed as an official Department of the Army position unless so designated by other authorized documents.

Citation of manufacturer's or trade names does not constitute an official endorsement or approval of the use thereof.

Destroy this report when it is no longer needed. Do not return it to the originator.

Army Research Laboratory
Aberdeen Proving Ground, MD 21005-5069

ARL-SR-191 **January 2010**

Anisotropic Effective Moduli of Microcrack Damaged Media

George A. Gazonas
Weapons and Materials Research Directorate, ARL

REPORT DOCUMENTATION PAGE

Form Approved
OMB No. 0704-0188

1. REPORT DATE *(DD-MM-YYYY)*	2. REPORT TYPE	3. DATES COVERED (From - To)
January 2010	Final	March 2006–June 2009

4. TITLE AND SUBTITLE
Anisotropic Effective Moduli of Microcrack Damaged Media

5a. CONTRACT NUMBER

5b. GRANT NUMBER

5c. PROGRAM ELEMENT NUMBER

6. AUTHOR(S)
George A. Gazonas

5d. PROJECT NUMBER
AH84

5e. TASK NUMBER

5f. WORK UNIT NUMBER

7. PERFORMING ORGANIZATION NAME(S) AND ADDRESS(ES)
U.S. Army Research Laboratory
RDRL-WMM-D
Aberdeen Proving Ground, MD 21005-5069

8. PERFORMING ORGANIZATION REPORT NUMBER
ARL-SR-191

9. SPONSORING/MONITORING AGENCY NAME(S) AND ADDRESS(ES)

10. SPONSOR/MONITOR'S ACRONYM(S)

11. SPONSOR/MONITOR'S REPORT NUMBER(S)

12. DISTRIBUTION/AVAILABILITY STATEMENT
Approved for public release; distribution is unlimited.

13. SUPPLEMENTARY NOTES

14. ABSTRACT
This report combines four recent papers related to using the generalized self-consistent method (GSCM) for determining the homogenized constitutive response of microcracked media for use in the development of multiscale constitutive models. In "The effect of crack face contact on the anisotropic effective moduli of microcrack damaged media," the GSCM is used in conjunction with a finite-element method to determine the anisotropic effective moduli of a medium containing damage consisting of microcracks with an arbitrary degree of alignment. The moduli of the medium subjected to tension, compression, and an initially stress-free state are evaluated and shown to be significantly different, affecting the wave speed (illustrated using slowness surfaces) in the damaged medium. In "An effective medium model for elastic waves in microcrack damaged media," direct numerical simulations of waves traveling in microcrack damaged media are compared to results using a homogenized effective medium calculation. In "Anisotropic effective moduli of microcracked materials under antiplane loading," the anisotropic effective moduli of a cracked solid subjected to antiplane shear deformation are analytically determined. Finally, in "On the effective electroelastic properties of microcracked generally anisotropic solids," concise expressions are derived for the effective electroelastic properties of a piezoelectric solid containing insulating, permeable, or conducting microcracks.

15. SUBJECT TERMS
generalized self-consistent method, multiscale modeling, homogenization, piezoelectric media, finite elements

16. SECURITY CLASSIFICATION OF:			17. LIMITATION OF ABSTRACT	18. NUMBER OF PAGES	19a. NAME OF RESPONSIBLE PERSON
a. REPORT	b. ABSTRACT	c. THIS PAGE			George A. Gazonas
Unclassified	Unclassified	Unclassified	UU	68	19b. TELEPHONE NUMBER (*Include area code*) 410-306-0863

Preface

This report contains reprints of four papers related to use of the generalized self-consistent method (GSCM) for determining the homogenized constitutive response of microcracked media for the development of multiscale constitutive models. In "The Effect of Crack Face Contact on the Anisotropic Effective Moduli of Microcrack Damaged Media,"[1] the GSCM is used in conjunction with a finite-element method to determine the anisotropic effective moduli of a medium containing damage consisting of microcracks with an arbitrary degree of alignment. The moduli of the medium subjected to tension, compression, and an initially stress-free state are evaluated and shown to be significantly different, affecting the wave speed (illustrated using slowness surfaces) in the damaged medium. In "An Effective Medium Model for Elastic Waves in Microcrack Damaged Media,"[2] direct numerical simulations of waves traveling in microcrack damaged media are compared to results using a homogenized effective medium calculation. For incident waves with large wavelengths (1/ka), where k is the wavenumber and a is the half-crack length, the scattered elastic energy approaches 0 and the wave does not "see" the obstacle; for crack systems modeled using the finite-element approach, this occurs for $1/ka > 60$ for media in tension and $1/ka > 10$ for those in compression. In "Anisotropic Effective Moduli of Microcracked Materials Under Antiplane Loading,"[3] the anisotropic effective moduli of a cracked solid subjected to antiplane shear deformation are analytically determined. When the undamaged solid is isotropic, the GSCM can be realized exactly; however, when the undamaged solid is anisotropic, coupled nonlinear equations for the unknown effective moduli are determined through numerical iteration. Finally, in "On the Effective Electroelastic Properties of Microcracked Generally Anisotropic Solids,"[4] concise expressions are derived for the effective electroelastic properties of a piezoelectric solid containing insulating, permeable, or conducting microcracks.

[1] Su, D.; Santare, M. H.; Gazonas, G. A. The Effect of Crack Face Contact on the Anisotropic Effective Moduli of Microcrack Damaged Media. *Engineering Fracture Mechanics* **2007**.

[2] Su, D.; Santare, M. H.; Gazonas, G. A. An Effective Medium Model for Elastic Waves in Microcrack Damaged Media. *Engineering Fracture Mechanics* **2008**.

[3] Wang, X.; Santare, M. H.; Gazonas, G. A. Anisotropic Effective Moduli of Microcracked Materials Under Antiplane Loading. *Engineering Fracture Mechanics* **2009**.

[4] Wang, X.; Gazonas, G. A.; Santare, M. H. On the Effective Electroelastic Properties of Microcracked Generally Anisotropic Solids. *Int. J. Fract*. **2009**.

Available online at www.sciencedirect.com
ScienceDirect
Engineering Fracture Mechanics 74 (2007) 1436–1455
Engineering Fracture Mechanics
www.elsevier.com/locate/engfracmech

The effect of crack face contact on the anisotropic effective moduli of microcrack damaged media

Dan Su [a], Michael H. Santare [a,*], George A. Gazonas [b]

[a] Department of Mechanical Engineering and Center for Composite Materials, University of Delaware, Newark, DE 19716, USA
[b] US Army Research Laboratory, Weapons and Materials Research Directorate, Aberdeen Proving Ground, MD 21005, USA

Received 19 March 2006; received in revised form 16 August 2006; accepted 22 August 2006
Available online 18 October 2006

Abstract

The generalized self-consistent method (GSCM) in conjunction with a computational finite element method is used to calculate the anisotropic effective moduli of a medium containing damage consisting of microcracks with an arbitrary degree of alignment. Since cracks respond differently under different external loads, the moduli of the medium subjected to tension, compression and an initially stress-free state are evaluated and shown to be significantly different, which will further affect the wave speed inside the damaged media. There are four independent material moduli for a 2-D plane stress orthotropic medium in tension or compression, and seven independent material moduli for a 2-D plane stress orthotropic cracked medium, which is initially stress free. When friction exists, it further changes the effective moduli. Numerical methods are used to take into account crack face contact and friction. The wave slowness profiles for microcrack damaged media are plotted using the predicted effective material moduli.

Keywords: Anisotropic damage; Effective moduli; Generalized self-consistent method; Microcracks

1. Introduction

Microcracking is a major cause of damage in brittle material systems, which reduces the material's effective moduli by allowing an increase in the large-scale, average deformation resulting from a given external load. As the number or size of the microcracks increase, there is a commensurate reduction in the effective stiffness, until the damage reaches a critical value causing the material to fail. A convenient way to quantify the crack density in 2-D is the parameter η [1].

$$\eta = \frac{Mc^2}{A}, \tag{1}$$

* Corresponding author. Tel.: +1 302 831 2246; fax: +1 302 831 3619.
E-mail address: santare@me.udel.edu (M.H. Santare).

0013-7944/$ - see front matter
doi:10.1016/j.engfracmech.2006.08.015

where M is the number of cracks per unit area A, and c is the average half crack length. In the general case, an ensemble of microcracks can be characterized by a distribution function, which includes the average orientation of the cracks and a description of how the crack angles are distributed around the average. This will result in anisotropic effective moduli, even when the undamaged material behaves isotropically. Since microcracks respond differently under tension and compression, damage growth and the resulting anisotropic effective moduli of microcracked media will differ depending upon the magnitude and direction of the boundary loads.

The crack-induced changes in the anisotropic effective moduli will have a profound effect on the overall structural response to loads. The prediction of these changes will help in the understanding of the anisotropic damage evolution process in brittle materials such as concrete, rock and ceramics. Indeed, continuum damage finite element modeling of the dynamic response of such brittle materials often requires, at the very least, an orthotropic description of damage in terms of three orthogonal arrays of interacting cracks [2]. The anisotropic response, is in part, a load-induced effect [3], but can also be attributed to a pre-existing preferred orientation of microcracks. In addition, the mechanical properties of microcracked media have a significant effect on wave propagation even in cases where the wavelengths are large enough to ignore wave reflection from the crack faces (see e.g. [4–6]).

Sayers et al. [7,8] used the effective moduli of the damaged media with perfectly aligned or randomly oriented cracks to study the elastic wave propagation. Schubnel and Guéguen [9] and Guéguen and Schubnel [10] calculated the elastic wave velocities and permeabilities in microcracked rocks. However, because the interactions of arbitrary orientations of cracks were not fully characterized, these authors only focused on the problems of aligned, perfectly random or specially distributed cracks, and did not consider the difference between the tensile and compressive behavior of microcracks. Therefore, further work is needed to understand the complex relationships among microcrack orientation distributions, external loads and the resulting effective moduli.

Many researchers have proposed methods to calculate the effective moduli for solids with inhomogeneities, voids or cracks. Without attempting to review the vast literature on the subject, we will focus on the studies that had the largest direct impact on the current work; the interested reader is referred to a comprehensive review of the literature provided by Kachanov [11,12]. The first solution that considered the elastic interaction of elliptically shaped cracks was by Budiansky and O'Connell [13]. In that landmark paper, they used the self-consistent method (SCM) to calculate the 3-D elastic moduli of a cracked solid, where the distribution of microcracks was assumed to be isotropic and homogeneous. In the SCM, a crack is embedded directly into an effective medium and the energy associated with opening the crack under a given load is calculated. By equating the strain energy associated with the opening of a distribution of such cracks, with the difference in strain energy between the undamaged and the effective medium, the effective moduli for the cracked medium can be calculated.

Gottesman et al. [14] used variational principles to calculate the effective elastic moduli for materials with both interacting and non-interacting parallel cracks using the SCM. These two solutions provided upper and lower bounds for the effective moduli of a medium with aligned cracks, resulting in an orthotropic effective medium as opposed to the randomly oriented cracks, which results in an isotropic effective medium. Horii and Nemat-Nasser [3] extended the Budiansky and O'Connell [13] solution, to account for crack closure and crack face friction effects. They considered load cases in which some cracks opened and some closed, and showed that when crack closure and friction are considered, the overall material response depends on load history.

Kachanov [11] provided a comprehensive review of earlier results, and compared them to analytical solutions he derived for non-interacting cracks. He noted that there are several drawbacks in the use of the SCM for determining effective moduli of cracked solids: (1) Because this method inserts the cracks directly into the effective media, the SCM over estimates the interaction between the cracks. (2) The SCM has a limiting value for crack density for randomly distributed cracks: it gives zero stiffness when the 2-D crack density η is larger than $1/\pi$.

In order to overcome these difficulties, several researchers have developed different methods for determining the effective moduli of microcracked media. Benveniste [15] extended the effective field or Mori–Tanaka method (MTM) [16] to calculate the effective moduli of 2-D cracked media. This MTM has some similarities to the SCM, but the energy is calculated based on a model of a crack in an undamaged medium subjected to an effective far-field stress or strain. The MTM predicts higher moduli than the SCM and does not predict a

limiting value for the crack density. Hashin [17] developed a differential scheme method (DSM) for elastic properties of a cracked material by following a limiting process on the DSM for porous materials. Kachanov [11] points out that the DSM is an incremental version of the SCM, which does not have a limiting crack density value, but still under-predicts the effective moduli, although not as severely as the SCM. At the same time, he notes that the DSM is path dependent, since it depends on the order in which the cracks are added to the formulation.

Aboudi and Benveniste [1] used a generalized self-consistent method (GSCM) to evaluate the 2-D effective moduli of a material with randomly oriented cracks. This method assumes that each crack resides in a region of undamaged material, which in turn is surrounded by the effective medium. The general solution for a crack inside a circular inclusion was used as the basis for this work (see Fig. 1). By using this assumption, the GSCM gives higher effective moduli than the SCM and gives non-zero stiffness at crack density $\eta = 1/\pi$. However, because of the use of a circular inclusion, the crack tip touches the inclusion-effective medium interface at $\eta = 1/\pi$. Therefore, this method can only be used for crack densities less than $1/\pi$ and becomes increasingly less accurate as the crack tip approaches the interface $\eta \to 1/\pi$. Huang et al. [18] provided a crack-elliptical matrix-composite model for the GSCM; in this improved GSCM, an elliptical inclusion is used instead of a circular inclusion, which extends the crack density limit seen in Aboudi and Benveniste [1] to a higher limiting value. The solution, however, is still only presented for a randomly oriented distribution of cracks.

The GSCM accounts for the interactions between cracks in an average sense under the assumption that each crack is surrounded by a region of intact material. Therefore, in physical situations when cracks are close together, the strong interactions between them cannot be accounted for within the framework of the GSCM. For example, Kachanov [11,12] shows that in some pre-arranged crack configurations, the crack density could become increasingly large, while having very little impact on the effective moduli. For another configuration with a very low crack density, the effective modulus can approach zero. Kachanov [11,12] points out that the limitations of the GSCM stem from the fact that this method does not permit overlap of the inclusions containing cracks. This does not preclude modeling of randomly located cracks, so long as the inclusions do not overlap, yet the maximum crack density is limited to $\eta \simeq 0.3$. In this statement, Kachanov refers to Aboudi and Benveniste [1], where the authors use a circular inclusion, which geometrically limits the crack density

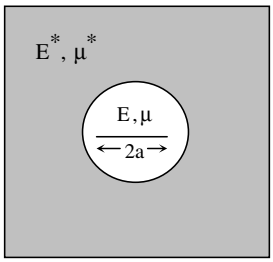

Fig. 1. GSCM model from Aboudi and Benveniste [1].

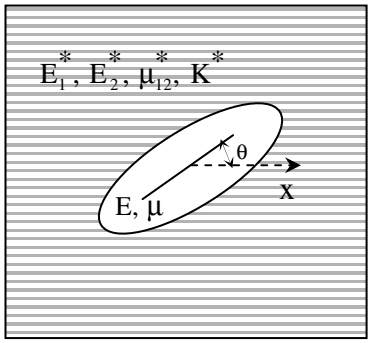

Fig. 2. Model of the crack problem from Santare et al. [19].

to $\eta = 1/\pi$ as discussed above. At this density, the crack tips touch the inclusion-matrix interface. In Huang et al. [18] and Santare et al. [19], the authors use an elliptical rather than a circular inclusion. With the elliptical inclusion this geometric limitation is eliminated and any η value can be used in the calculations. However the assumption of no overlapping between the inclusions is still present, so the model cannot account for cracks which nearly touch. Because of this, there is still a practical limitation on the value for η.

In cases where there is strong interaction among multiple cracks, the GSCM is not useful and one would need other techniques to calculate the effective moduli. Such techniques have been developed. For example, Greengard and Helsing [20] employ the fast multipole method (FMM) to evaluate the stress field of the elastic media with different inclusions; Helsing [21] applies FMM in calculating the interactions among large numbers of cracks; Wang and Chau [22] use a boundary element approach to study the effective stress intensity factor and the interaction between cracks and holes; Pan [23] derives the single domain BEM formulation to study the effect of different cracks in different size of domains; Wang and Feng [24] discuss the interaction between multiple rows of periodical cracks; Dong and Lee [25] apply the boundary integral equation method to evaluate the interaction between the doubly periodic array of cracks and their effect on the mechanical properties. These methods may be used to account for strong crack interactions resulting from high crack densities and presumably, from randomly located cracks. But the example solutions in the referenced literature still do not account for randomly located cracks. In the current paper, we show the results for crack density up to $\eta = 0.4$, which as described in Kachanov [11] "can be considered as quite high" for a 2-D problem, but seems a reasonable upper limit in light of the considerations discussed above.

In most of the above studies, the authors consider either randomly oriented cracks or aligned cracks. For randomly oriented cracks, the effective medium will be isotropic, since there is no preferred crack orientation. In the case of aligned cracks, the effective moduli will clearly be anisotropic, since the material behaves differently when the cracks are open than when they are not. In real applications, however, the orientation distribution of the cracks will be neither random nor aligned. For example, the cracks shown in Fig. 3 have an average orientation parallel to the x-axis and are distributed within $\pm\theta_0$ relative to the x-axis. In this case, crack opening will influence the moduli in all directions, but not equally. Santare et al. [19] extended Aboudi and Benveniste's [1] GSCM to study the 2-D anisotropic case where the cracks have a prescribed orientation distribution $\phi(\theta)$ (Fig. 3). They used the solution for a crack, inside an elliptical inclusion surrounded by an anisotropic effective medium (Fig. 2). Feltman and Santare [26] extended the Santare et al. [19] work to study the problem of arbitrarily oriented cracks in a material that is originally anisotropic before damage occurs.

In recent years, the research in this field has continued. Zheng and Du [27] proposed the effective self-consistent method (ESCM) and its simplified explicit version, the interaction direct derivative method (IDDM). These methods are based on an effective stress/strain field as in the MTM mentioned earlier. Feng et al. [28] proposed a quasi-micromechanical method (QMM) to calculate the overall constitutive relations for brittle materials with interacting and growing microcracks. They combined phenomenological observations with micromechanical models to realize some of the benefits from both approaches. They built the model from a micromechanical analysis while using the orientation domain of microcrack growth (DMG) from continuum damage mechanics together with the crack density parameter, to characterize the microcrack damage. In addition to these quasi-analytical studies, several authors, (see for e.g., [11,29–32]), have provided numerical solutions to determine the effective moduli in 2-D cracked media.

It is clear that a microcracked medium will behave differently in tension and compression, hence the effective anisotropic moduli of such a medium should reflect this load-induced anisotropy. Horii and Nemat-Nasser [3] discuss the response of a medium with randomly distributed cracks under overall

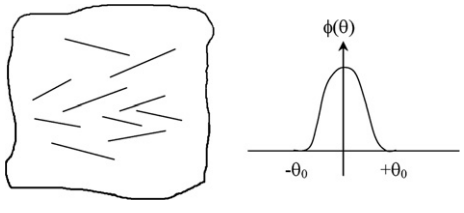

Fig. 3. Cracks distributed within $\pm\theta_0$. θ is the angle between the crack and x-axis (label the x-axis in Fig. 2).

compressive forces using the SCM. In this solution, some of the pre-existing cracks close, some open, which lead to the anisotropic response. They show the effective moduli under several different loading conditions. However, the results are limited to randomly distributed cracks and the limitations of the SCM, such as under estimating the moduli and predicting zero moduli, are still present in the results.

The problem of crack face overlap has also been recently addressed by Wang and Sun [33] in their work using boundary element methods. In the present work, we extend the GSCM developed in Santare et al. [19] and use computational finite element methods to calculate the anisotropic effective moduli for 2-D cracked media in plane stress, by considering the different behaviors of cracks in tension and compression.

2. Generalized self-consistent method for anisotropic effective media

To begin the discussion, consider the application of the GSCM to the determination of the effective moduli in a microcrack damaged solid. For a solid body containing discontinuities or voids, the total strain will be the sum of the deformation of the material itself plus the changes in the void volume. For a specific, external load, the average deformation of the material is related to the average stress and therefore can easily be found through the undamaged material's constitutive relations. To determine the change in void volume, one needs to know the initial shape and distribution of the voids. In the current model, the voids are assumed to be homogeneously distributed microcracks and the strain associated with them is therefore related to the crack opening displacements. Assuming homogeneous loading and elastic material response, the strain relationship described above can be written in terms of strain energies ([1]; see also Walsh [34] who derives a similar expression for isotropic solids using the reciprocal theorem),

$$\frac{1}{2}S^*_{ijkl}\sigma^0_{ij}\sigma^0_{ij} = \frac{1}{2}S_{ijkl}\sigma^0_{kl}\sigma^0_{ij} + \frac{1}{2V}\sum_{k=1}^{M}\int_{C_k}[u_i]t^0_i\,\mathrm{d}C_k. \tag{2}$$

In this expression, $\boldsymbol{S}^*_{ijk\ell}$ is the effective compliance of the damaged material, and $\boldsymbol{S}_{ijk\ell}$ is the compliance of the undamaged material, σ^0_{ij} is the homogeneous, applied Cauchy stress field, and

$$t^0_i = \sigma^0_{ij}n_j \tag{3}$$

is the traction that would be present along the crack faces if the material were not damaged. The term in brackets $[\boldsymbol{u}_i]$ is the crack opening displacement so that the integral in the expression, taken over the crack surface C_k of each of the M cracks in the volume V, gives the total work associated with crack opening. This integral is evaluated to take into account the crack distribution, by considering all the existing microcrack orientations, appropriately weighted. To determine "N" distinct effective moduli, "N" different homogeneous stress fields σ^0_{ij} are applied to Eq. (2), and the different forms of the equation are solved simultaneously to determine the "N" effective elastic constants (see for example [19]).

3. Crack face contact

The crack-opening energy integrals used in the previous studies are based on linear elastic fracture mechanics (LEFM), which does not explicitly account for crack face contact. Therefore, the strain energy associated with compressive loading is the same as that associated with the tensile loading due to the fact that in LEFM the crack faces overlap in compression. In reality, the crack faces will open or close depending on the applied loads, resulting in very different strain energies in tension and compression. Consider a two-dimensional plane stress orthotropic elastic material with cracks, under bi-axial loads P and P^* (Fig. 4a) and a small load increment Δq, which is not necessarily a bi-axial load.

We will discuss the following three different cases as shown in Fig. 4b. The σ_1 and σ_2 in Fig. 4b represent the principle stresses in the 2-D plane.

Case 1: $P > 0$, $P^* > 0$ and $|P| \gg |\Delta q|$, $|P^*| \gg |\Delta q|$

In this case, the pre-existing bi-axial tensile loads P and P^* are much larger than the load increment Δq. Because of this, all cracks are open and there is no crack face contact. The results in Santare et al. [19] are valid in this case.

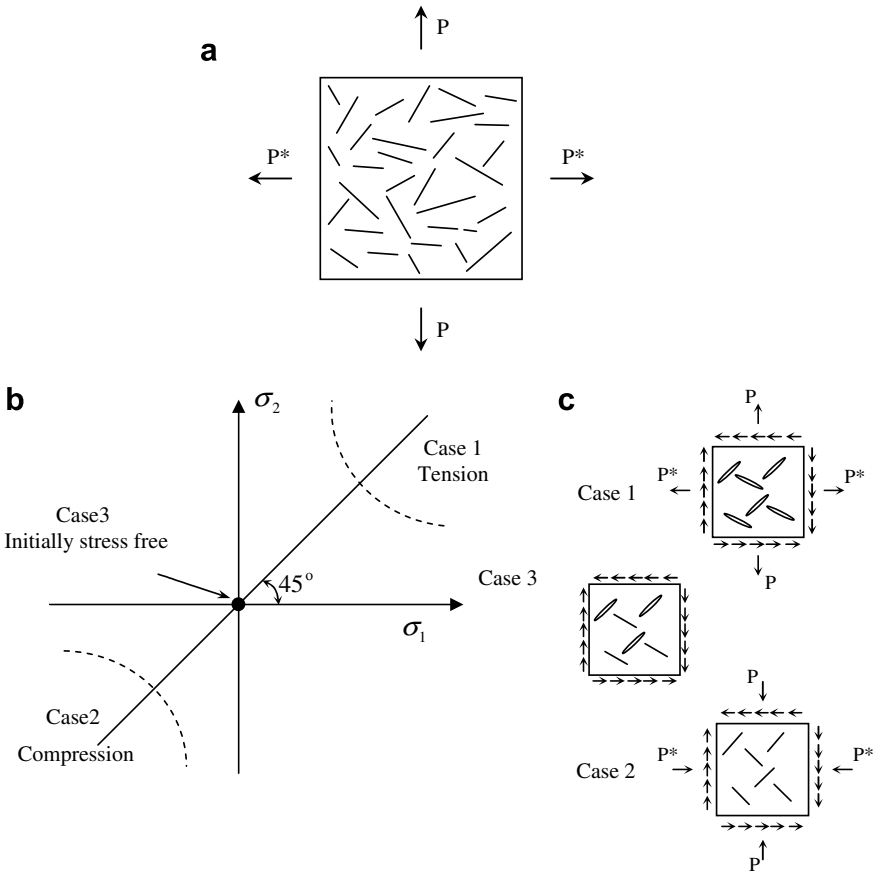

Fig. 4. (a) A cracked medium under bi-axial load. (b) Three different load cases. (c) Three cases with pure shear load increment.

Case 2: $P < 0, P^* < 0$ and $|P| \gg |\Delta q|$, $|P^*| \gg |\Delta q|$

In this case, the pre-existing bi-axial loads P and P^* are compressive and much larger than the load increment $\Delta \boldsymbol{q}$. Therefore, all cracks remain closed in mode I (normal). However the cracks may still open in mode II (shear).

Case 3: $P = P^* = 0$

The medium is initially stress free before the load increment is applied. In this case, the cracks may either open or close in both mode I and II depending on the direction of the load increments $\Delta \boldsymbol{q}$.

Fig. 4c shows schematically the cracks' response to these three cases under a pure shear load increment as an example of the $\Delta \boldsymbol{q}$. In Case 1, all the cracks open; in Case 2, all the cracks close in mode I; and in Case 3, some cracks open and some close.

For Cases 1 and 2, four independent material constants are required to fully characterize $\boldsymbol{S}^*_{ijk\ell}$ in the plane (plane stress); thus four independent load cases are needed as shown schematically in Fig. 5 (for Case 1) and Fig. 6 (for Case 2). Taking each load case separately and assuming that the undamaged material is isotropic, the following equations result [19]:

$$\frac{1}{2E_1^*}p_1^2 A = \frac{1}{2E}p_1^2 A + \frac{1}{2}\sum_{k=1}^{M}\int_{C_k}[u_i]^{p_1} t_i^{p_1}\,\mathrm{d}C_k, \tag{4}$$

$$\frac{1}{2E_2^*}p_2^2 A = \frac{1}{2E}p_2^2 A + \frac{1}{2}\sum_{k=1}^{M}\int_{C_k}[u_i]^{p_2} t_i^{p_2}\,\mathrm{d}C_k, \tag{5}$$

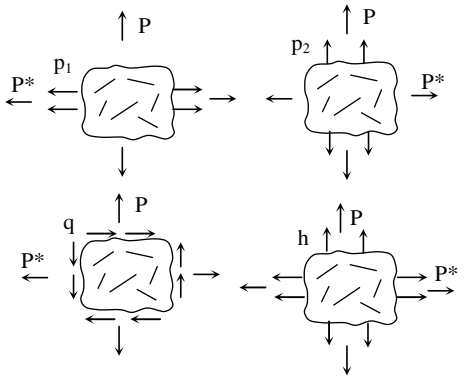

Fig. 5. Four load cases for medium in tension.

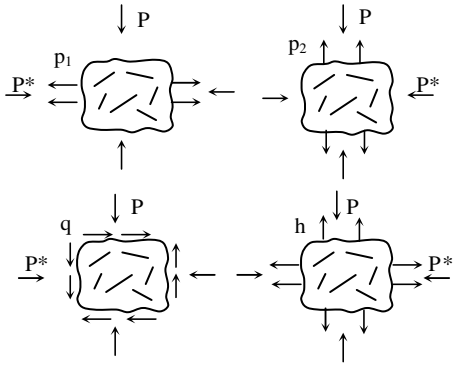

Fig. 6. Four load cases for medium in compression.

$$\frac{1}{2\mu^*}q^2A = \frac{1}{2\mu}q^2A + \frac{1}{2}\sum_{k=1}^{M}\int_{C_k}[u_i]^q t_i^q \,\mathrm{d}C_k, \tag{6}$$

$$\frac{1}{2K^*}h^2A = \frac{1}{2K}h^2A + \frac{1}{2}\sum_{k=1}^{M}\int_{C_k}[u_i]^h t_i^h \,\mathrm{d}C_k. \tag{7}$$

In these equations, p_1, p_2, q and h are the homogeneous load increments as shown in Figs. 5 and 6. E_1^*, E_2^*, μ^* and K^* are the effective moduli of the damaged material. E_1^* and E_2^* are the elastic moduli in the principal directions, μ^*, is the shear modulus, and K^* is the effective 2-D plane stress bulk modulus. These moduli are related to Poisson's ratio through the equation [19],

$$K^* = \frac{E_1^* E_2^*}{E_1^* + E_2^*(1 - 2v_1^*)}, \tag{8}$$

where v_1^* is one of the effective Poisson's ratios of the damaged material. $\boldsymbol{E}$, μ and $\boldsymbol{K}$ are the undamaged material moduli where $\boldsymbol{K}$ is analogous to $\boldsymbol{K}^*$ for the case of an isotropic material.

In Case 3, the cracked medium responds differently under tensile and compressive loads, hence there will be different Young's moduli, and bulk moduli under tension and compression (Fig. 7). We assume the crack distribution is symmetric with respect to the x-axis. Therefore, when we shear the medium relative to this axis, half of the cracks will open and half will close in mode I (as depicted in Fig. 4c), so there is only one effective shear modulus μ^* in Case 3. Seven independent material constants are thus required to describe this 2-D orthotropic plane stress model

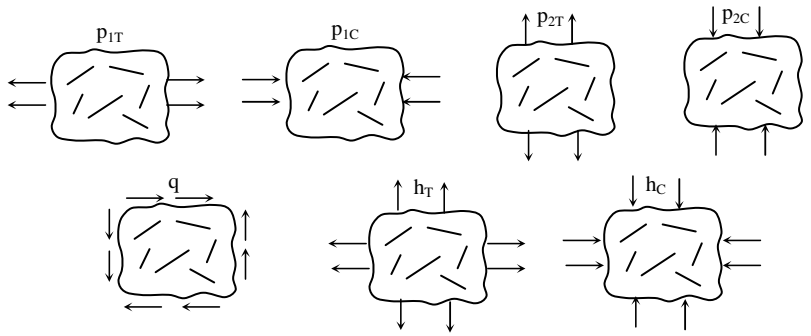

Fig. 7. Seven load cases for an initially stress-free medium.

$$\frac{1}{2E^*_{1T}}p^2_{1T}A = \frac{1}{2E}p^2_{1T}A + \frac{1}{2}\sum_{k=1}^{M}\int_{C_k}[u_i]^{p_{1T}}t_i^{p_{1T}}\,dC_k, \tag{9}$$

$$\frac{1}{2E^*_{1C}}p^2_{1C}A = \frac{1}{2E}p^2_{1C}A + \frac{1}{2}\sum_{k=1}^{M}\int_{C_k}[u_i]^{p_{1C}}t_i^{p_{1C}}\,dC_k, \tag{10}$$

$$\frac{1}{2E^*_{2T}}p^2_{2T}A = \frac{1}{2E}p^2_{2T}A + \frac{1}{2}\sum_{k=1}^{M}\int_{C_k}[u_i]^{p_{2T}}t_i^{p_{2T}}\,dC_k, \tag{11}$$

$$\frac{1}{2E^*_{2C}}p^2_{2C}A = \frac{1}{2E}p^2_{2C}A + \frac{1}{2}\sum_{k=1}^{M}\int_{C_k}[u_i]^{p_{2C}}t_i^{p_{2C}}\,dC_k, \tag{12}$$

$$\frac{1}{2\mu^*}q^2A = \frac{1}{2\mu}q^2A + \frac{1}{2}\sum_{k=1}^{M}\int_{C_k}[u_i]^{q}t_i^{q}\,dC_k, \tag{13}$$

$$\frac{1}{2K^*_{T}}h^2_{T}A = \frac{1}{2K}h^2_{T}A + \frac{1}{2}\sum_{k=1}^{M}\int_{C_k}[u_i]^{h_T}t_i^{h_T}\,dC_k, \tag{14}$$

$$\frac{1}{2K^*_{C}}h^2_{C}A = \frac{1}{2K}h^2_{C}A + \frac{1}{2}\sum_{k=1}^{M}\int_{C_k}[u_i]^{h_C}t_i^{h_C}\,dC_k. \tag{15}$$

In these equations, p_{1T}, p_{1C}, p_{2T}, p_{2C}, q, h_T, h_C represent the homogeneous load increments shown in Fig. 7. E^*_{1T} and E^*_{2T} are the effective Young's moduli under tensile load, and E^*_{1C}, E^*_{2C} are the effective Young's moduli under compressive load. K^*_T, K^*_C are the effective 2-D plane stress bulk moduli under tensile and compressive loads. By generalizing the results of Taya and Mura [35] and Feltman and Santare [26], they can be written as

$$K^*_T = \frac{E^*_{1T}E^*_{2T}}{E^*_{1T} + E^*_{2T}(1-2v^*_{12T})}, \tag{16}$$

$$K^*_C = \frac{E^*_{1C}E^*_{2C}}{E^*_{1C} + E^*_{2C}(1-2v^*_{12C})}, \tag{17}$$

where v^*_{12T} represents the effective Poisson's ratios of the damaged material under tensile loads, and v^*_{12C} is for compressive loads.

4. Finite element model

The results in Santare et al. [19] are valid only for Case 1, as discussed in the previous section. In that case, the crack surfaces will never overlap due to the applied bi-axial tensile loads. In order to prevent the unphysical crack face overlap under compression loads in LEFM, and discuss other cases mentioned in previous section, we have developed a finite element model to calculate the energy associated with the crack opening

displacements. Nonlinear contact elements are used along the crack surfaces, so that overlap is eliminated, and crack face friction can be added easily.

The finite element model was designed to mimic as closely as possible the analytical boundary value problem used in the GSCM. This model is shown schematically in Fig. 8. The use of finite elements introduces several new issues. For example, the analytical solution domain used in GSCM is an infinite medium. To simulate this using an FE model we need a large enough domain so that the embedded crack does not interact with the external boundary. However, the larger the model, the more calculation time needed to converge to a set of effective moduli. A second issue is the interface between the ellipse and the surrounding medium. In the FE model, the mesh needs to be sufficiently refined to simulate the smooth elliptical interface in the analytical solution. A comprehensive meshing study was undertaken and the numerical results were compared to known analytical solutions [36] to resolve these domain size and finite element mesh refinement issues.

The resulting FE model is constructed with 2-D plane stress, isoparametric elements. As in the analytical solution, the material inside the ellipse is isotropic and homogeneous and the material outside is a homogeneous orthotropic effective material with a known principal axis orientation. Note that in Fig. 8, the crack shown is horizontal. In order to calculate the crack opening displacement for cracks at other angles, we simply modify the externally applied loads as calculated from Mohr's circle. The external boundary length of the FE model is $L = 500$ and the focal length of the ellipse equals the half crack length $c = 30$. In order to model a specific crack density η, the crack length is kept constant, and the size of the ellipse is varied. By using Eq. (1), together with the geometrical relations for an ellipse, $A = \pi ab$ and $c^2 = a^2 - b^2$, we can determine a unique a and b, the semi-major and semi-minor axes of the ellipse for a given η. For the results that follow, the FE model has 31,882 elements in the entire 2-D plane stress model, with 4054 elements inside the ellipse when $\eta = 0.4$.

The effective moduli for the cracked media are obtained using the FE solutions for the crack energies in the method described in Section 2 and 3. We use ABAQUS 6.4.4 [37] as the FE solver and the program is written in the ABAQUS script language Python. For the initially stress-free case (Case 3), we wrote a user subroutine to define a new 2-D material with seven material constants. On a PC with a Pentium 4 2.0 GHz cpu and 1 GB RAM, it took from 30 min to 3 h for a single iteration with a specific η and θ_0, depending on the number of unknown material properties (4 for Cases 1 and 2 and 7 for Case 3), whether the friction existed and whether we used the user defined material. There are about 5–15 iterations in a "typical" solution, when we use the virgin material properties as the initial guess.

To describe the algorithm of the FE script, consider the medium in tension (Case 1) as an example. Let us assume that the crack distribution function is $\phi(\theta)$ and the individual crack angles are distributed in the interval $[-\theta_0, \theta_0]$ relative to the x-axis. With this, we can replace the summations in Eqs. (4)–(7) with the following integrals (adapted from [19]):

$$\frac{1}{2E_1^*}p_1^2 = \frac{1}{2E}p_1^2 + \frac{1}{4}\frac{\eta}{c^2\theta_0}\int_{-\theta_0}^{\theta_0}\phi(\theta)\int_{C_k}[u_i]^{p_1}t_i^{p_1}\,\mathrm{d}C_k\,\mathrm{d}\theta, \tag{18}$$

$$\frac{1}{2E_2^*}p_2^2 = \frac{1}{2E}p_2^2 + \frac{1}{4}\frac{\eta}{c^2\theta_0}\int_{-\theta_0}^{\theta_0}\phi(\theta)\int_{C_k}[u_i]^{p_2}t_i^{p_2}\,\mathrm{d}C_k\,\mathrm{d}\theta, \tag{19}$$

$$\frac{1}{2\mu^*}q^2 = \frac{1}{2\mu}q^2 + \frac{1}{4}\frac{\eta}{c^2\theta_0}\int_{-\theta_0}^{\theta_0}\phi(\theta)\int_{C_k}[u_i]^{q}t_i^{q}\,\mathrm{d}C_k\,\mathrm{d}\theta, \tag{20}$$

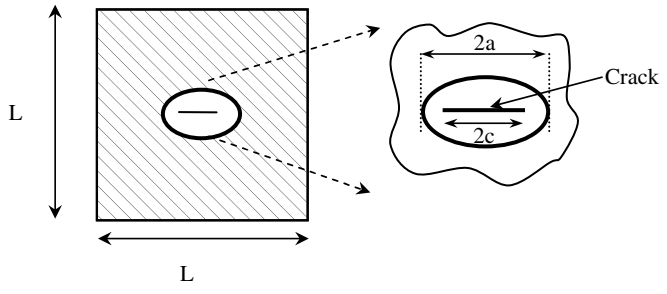

Fig. 8. FEM model for single crack inside an elliptical inclusion.

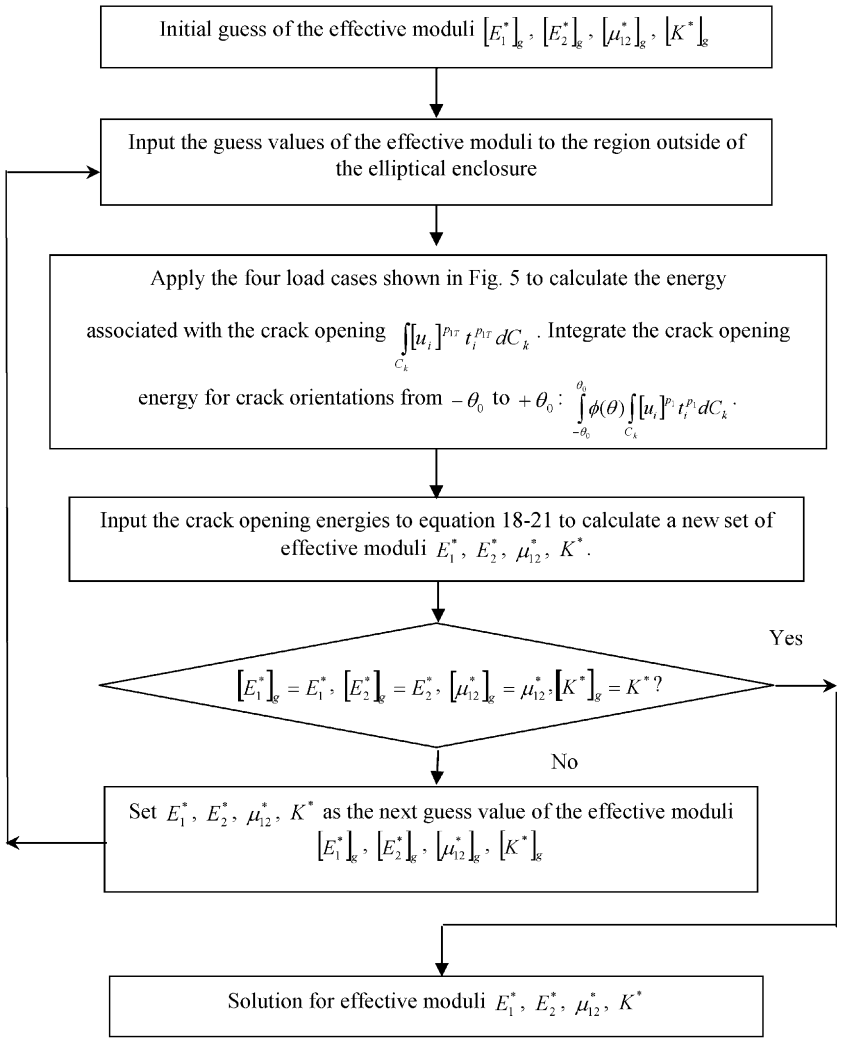

Fig. 9. Flow chart for calculating effective moduli of the medium in tension.

$$\frac{1}{2K^*}h^2 = \frac{1}{2K}h^2 + \frac{1}{4}\frac{\eta}{c^2\theta_0}\int_{-\theta_0}^{\theta_0}\phi(\theta)\int_{C_k}[u_i]^h t_i^h \,\mathrm{d}C_k\,\mathrm{d}\theta. \tag{21}$$

Fig. 9 is a flow chart of the algorithm used for calculating the effective moduli of the medium in tension. The quantities assumed known, are the crack density, η (hence the elliptical geometry and crack length) the undamaged material moduli E, μ and K and the crack orientation distribution, $\phi(\theta)$, and range $[-\theta_0, \theta_0]$. An initial guess is made for the four effective moduli in the surrounding matrix. By applying these and the traction boundary conditions to the model as shown in Fig. 5, we calculate the crack opening displacement $[u_i]$ in each load case for the full range of crack orientations considered. These displacements allow us to approximate the double integrals in Eqs. (18)–(21). We can then use these four equations to calculate a new set of the four effective moduli E_1^*, E_2^*, μ^* and K^*. These new moduli are then compared to the initial estimates to determine if another iteration is necessary to converge within a user-defined level of accuracy.

5. Computational results

As discussed before, different crack distribution functions $\phi(\theta)$ will result in different orthotropic effective moduli. In the following solutions, we choose $\phi(\theta)$ to be a constant distribution between $[-\theta_0, \theta_0]$ as shown in

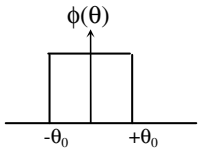

Fig. 10. Constant distribution of cracks.

Fig. 10. This is chosen so that when $\theta_0 = 90$, the cracks are randomly distributed as is the case in most of the literature. Other distributions could be used simply by inputting the proper function into Eqs. (18)–(21). We assume that the intact Poisson's ratio is 1/3 and that the crack tips are placed at the foci of the ellipse in Fig. 8.

In the tables, we list the results for the effective moduli for all three load cases described in Section 3. The effective moduli for the medium in tension (Case 1) are all within 4% relative error when compared to the results in Santare et al. [19]. This verifies that the FE model developed approximates the analytical solution to within an acceptable level of accuracy when all the cracks are open. In Figs. 11 and 12, we compare our current results with several classic results for the effective moduli of cracked media in 2-D plane stress models. Fig. 11 is the effective Young's modulus for the medium with randomly distributed cracks ($\theta_0 = 90$) and Fig. 12 shows the effective Young's modulus in the direction perpendicular to an aligned array of cracks ($\theta_0 = 0$).

As discussed above, in a 2-D orthotropic plane stress model, four material moduli (Cases 1 and 2) or seven material moduli (Case 3) are required to fully define the material compliance. In plane stress, the mechanical properties in the out-of-plane direction are uncoupled from those in the in-plane directions and are therefore completely arbitrary.

However, in the literature, many authors predict the effective moduli for the cracked medium using a 2-D plane strain model. In plane strain, the out-of-plane compliances affect the in-plane moduli. Yet, many authors do not report the mechanical properties in the out-of-plane direction, and this makes it difficult to compare our result to theirs. Alternatively, it is possible to use the current procedure, along with an assumed set of out-of-plane properties, to generate an analogous set of plane strain results.

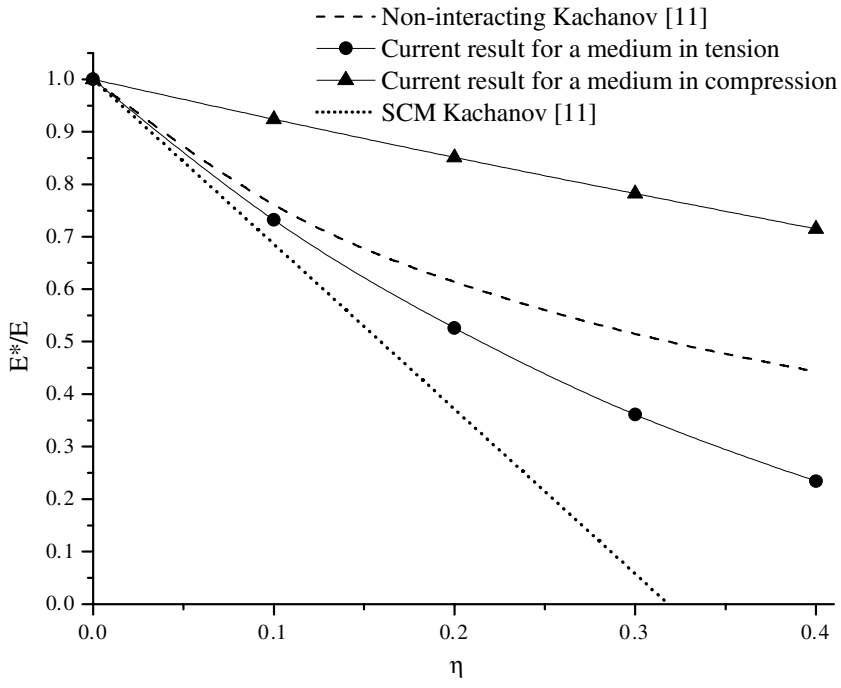

Fig. 11. Normalized effective Young's modulus for randomly distributed cracks vs. crack density.

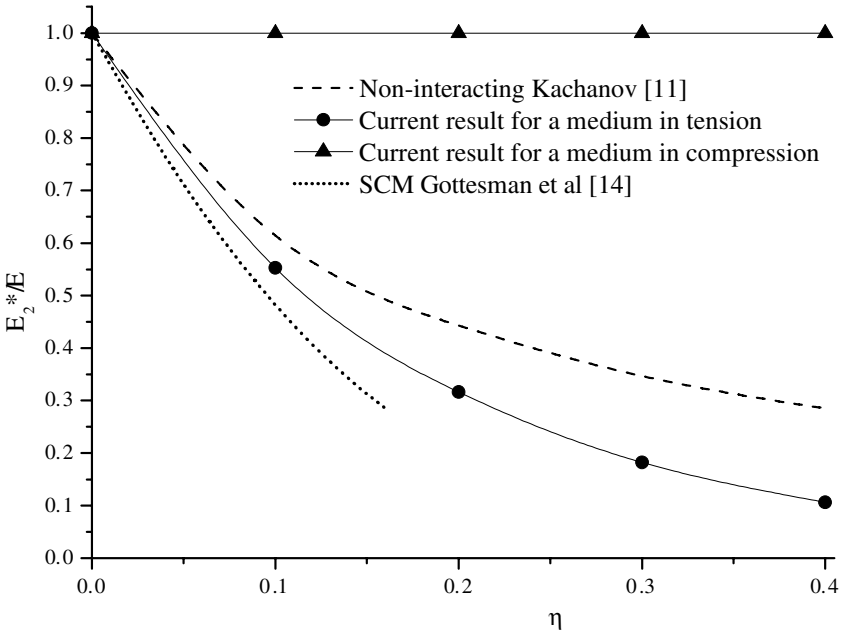

Fig. 12. Normalized effective Young's modulus, in the direction perpendicular to the cracks, for aligned cracks vs. crack density.

The data in Tables 1–4 are plotted in a series of contour plots (Figs. 13–15) to facilitate visualization and comparison. In each contour plot, the horizontal axes are the limits of the orientation distribution, θ_0 from 0° to 90° and the crack density, η from 0 to 0.4. The vertical axis is the effective modulus normalized by the corresponding undamaged modulus. Figs. 13 and 14 show the moduli for the medium in tension (Case 1) and compression (Case 2). Comparing Fig. 13 with Fig. 14, we see that the medium is generally stiffer under compressive loads than under tensile loads. This is because the cracks can only experience mode II (shear) opening under compressive loads and therefore the energy dissipated through crack opening is smaller than that under tensile loads where modes I and II are both possible. As shown in Fig. 14, the 2-D effective bulk modulus is unchanged under compressive loads. This is due to the fact that when the medium is loaded in bi-axial compression, all the cracks will be closed (in both normal and shear modes).

Fig. 15 shows how the effective moduli of the initially stress-free medium (Case 3) vary with θ_0 and η. In this figure, when $\theta_0 = 90°$, the crack orientations are random and therefore the medium is isotropic. The classical relationship among isotropic material moduli is shown as

$$\mu = \frac{E}{2(1+v)}. \tag{22}$$

However, the effective properties in Fig. 15 do not satisfy Eq. (22). In an isotropic medium, where the tensile properties are different from the compressive properties, the following relationship can be easily derived:

$$\mu = \frac{E_C E_T}{E_C(1+v_T) + E_T(1+v_C)}, \tag{23}$$

where E_C, E_T are Young's moduli under tensile and compressive loads and v_T, v_C are Poisson's ratios in these two load cases. In this case, the Poisson's ratios in Eq. (23) can be calculated from the 2-D bulk moduli and Young's moduli through the following relations:

$$K_T = \frac{E_T}{2(1-v_T)}, \tag{24}$$

$$K_C = \frac{E_C}{2(1-v_C)}, \tag{25}$$

Eqs. (24) and (25) are the isotropic versions of Eqs. (16) and (17).

Table 1
Effective moduli of a medium in tension

θ_0	E_1^*/E	E_2^*/E	μ_{12}^*/μ	K^*/K	θ_0	E_1^*/E	E_2^*/E	μ_{12}^*/μ	K^*/K
$\eta = 0.1$					$\eta = 0.2$				
0	1.000	0.553	0.796	0.623	0	1.000	0.316	0.633	0.381
10	0.993	0.556	0.795	0.623	10	0.985	0.319	0.632	0.382
20	0.974	0.566	0.795	0.625	20	0.944	0.328	0.630	0.384
30	0.944	0.581	0.794	0.627	30	0.883	0.344	0.628	0.388
40	0.907	0.601	0.794	0.629	40	0.812	0.366	0.626	0.391
50	0.866	0.626	0.793	0.631	50	0.739	0.393	0.624	0.395
60	0.826	0.653	0.793	0.633	60	0.670	0.424	0.624	0.397
70	0.789	0.681	0.793	0.634	70	0.611	0.459	0.624	0.399
80	0.758	0.708	0.794	0.634	80	0.562	0.494	0.625	0.400
90	0.732	0.732	0.794	0.634	90	0.526	0.526	0.626	0.400
$\eta = 0.3$					$\eta = 0.4$				
0	1.000	0.182	0.502	0.228	0	1.000	0.106	0.398	0.137
10	0.976	0.184	0.500	0.229	10	0.965	0.108	0.395	0.138
20	0.910	0.191	0.496	0.231	20	0.870	0.113	0.388	0.139
30	0.816	0.203	0.491	0.234	30	0.740	0.120	0.380	0.140
40	0.711	0.220	0.486	0.237	40	0.611	0.131	0.372	0.140
50	0.611	0.242	0.482	0.239	50	0.484	0.145	0.366	0.139
60	0.523	0.268	0.481	0.240	60	0.387	0.163	0.364	0.138
70	0.452	0.298	0.481	0.240	70	0.316	0.184	0.364	0.137
80	0.399	0.330	0.483	0.241	80	0.266	0.208	0.366	0.136
90	0.361	0.361	0.485	0.241	90	0.234	0.234	0.368	0.136

Table 2
Effective moduli of a medium in compression

θ_0	E_1^*/E	E_2^*/E	μ_{12}^*/μ	K^*/K	θ_0	E_1^*/E	E_2^*/E	μ_{12}^*/μ	K^*/K
$\eta = 0.1$					$\eta = 0.2$				
0	1.000	1.000	0.797	1.000	0	1.000	1.000	0.639	1.000
10	0.994	0.994	0.804	1.000	10	0.987	0.987	0.650	1.000
20	0.977	0.977	0.823	1.000	20	0.953	0.953	0.680	1.000
30	0.955	0.955	0.850	1.000	30	0.909	0.909	0.724	1.000
40	0.933	0.933	0.878	1.000	40	0.868	0.868	0.772	1.000
50	0.917	0.917	0.900	1.000	50	0.838	0.838	0.810	1.000
60	0.909	0.909	0.911	1.000	60	0.824	0.824	0.830	1.000
70	0.910	0.910	0.911	1.000	70	0.825	0.825	0.828	1.000
80	0.916	0.916	0.902	1.000	80	0.836	0.836	0.813	1.000
90	0.924	0.924	0.890	1.000	90	0.851	0.851	0.793	1.000
$\eta = 0.3$					$\eta = 0.4$				
0	1.000	1.000	0.516	1.000	0	1.000	1.000	0.418	1.000
10	0.980	0.980	0.528	1.000	10	0.973	0.973	0.432	1.000
20	0.929	0.929	0.564	1.000	20	0.903	0.903	0.470	1.000
30	0.864	0.864	0.618	1.000	30	0.819	0.819	0.528	1.000
40	0.805	0.805	0.677	1.000	40	0.745	0.745	0.595	1.000
50	0.764	0.764	0.728	1.000	50	0.693	0.693	0.653	1.000
60	0.744	0.744	0.754	1.000	60	0.670	0.670	0.684	1.000
70	0.745	0.745	0.752	1.000	70	0.671	0.671	0.682	1.000
80	0.761	0.761	0.731	1.000	80	0.690	0.690	0.657	1.000
90	0.782	0.782	0.705	1.000	90	0.715	0.715	0.626	1.000

When friction is present on the crack surfaces, the moduli become path and load dependent. This is because the friction force is a non-conservative force, and therefore the work of friction depends on the sequence of

Table 3
Effective moduli of initially stress-free media

θ_0	E^*_{1T}/E	E^*_{1C}/E	E^*_{2T}/E	E^*_{2C}/E	μ^*_{12}/μ	K^*_t/K	K^*_c/K	θ_0	E^*_{1T}/E	E^*_{1C}/E	E^*_{2T}/E	E^*_{2C}/E	μ^*_{12}/μ	K^*_t/K	K^*_c/K
$\eta = 0.1$								$\eta = 0.2$							
0	1.000	1.000	0.553	1.000	0.796	0.623	1.000	0	1.000	1.000	0.316	1.000	0.634	0.381	1.000
10	0.993	0.994	0.556	0.994	0.799	0.623	1.000	10	0.986	0.987	0.319	0.987	0.640	0.382	1.000
20	0.975	0.977	0.565	0.977	0.809	0.625	1.000	20	0.947	0.953	0.328	0.953	0.654	0.385	1.000
30	0.946	0.954	0.580	0.954	0.821	0.627	1.000	30	0.889	0.909	0.344	0.909	0.673	0.389	1.000
40	0.910	0.933	0.600	0.933	0.834	0.629	1.000	40	0.821	0.867	0.366	0.867	0.693	0.394	1.000
50	0.871	0.917	0.624	0.917	0.844	0.632	1.000	50	0.749	0.837	0.393	0.837	0.708	0.398	1.000
60	0.831	0.909	0.651	0.909	0.849	0.633	1.000	60	0.681	0.823	0.424	0.823	0.716	0.401	1.000
70	0.793	0.910	0.679	0.910	0.849	0.635	1.000	70	0.620	0.823	0.459	0.823	0.715	0.403	1.000
80	0.760	0.916	0.707	0.916	0.845	0.635	1.000	80	0.570	0.835	0.496	0.835	0.709	0.404	1.000
90	0.733	0.924	0.733	0.924	0.840	0.635	1.000	90	0.530	0.850	0.530	0.850	0.701	0.404	1.000
$\eta = 0.3$								$\eta = 0.4$							
0	1.000	1.000	0.182	1.000	0.505	0.228	1.000	0	1.000	1.000	0.107	1.000	0.402	0.137	1.000
10	0.978	0.980	0.184	0.980	0.511	0.230	1.000	10	0.968	0.973	0.108	0.973	0.408	0.138	1.000
20	0.916	0.928	0.192	0.928	0.526	0.233	1.000	20	0.880	0.902	0.114	0.902	0.423	0.141	1.000
30	0.828	0.863	0.205	0.863	0.547	0.237	1.000	30	0.761	0.816	0.122	0.816	0.443	0.144	1.000
40	0.728	0.803	0.222	0.803	0.569	0.241	1.000	40	0.632	0.739	0.134	0.739	0.463	0.146	1.000
50	0.630	0.760	0.244	0.760	0.586	0.245	1.000	50	0.514	0.686	0.149	0.686	0.478	0.147	1.000
60	0.542	0.740	0.271	0.740	0.595	0.247	1.000	60	0.415	0.661	0.168	0.661	0.486	0.146	1.000
70	0.469	0.741	0.302	0.741	0.594	0.248	1.000	70	0.339	0.662	0.191	0.662	0.485	0.145	1.000
80	0.412	0.756	0.336	0.756	0.587	0.248	1.000	80	0.283	0.680	0.217	0.680	0.479	0.144	1.000
90	0.370	0.777	0.370	0.777	0.578	0.248	1.000	90	0.246	0.706	0.245	0.706	0.470	0.143	1.000

Table 4
Effective moduli of initially stress-free media with friction coefficient equal to 0.2

θ_0	E^*_{1T}/E	E^*_{1C}/E	E^*_{2T}/E	E^*_{2C}/E	μ^*_{12}/μ	K^*_t/K	K^*_c/K	θ_0	E^*_{1T}/E	E^*_{1C}/E	E^*_{2T}/E	E^*_{2C}/E	μ^*_{12}/μ	K^*_t/K	K^*_c/K
$\eta = 0.1$								$\eta = 0.2$							
0	1.000	1.000	0.553	1.000	0.796	0.623	1.000	0	1.000	1.000	0.316	1.000	0.634	0.381	1.000
10	0.993	0.994	0.556	1.000	0.802	0.623	1.000	10	0.986	0.987	0.319	1.000	0.644	0.382	1.000
20	0.975	0.978	0.565	0.994	0.814	0.625	1.000	20	0.947	0.955	0.329	0.988	0.661	0.385	1.000
30	0.946	0.958	0.580	0.978	0.828	0.627	1.000	30	0.890	0.915	0.344	0.955	0.683	0.390	1.000
40	0.910	0.940	0.600	0.959	0.841	0.629	1.000	40	0.821	0.880	0.366	0.917	0.703	0.394	1.000
50	0.871	0.928	0.624	0.943	0.850	0.632	1.000	50	0.750	0.857	0.393	0.886	0.717	0.399	1.000
60	0.831	0.924	0.651	0.934	0.855	0.634	1.000	60	0.681	0.850	0.425	0.868	0.725	0.402	1.000
70	0.793	0.928	0.680	0.932	0.855	0.635	1.000	70	0.621	0.856	0.460	0.864	0.725	0.404	1.000
80	0.760	0.935	0.708	0.936	0.851	0.635	1.000	80	0.570	0.869	0.496	0.871	0.720	0.405	1.000
90	0.733	0.942	0.733	0.942	0.846	0.635	1.000	90	0.531	0.883	0.531	0.883	0.711	0.405	1.000
$\eta = 0.3$								$\eta = 0.4$							
0	1.000	1.000	0.182	1.000	0.505	0.229	1.000	0	1.000	1.000	0.107	1.000	0.413	0.138	1.000
10	0.978	0.980	0.184	1.000	0.515	0.230	1.000	10	0.968	0.972	0.109	1.000	0.418	0.139	1.000
20	0.916	0.930	0.192	0.981	0.535	0.233	1.000	20	0.881	0.904	0.114	0.974	0.436	0.141	1.000
30	0.828	0.871	0.205	0.931	0.559	0.238	1.000	30	0.762	0.824	0.123	0.905	0.458	0.144	1.000
40	0.729	0.819	0.222	0.874	0.581	0.242	1.000	40	0.634	0.758	0.135	0.828	0.479	0.147	1.000
50	0.631	0.786	0.245	0.827	0.597	0.245	1.000	50	0.515	0.716	0.150	0.768	0.493	0.147	1.000
60	0.543	0.775	0.272	0.801	0.606	0.248	1.000	60	0.417	0.703	0.169	0.735	0.501	0.147	1.000
70	0.470	0.784	0.303	0.796	0.606	0.249	1.000	70	0.340	0.713	0.192	0.728	0.501	0.146	1.000
80	0.413	0.804	0.337	0.806	0.600	0.249	1.000	80	0.285	0.738	0.219	0.742	0.495	0.145	1.000
90	0.371	0.824	0.371	0.824	0.589	0.248	1.000	90	0.247	0.764	0.247	0.764	0.486	0.144	1.000

loading. To simplify the current discussion, here we will only consider the initially stress-free medium with the external loads applied proportionally.

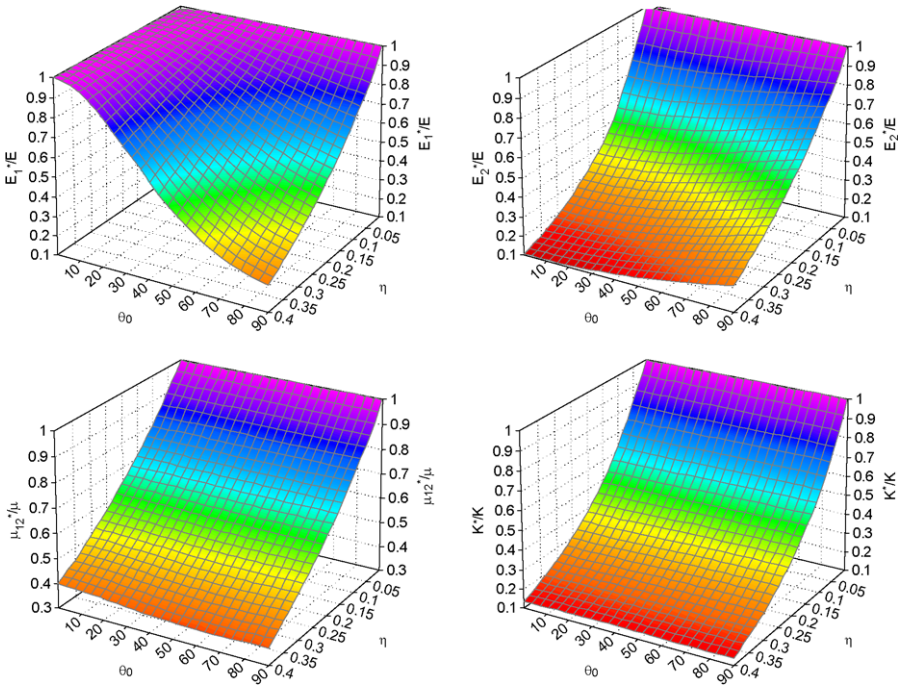

Fig. 13. Effective moduli of a medium in tension.

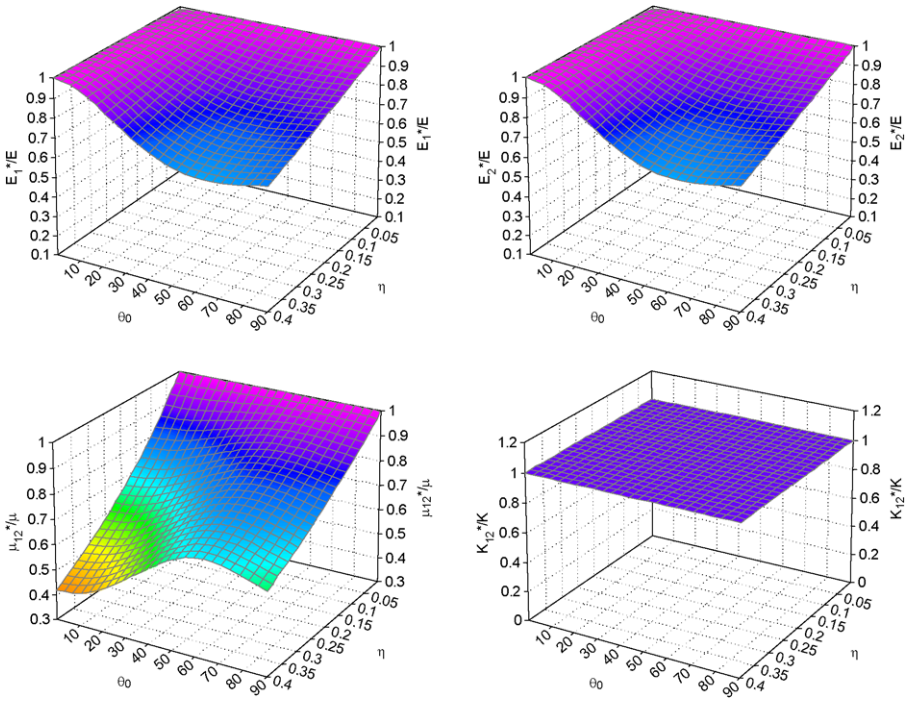

Fig. 14. Effective moduli of a medium in compression.

Fig. 16 shows the comparison of normalized effective Young's moduli for the initially stress-free media with and without friction under compressive load. The crack density $\eta = 0.4$, and in the friction case, the friction

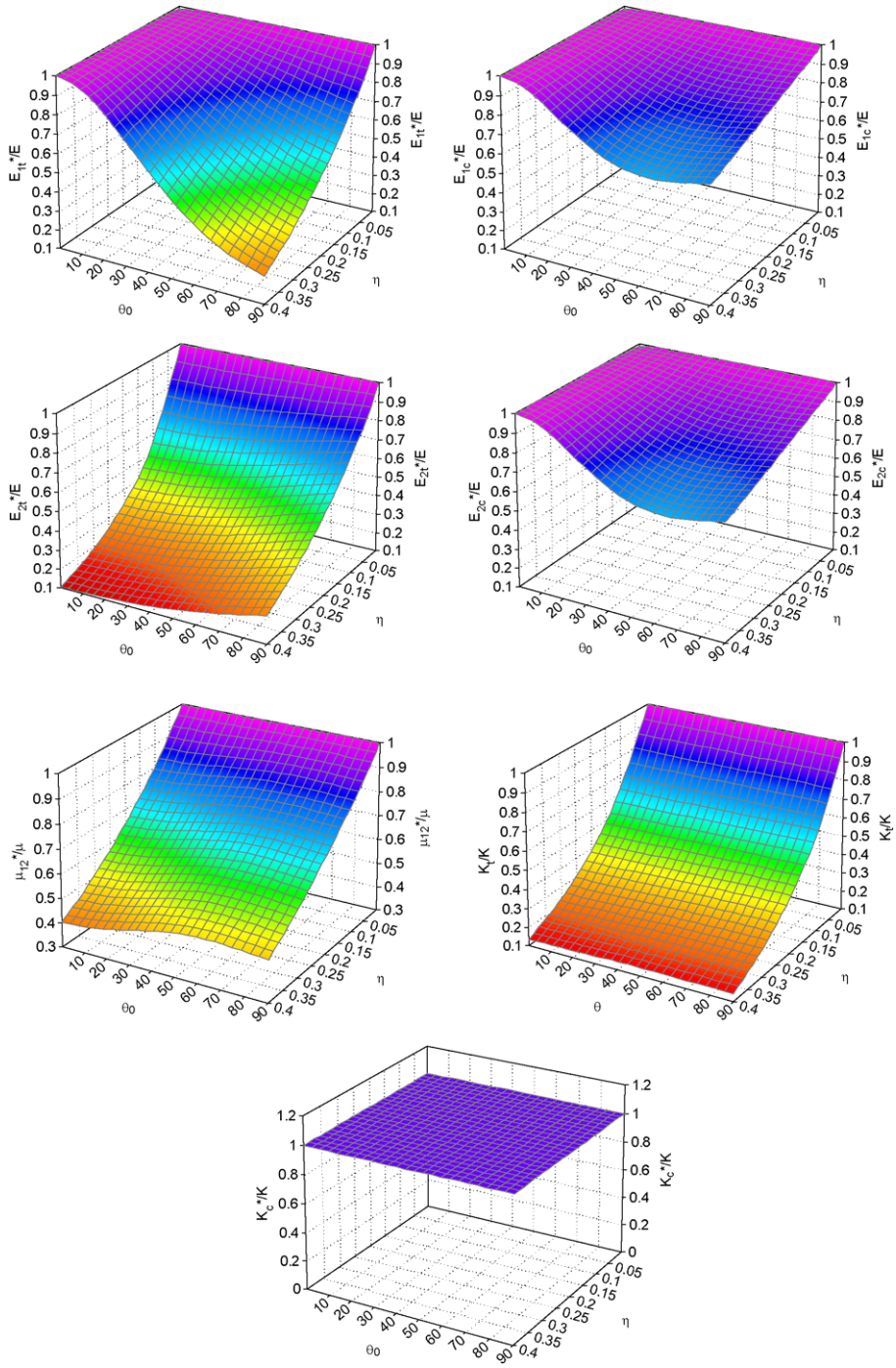

Fig. 15. Effective moduli of an initially stress-free medium.

coefficient is equal to 0.2. We can see that the friction affects to the Young's moduli under compressive loads. When $\eta = 0.4$, E^*_{1C} and E^*_{2C} increase about 8% when the friction exists. Also, we see that there is a clear "flat zone" ($E^*_{2C}/E = 1$) for E^*_{2C} when $\theta_0 < 11°$. This is because the friction prevents the cracks from opening in any mode under this situation. The maximum extent of the "flat zone" is determined by the friction coefficient.

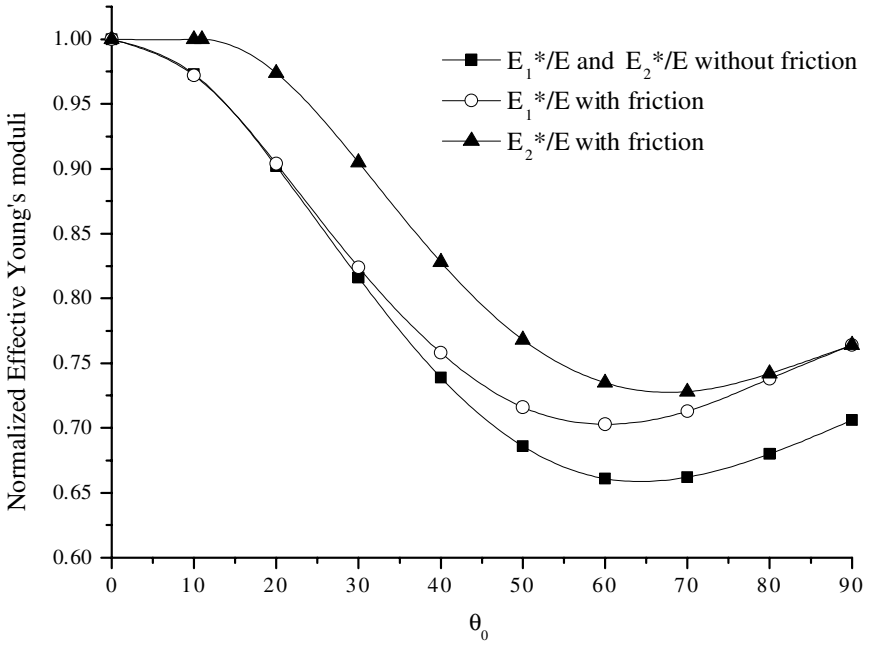

Fig. 16. Normalized E^*_{1C}, E^*_{2C} of initially stress-free media with and without friction. $\eta = 0.4$ and the friction coefficient equal to 0.2.

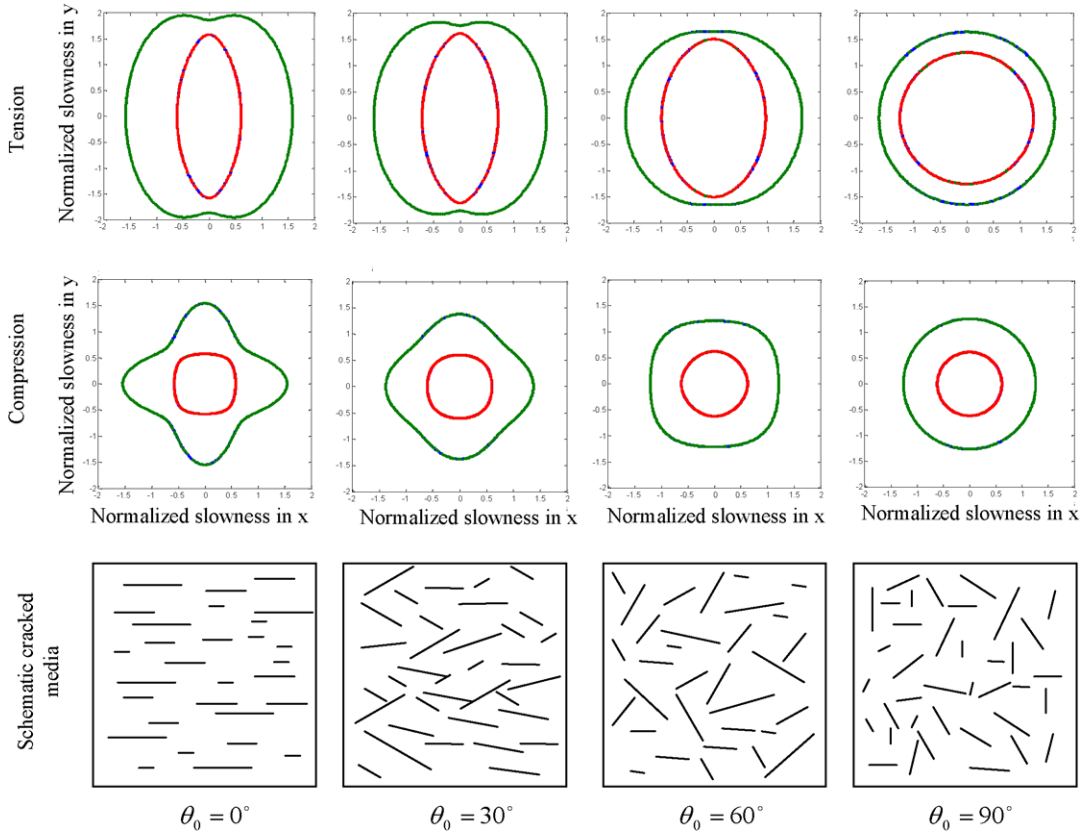

Fig. 17. Normalized slowness of cracked media under tension and compression. Crack density $\eta = 0.4$. Outside lines: quasi-transverse wave; inside lines: quasi-longitudinal wave. All the lines are normalized by the slowness of transverse wave in virgin material.

6. Wave propagation in microcrack damaged media

When applying the predicted effective moduli to the wave equation, we can predict the elastic wave speed within the cracked media. To find out the wave speed of a plane harmonic wave in the **L** direction, we need to solve the following eigenvalue equation [38]:

$$\det\{A_{ij} - \delta_{ij}\rho v^2\} = 0, \tag{26}$$

in which, $\mathbf{A} = \mathbf{L}^{\mathrm{T}}\mathbf{C}\mathbf{L}$ is the acoustic tensor, $\mathbf{C}$ is the elastic tensor and $\mathbf{L}$ is a 3×2 direction cosine matrix.

$$[\mathbf{L}] = \begin{bmatrix} l_1 & 0 \\ 0 & l_2 \\ l_2 & l_1 \end{bmatrix}. \tag{27}$$

The slowness is the inverse of wave speed

$$\mathbf{S}^{(i)}(\mathbf{l}) = \frac{\mathbf{l}}{v^{(i)}}. \tag{28}$$

Fig. 17 shows the normalized slowness (inverse of the wave speed) in the media with cracks in tension and compression. The outside lines depict curves of maximum slowness (quasi-transverse wave) and the inside lines depict curves of minimum slowness (quasi-longitudinal wave). The figures on the first line are the media under tensile loads (Case 1 in Fig. 4b) and the figures on the second line are the media under compressive loads (Case 2 in Fig. 4b). Comparing the figures in the same column, we can see that for identical crack distributions and densities, the wave speed (slowness) profiles are very different under different loads.

7. Conclusions

In this study, a finite element model was used to solve the analytical crack-inclusion anisotropic boundary value problem used in the GSCM. The analytical results of Santare et al. [19] were used to validate the finite element model within a 4% relative error (Case 1), which confirms the accuracy of the model. Using the same basic FE model, contact elements were introduced to eliminate the crack surface overlap, which occurs under compression in linear elastic fracture mechanics. With this model, we calculated effective moduli for a damaged medium under tensile, compressive, and initially stress-free conditions. Base on the effective moduli, we also predict the elastic wave slowness within the 2-D cracked media.

Generally speaking, the results show that the existence of microcracks decreases the effective stiffness of the medium and the effective moduli further decrease as the microcrack density is increased. The crack orientation distribution also has a significant effect on the anisotropy of the effective moduli which can vary from highly anisotropic when the cracks are unidirectional ($\theta_0 = 0°$) to isotropic when they are randomly distributed ($\theta_0 = 90°$). Furthermore, we see that the damaged medium responds quite differently depending on whether the external loads are tension, compression or initially zero. And we see that the medium is much stiffer when the overall external loads are compressive.

We have described how, in an initially stress-free medium under 2-D plane stress loading, there are seven independent orthotropic effective material properties for the microcracked medium (Case 3); for randomly distributed microcracks, the number of independent moduli are reduced to four, and satisfy Eq. (23). We have also shown how friction can be introduced into the model, and that in general, friction makes the medium stiffer particularly under compression loads. From the literature [3] we know that the moduli become path and load dependent when crack face friction is included in the analysis, and to adequately account for these effects, further study is required.

Finally, we plot wave slowness profiles for microcrack damaged media and show that for media with identical microcrack densities and distributions the wave speeds are very different under tensile and compressive loads, because of the different effective moduli for these two load cases.

Acknowledgement

This research was supported by the United States Army Research Laboratory through the Composite Materials Technology cooperative in agreement with the Center for Composite Materials at the University of Delaware.

References

[1] Aboudi J, Benveniste Y. The effective moduli of cracked bodies in plane deformations. Engng Fract Mech 1987;26(2):171–84.
[2] Fahrenthold EP. A continuum damage model for fracture of brittle solids under dynamic loading. Trans ASME 1991;58: 904–9.
[3] Horii H, Nemat-Nasser S. Overall moduli of solid with microcracks: load-induced anisotropy. J Mech Phys Solids 1983;31(2): 155–71.
[4] Bayuk IO, Kalinin VA. Elastic anisotropy of rocks 2. An oriented system of cracks of arbitrary concentration. Phys Solid Earth 1995;31(3):194–200.
[5] Monsen K. Acoustic velocity in fractured rock. J Geophys Res 2001;106(B7):13261–7.
[6] Liu E, Hudson JA, Pointer T. Equivalent medium representation of fractured rock. J Geophys Res 2000;105(B2):2981–3000.
[7] Sayers CM, van Munster JG. Microcrack-induced seismic anisotropy of sedimentary rocks. J Geophys Res 1991;96(B10):529–33.
[8] Sayers CM, Kachanov M. Microcrack-induced elastic wave anisotropy of brittle rocks. J Geophys Res 1995;100(B3):4149–56.
[9] Schubnel A, Guéguen Y. Dispersion and anisotropy of elastic waves in cracked rocks. J Geophys Res 2003;108(B2):2101.
[10] Guéguen Y, Schubnel A. Elastic wave velocities and permeability of cracked rocks. Tectonophysics 2003;370:163–76.
[11] Kachanov M. Effective elastic properties of cracked solids: critical review of some basic concepts. Appl Mech Rev 1992;45(8): 304–35.
[12] Kachanov M. Elastic solids with many cracks and related problems. In: Hutchinson JW, Wu T, editors. Advances in applied mechanics, vol. 30. Academic Press; 1993. p. 259–445.
[13] Budiansky B, O'Connell RJ. Elastic moduli of a cracked solid. Int J Solids Struct 1976;12:81–97.
[14] Gottesman T, Hanshin Z, Brull MA. Effective elastic moduli of cracked fiber composites. In: Bussell AR, editor. Adv Compos Mater 1980:749–58.
[15] Benveniste Y. On the Mori–Tanaka's method in cracked bodies. Mech Res Commun 1986;13:193–201.
[16] Mori T, Tanaka K. Average stress in matrix and average elastic energy of materials with misfitting inclusions. Acta Metall 1973;21:571–4.
[17] Hashin Z. The differential scheme and its application to cracked materials. J Mech Phys Solids 1988;36(6):719–34.
[18] Huang Y, Hu KX, Chandra A. A generalized self-consistent mechanics method for microcracked solids. J Mech Phys Solids 1994;42(8):1273–91.
[19] Santare MH, Crocombe AD, Anlas G. Anisotropic effective moduli of materials with microcracks. Engng Fract Mech 1995;52(5):833–42.
[20] Greengard L, Helsing J. On the numerical evaluation of elastostatic fields in locally isotropic two-dimensional composites. J Mech Phys Solids 1998;46(8):1441–62.
[21] Helsing Johan. Fast and accurate numerical solution to an elastostatic problem involving ten thousand randomly oriented cracks. Int J Fracture 1999;100:321–7.
[22] Wang YB, Chau KT. A new boundary element for plane elastic problems involving cracks and holes. Int J Fracture 1997;87(1): 1–20.
[23] Pan EN. A general boundary element analysis of 2-D linear elastic fracture mechanics. Int J Fracture 1997;88(1):41–59.
[24] Wang GS, Feng XT. The interaction of multiple rows of periodical cracks. Int J Fracture 2001;110(1):73–100.
[25] Dong CY, Lee Kangyong. Numerical analysis of doubly periodic array of cracks/rigid-line inclusions in an infinite isotropic medium using the boundary integral equation method. Int J Fracture 2005;133:389–405.
[26] Feltman RS, Santare MH. Anisotropic effective moduli of cracked short-fiber reinforced composites. J Appl Mech 1999;66:1–5.
[27] Zheng Q-S, Du D-X. An explicit and universally applicable estimate for the effective properties of multiphase composites which accounts for inclusion distribution. J Mech Phys Solids 2001;49:2765–88.
[28] Feng X-Q, Qin Q-H, Yu S-W. Quasi-micromechanical damage model for brittle solids with interacting microcracks. Mech Mater 2004;36:261–73.
[29] Kachanov M. Elastic solids with many cracks: a simple method of analysis. Int J Solids Struct 1987;23(1):23–43.
[30] Huang Y, Chandra A, Jiang ZQ, Wei X, Hu KX. The Numerical calculation of two-dimensional effective moduli for microcracked solids. Int J Solids Struct 1996;33(11):1575–86.
[31] Shen L, Yi S. An effective inclusion model for effective moduli of heterogeneous materials with ellipsoidal inhomogeneities. Int J Solids Struct 2001;38:5789–805.
[32] Shen L, Li J. A numerical simulation for effective elastic moduli of plates with various distributions and sizes of cracks. Int J Solids Struct 2004;41:7471–92.
[33] Wang YB, Sun YZ. A new boundary integral equation method for cracked 2-D anisotropic bodies. Engng Fract Mech 2005;72: 2128–43.

[34] Walsh JB. The effect of cracks on the uniaxial elastic compression of rocks. J Geophys Res 1965;70:399–411.
[35] Taya M, Mura T. On the stiffness and strength of aligned short fiber reinforced composites containing fiber end cracks under uniaxial applied stress. ASME J Appl Mech 1981;48:361–7.
[36] Anlas G, Santare MH. An arbitrarily oriented crack inside an elliptical inclusion. J Appl Mech 1993;60:589–94.
[37] ABAQUS analysis user's manual, 2003. ABAQUS, INC.
[38] Auld BA. Acoustic fields and waves in solids, vol. I. Malabar, FL: Krieger Publ. Co.; 1990. 435 pp.

Engineering Fracture Mechanics 75 (2008) 4104–4116

Contents lists available at ScienceDirect

Engineering Fracture Mechanics

journal homepage: www.elsevier.com/locate/engfracmech

An effective medium model for elastic waves in microcrack damaged media

Dan Su [a], Michael H. Santare [a,*], George A. Gazonas [b]

[a] Department of Mechanical Engineering and Center for Composite Materials, University of Delaware, Newark, DE 19716, USA
[b] US Army Research Laboratory, Weapons and Materials Research Directorate, Aberdeen Proving Ground, MD 21005, USA

ARTICLE INFO

Article history:
Received 29 June 2007
Received in revised form 3 April 2008
Accepted 7 April 2008
Available online 14 April 2008

Keywords:
Waves
Anisotropic damage
Numerical experiment
Effective moduli
Microcracks

ABSTRACT

Direct numerical simulations of waves traveling through microcrack-damaged media are conducted and the results are compared to effective medium calculations to determine the applicability of the latter for studying wave propagation. Both tensile and compressive waves and various angular distributions of randomly-located cracks are considered. The relationships between the input wavelength and the output wave speed and output signal strength are studied. The numerical simulations show that the wave speed is nearly constant when $1/ka > 60$ for tensile waves and $1/ka > 10$ for compressive waves, where k is the wave number and a is the average half-crack length. The direct simulations also show that when the input wavelength is much longer than the crack length, $1/ka > 60$, the wave can pass through the damaged medium relatively unattenuated. On the other hand, when the input wavelength is shorter than a "cut off" wave length, the output wave magnitude decreases linearly with the input wavelength. The effective medium wave speed and magnitude calculations are not dependent on the input wavelength and therefore the results correspond well with the numerical simulations for large $1/ka$. This suggests a minimum wavelength for which the homogenized methods can be used for studying these problems.

1. Introduction

For many brittle materials, the most common damage mechanism is microcracking. As microcracks develop, they change the local mechanical response to input loads. One way, commonly used to evaluate the quasi-static response of the damaged medium is by directly simulating an actual array of cracks. Solutions of this type include the fast multipole method (FMM, [1,2]), boundary element method (BEM [3,4]) and many other numerical solutions, such as described in [5–9]. The major advantage of these methods is that they take into account the actual crack–crack interactions. There is no theoretical limitation to the crack density or crack distribution and these direct methods can give highly accurate results if the model is an accurate representation of the damaged medium. However, the detailed calculation of the interaction between the cracks is also the major disadvantage of the direct methods. As the crack density increases, the modeling time and computational demands can increase dramatically.

To address this increase in computational demand, effective medium methods can be used. In these methods, one models the quasi-static response of a medium with diffuse microcrack damage by replacing the damaged material with an effective medium, possessing the same local mechanical properties. Many such effective medium models have been developed, such as the self consistent method (SCM) [10–12], Generalized self consistent method (GSCM) [13–17], Mori–Tanaka method (MTM) [18,19], and the differential scheme method (DSM) [20]. For a comprehensive review of the literature in effective mechanical properties prediction, readers can refer to [6,21].

* Corresponding author. Tel.: +1 302 831 2246; fax: +1 302 831 3619.
E-mail address: santare@me.udel.edu (M.H. Santare).

0013-7944/$ - see front matter © 2008 Elsevier Ltd. All rights reserved.
doi:10.1016/j.engfracmech.2008.04.003

While the above-cited literature primarily discusses the quasi-static response of microcrack-damaged media, several researchers have addressed elastic wave propagation behavior in these materials. In 1995 Sayers and Kachanov [22] used the effective moduli of a cracked medium to study microcrack-induced elastic wave anisotropy. In that paper, the authors used second-rank and fourth-rank crack density tensors to evaluate the effective elastic moduli. They calculated the effective moduli for the (randomly-oriented) isotropic distribution of cracks and the perfectly aligned cracks. For the isotropic cracked medium, they also back-calculated the crack density from experimental data of the ultrasonic wave speed. Following Sayers and Kachanov's results, Schubnel and Gueguen [23,24] used micromechanical and statistical physics to evaluate the elastic wave velocities and permeability of cracked rocks. They calculated the velocity for high and low frequency waves for both wet and dry cracks for an aligned array of cracks and an array composed of ±60° cracks under an external confining pressure. Maurel et al. [25] studied the elastic wave propagation through a random array of dislocations. Markov [26] used the Frenkel–Biot theory to study the longitudinal harmonic wave propagation in an isotropic porous matrix with inclusions. Levin and Markov [27] used an effective medium approximation (EMA), based on the self-consistent method, to determine the effective elastic moduli and elastic wave propagation velocities in a transversely isotropic solid containing aligned inclusions.

Yet, with all this literature, there are several questions which remain. For example, under what conditions can we model an actual damaged material with an equivalent effective medium? How accurate is the effective medium representation? What factors affect the accuracy?

Several researchers have performed studies to address some of these topics. Zhang and Gross [28] studied the propagation of an elastic wave through a medium with randomly distributed cracks. The cracks are treated as finite length lines with displacement discontinuity and the crack surfaces are assumed to be frictionless. They studied the scattering function for a single crack and expanded this using a numerical approach to study the response of multiple cracks. They used both the theory of Foldy and the causal approach based on K–K relations to compute the attenuation coefficient and the effective wave velocity. Littles et al. [29] performed an experimental and theoretical investigation to study how longitudinal waves are scattered by a distribution of cracks. The results show that the transmission coefficients are a function of the incident wave number, the crack size and crack density. Kawahara and Yamashita [30] studied the scattering of P, SV and SH waves by a zonal distribution of uniaxial cracks using a theoretical analysis. They showed that the attenuation coefficient peaks around $ka \approx 1$, the phase velocity is almost independent of k in the range of $ka < 1$ and increases monotonically when k is in the range of $ka > 1$. They also found that the effect of crack-face friction is to shift the peak of the attenuation coefficient toward the lower wave number range. Kelner et al. [31] used the boundary element method to simulate P wave propagation in media with uniaxial cracks. The authors conclude that when the wavelength of the incident wave is close to, or shorter than, the crack length, the scattered waves are efficiently excited. They also observed that the attenuation factor of the direct P wave peaks at around $ka = 2$, where k is the incident wave number and a is the crack length, and decreases proportionally with $(ka)^{-1}$ in the high wave number range.

Most of the above papers focus on low crack densities and high frequency input waves, a combination which corresponds to high attenuation. Also, the crack orientations in most of the papers are limited to aligned or randomly-oriented distributions. Additionally, in most of the literature cited, the authors assume the crack surfaces are stress free, which means the cracks are opened under all loads. In our previous paper [16], we use the generalized self consistent method (GSCM) to predict the anisotropic effective moduli of a medium containing an arbitrarily-oriented distribution of cracks. In that paper, we show that because the cracks open or close under different external loads, the effective moduli under different loading conditions are quite different. In that paper, we discussed three different loading conditions: (1) overall applied tensile loads; (2) overall compressive loads; (3) initially stress free media. The effective moduli under these three different loading conditions are evaluated taking into account the effects of crack-face contact. In that paper we also mentioned that tensile and compressive wave propagation in the same medium behave very differently. In this paper, we study under what conditions one may use the calculated effective moduli to simulate wave propagation in the microcrack damaged medium. We conduct direct numerical simulations to relate input wavelength to propagating wave speed and output signal strength, and compare these results to those obtained via the effective medium models. Once these comparisons are established, we can establish guidelines for the use of effective medium calculations to analyze ultrasound data for determining the internal state of microcrack damage.

2. FEM model

In the following numerical experiments, we use the definition of crack density and crack orientation distribution function $\phi(\theta)$ described in [15,16]. We define the crack density as

$$\eta = \frac{Ma^2}{A}, \tag{1}$$

where M is the number of cracks per unit area A, and a is the average half-crack length. We assume the crack orientation can be described by an orientation distribution function $\phi(\theta)$, where θ is the angle of the individual crack with respect to the average crack orientation, assigned to be the x-axis. In the following analysis, we assume that the cracks are evenly distributed between the angles $-\theta_0$ and $+\theta_0$, as shown in Fig. 1. A more detailed description of the crack distribution function $\phi(\theta)$, and crack density function η, can be found in [16].

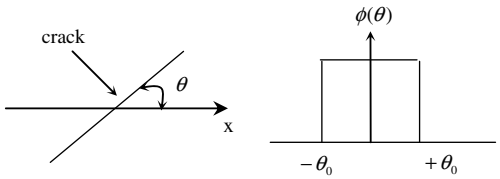

Fig. 1. Even distribution of crack orientation.

To simulate uni-directional plane wave propagation, we assume an infinite half plate, and apply a time-dependent load uniformly along the top surface (Fig. 2a). Because the plate is infinitely extended in the x-direction, we can pick a strip from anywhere in the half plane as a representative sample (Fig. 2b) by applying symmetry boundary conditions to the left and right edges of the strip. The location of each crack within the strip was generated by a random number generator as was the crack angle θ chosen to be in the interval $+\theta_0$ and $-\theta_0$. If the randomly generated location of a crack caused it to overlap with an already existing crack, that crack was eliminated from the model and the process was continued until the desired crack density was reached. Cracks that contacted the left or right boundaries were kept in the model, but because of the symmetry conditions imposed on these boundaries, their lengths could be quite different from the average. Building the model in this manner, the array is not completely random, but represents a relatively homogeneous approximation to randomly distributed cracks. Contact elements are placed along the cracks to prevent crack-face interpenetration. Fig. 2b is a representation of the models used in the numerical experiments. A number of trial models were run to determine an appropriate length and width for the strips and the chosen dimensions represent a compromise between a model large enough to eliminate edge effects and one small enough to allow for efficient computations. All lengths are normalized with respect to the average crack length ($2a$) and the resulting width of each model is 4, and the length is 80. In all the results that follow, the crack density parameter is chosen to be $\eta = 0.4$. (Most of the previously reviewed literature studies crack densities in the range of 0.1–0.2 when defined by the term η, in Eq. (1)) Larger densities proved difficult to model, due to interference between individual cracks and smaller densities show the same overall trends, but to a lesser extent. Since the cracks are randomly located and oriented, we constructed four or five models for each orientation distribution to show the variability introduced by the randomness.

In the simulation, we use ABAQUS 6.4.4 as the finite element solver. In Figs. 3–6, we show the finite element models for samples 1–14. As shown in Fig. 3d, each crack is represented by two crack surfaces with zero distance between them. Therefore, in the stress free state, all the cracks are closed.

In order to study the relationship between the input wavelength and the output signal, we apply a single frequency time-dependent load, uniformly along the top of the strip. Fig. 7 shows a sample input load with the function

$$P(t) = A\left[\frac{1-\cos(\omega t)}{2}\right], \quad \text{for} \quad 0 \leqslant \frac{\omega t}{2\pi} \leqslant 1, \tag{2}$$

where, $P(t)$ is the time-dependent load, A is the maximum load amplitude, ω is the circular frequency of the input and t is the time. We can apply positive or negative pressure in order to generate a compressive or tensile wave inside the sample.

In the numerical experiments, we use the dimensionless number $1/ka$ as the effective wave length parameter, where a is the average half-crack length, $k = \omega/c_p$, ω is the input wave frequency and $c_p$is the plane-stress longitudinal wave velocity in the un-damaged medium [32], which is defined as

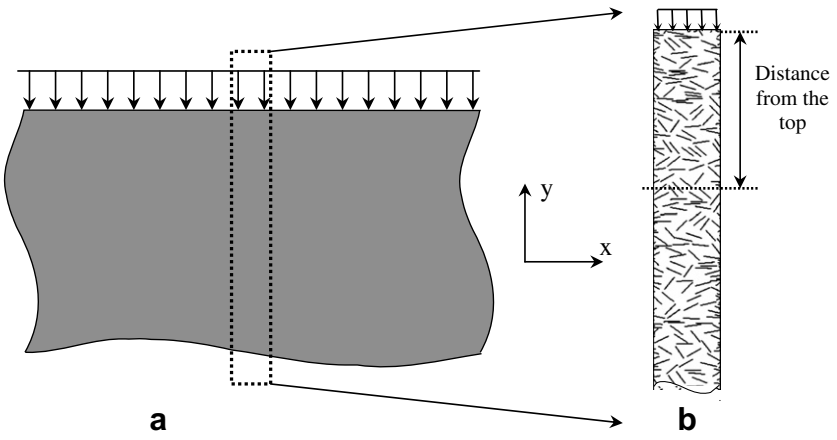

Fig. 2. Model schematics. (a) Time-dependent load is applied along the top boundary of the half plane. (b) A representative strip from the plane is used in the finite element simulation.

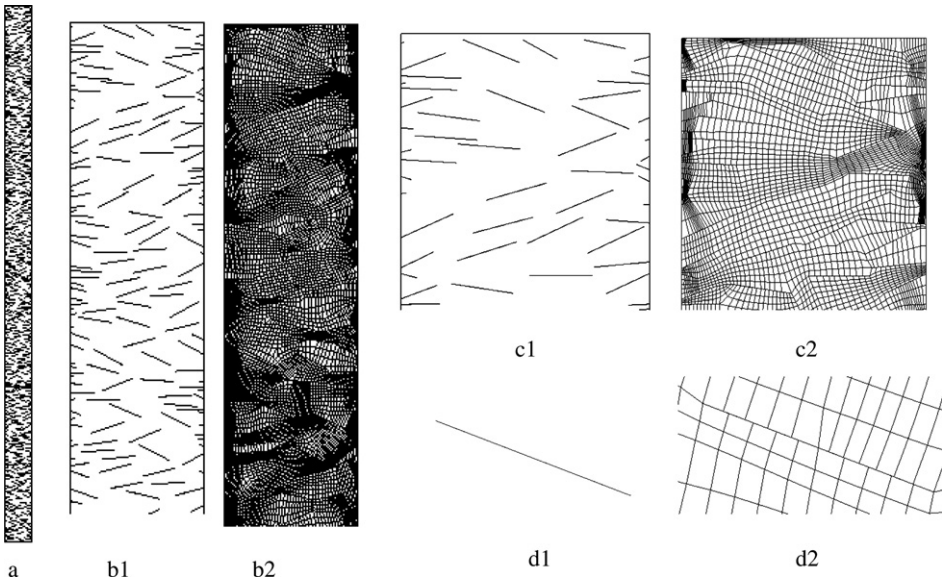

Fig. 3. Finite element model of sample 06 ($\theta_0 = 30°$). (a) Whole model without mesh detail. (b1, b2) Zoom in for the top part with and without mesh detail. (c1, c2) Further zoom in with and without mesh detail. (d1, d2) Zoom in for a single crack with and without mesh detail.

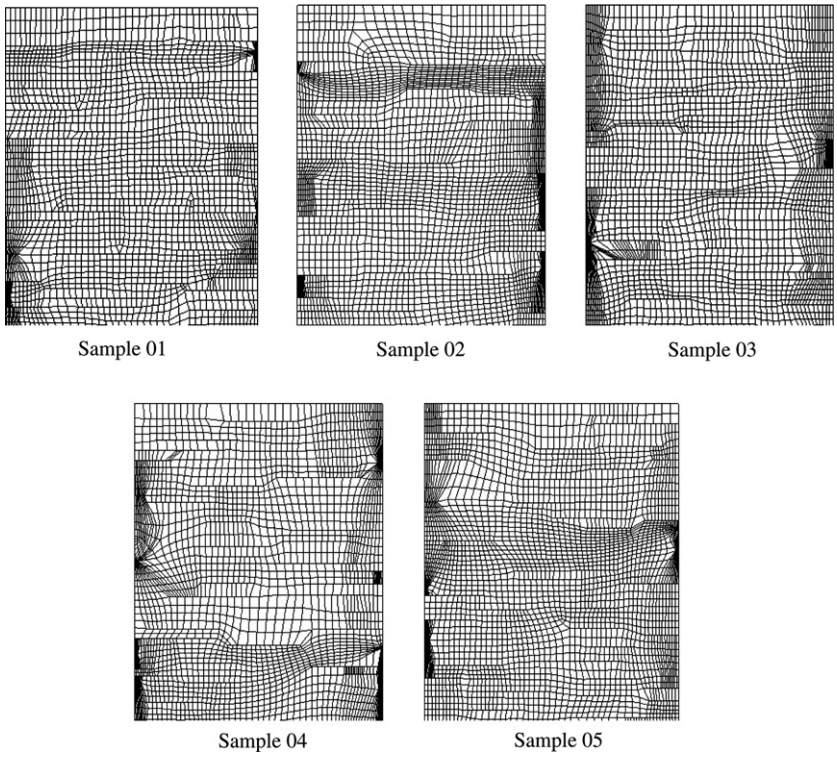

Fig. 4. The top part of finite element model of samples 01–05 ($\theta_0 = 0°$).

$$c_p = \sqrt{\frac{E}{(1-\nu^2)\rho}}. \tag{3}$$

This effective wave number $1/ka$, therefore represents the ratio between the input wave length in the undamaged media and the average half crack length.

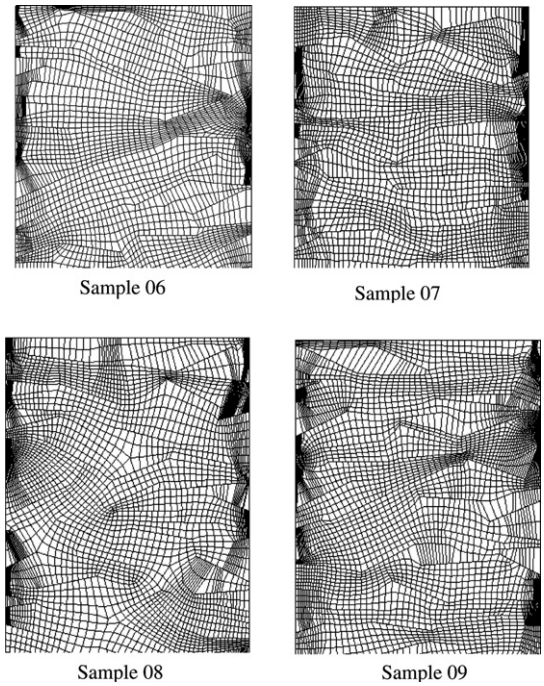

Fig. 5. The top part of finite element model of samples 06–09 ($\theta_0 = 30°$).

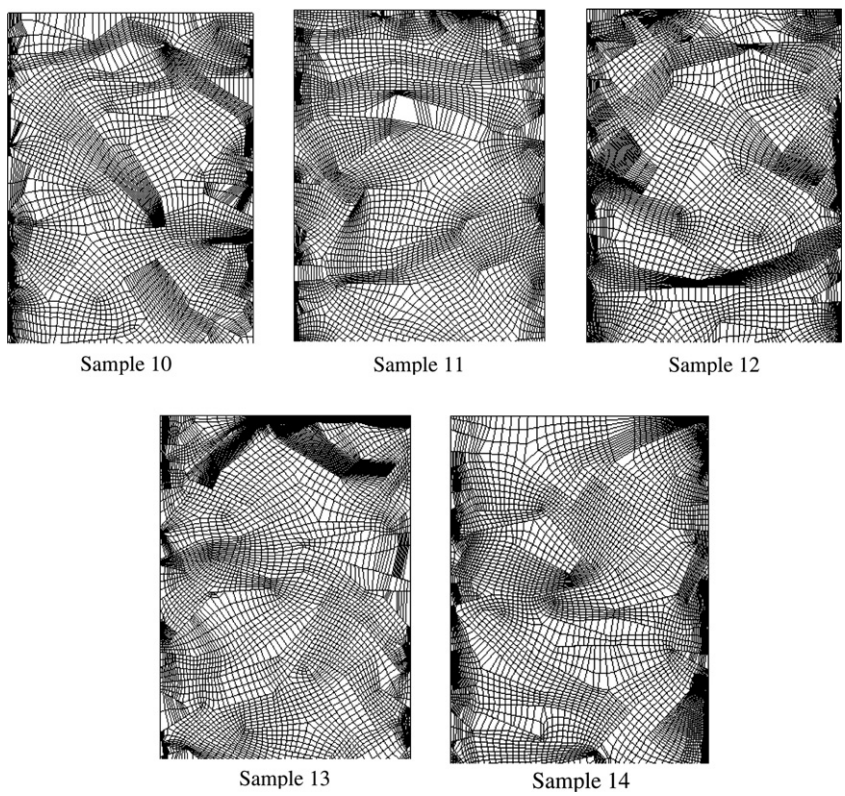

Fig. 6. The top part of finite element model of samples 10–14 ($\theta_0 = 60°$).

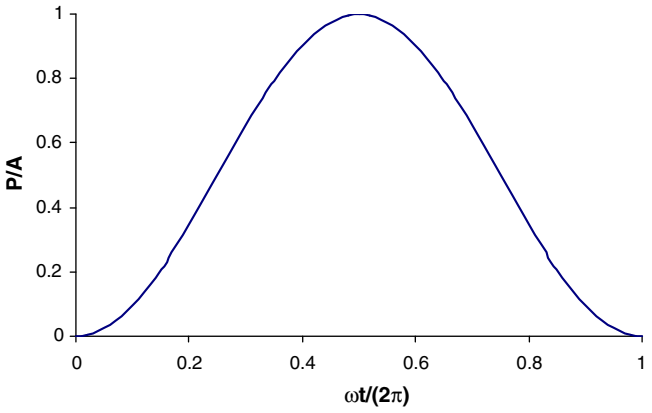

Fig. 7. Sample input load. The function of the input load is $P = A\frac{1-\cos(\omega t)}{2}$ for $0 \leqslant \frac{\omega t}{2\pi} \leqslant 1$.

3. Wave speed calculation

In this section we determine the wave speeds in the direct numerical simulations and compare these to the speeds in the effective media models. The properties of the effective media, and the generalized-self-consistent method used to calculate them, are shown in [16]. All the wave speeds are normalized by the plane-stress wave speed in the intact material c_p, shown in Eq. (3). We trigger the wave from the top of the models with time dependent pressure loads and trace the stress component σ_y. We chose 1% of the maximum input as the threshold value for the stress at the wave front. This means that we assume that the wave arrives at a particular cross section when the average stress σ_y in that cross section reaches 1% of the maximum input stress.

In Figs. 8–10, we show the wave speed in each of the direct numerical simulation models as a function of the input wave length number $1/ka$, as well as the effective medium predictions and an analytical solution. The analytical solution is the uniaxial longitudinal wave speed, which can be derived from [33], for an anisotropic plane stress medium calculated from

$$c_{p2} = \sqrt{\frac{E_2}{(1 - v_{12}v_{21})\rho}}, \tag{4}$$

where E_2, v_{12}, v_{21} are the corresponding effective Young's moduli in y direction, and the effective Poisson's ratios, which are shown in [16] and ρ is the corresponding mass density. Fig. 8 shows results for the five different models with an aligned array of cracks $\theta_0 = 0°$. Fig. 9 contains the models with crack orientations evenly distributed between the values $\theta_0 = \pm 30°$ and Fig. 10, the models with angles between $\theta_0 = \pm 60°$. The left column in each figure shows the tensile wave speed, while the right column shows the speed of compressive waves.

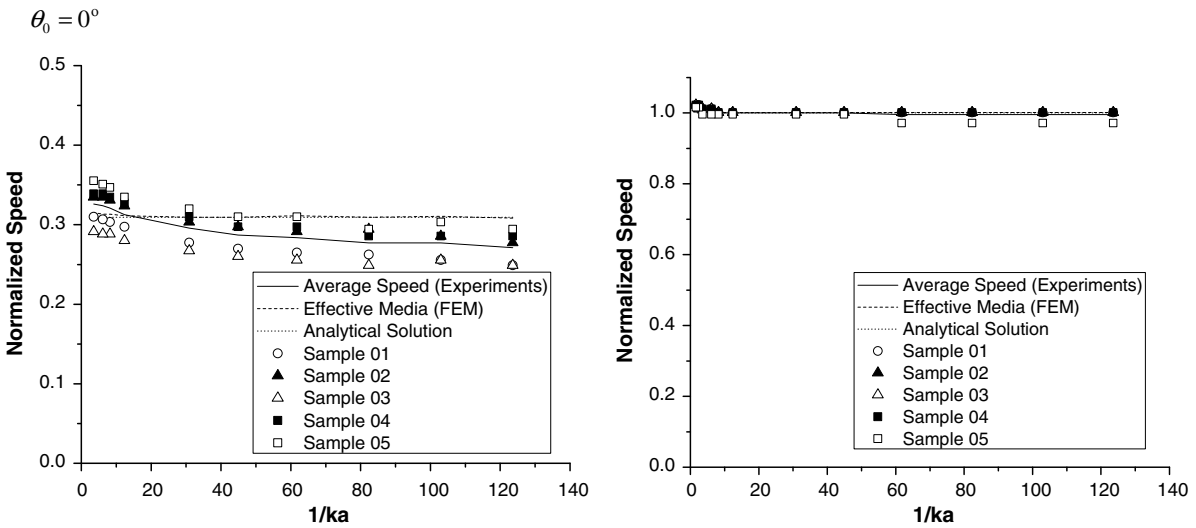

Fig. 8. Normalized wave speed vs. $1/ka$ for $\theta_0 = 0°$. Left : speed of tensile waves. Right : speed of compressive wave.

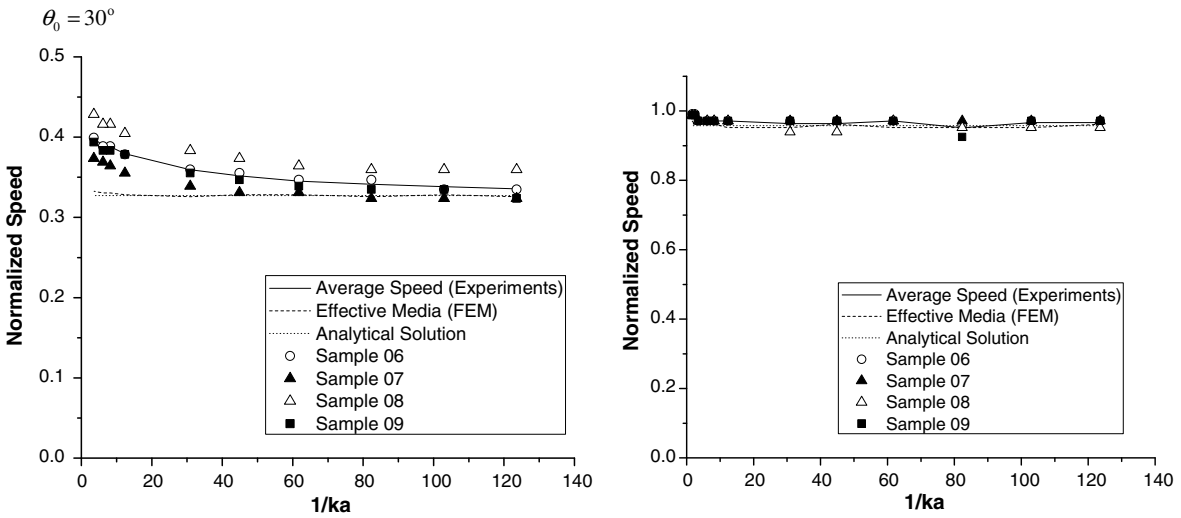

Fig. 9. Normalized wave speed vs. $1/ka$ for $\theta_0 = 30°$. Left figure: speed of tensile waves. Right figure: speed of compressive wave.

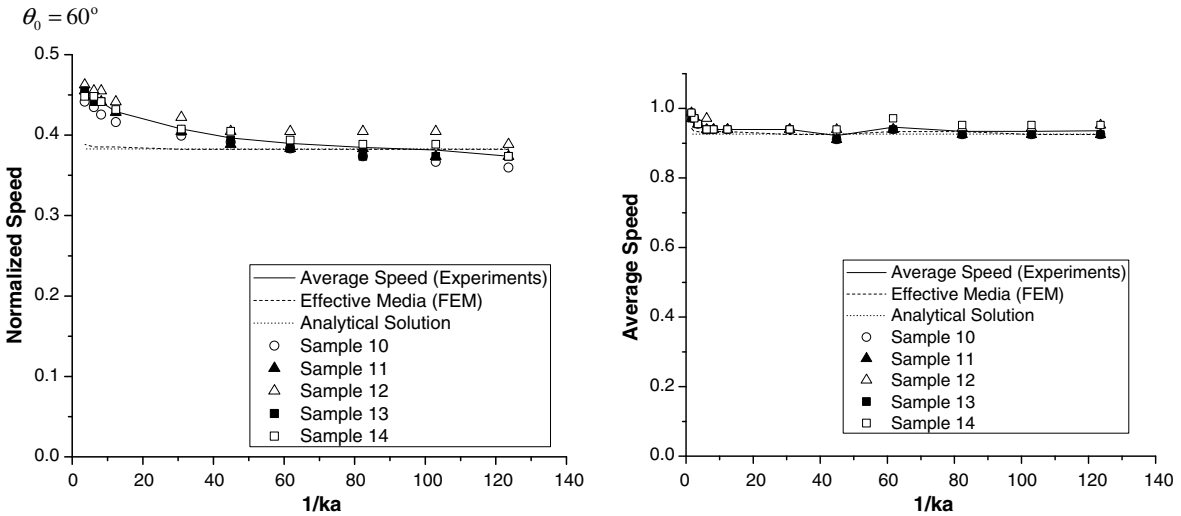

Fig. 10. Normalized wave speed vs. $1/ka$ for $\theta_0 = 60°$. Left : speed of tensile waves. Right : speed of compressive wave.

From the results, we can see that in all cases, the compressive waves travel much faster than the tensile waves. This is because under compression, the cracks can only open in mode II (shear opening) (As we discuss in Section 2, in the stress-free state, the distance between the cracks surfaces is zero. Therefore, the crack surfaces cannot move closer to each other under compression.) while in tension, the cracks can open in both mode I (normal opening) and mode II. Therefore for a given medium, the material is much less stiff when tensile waves pass through, than when compressive waves pass through. For a detailed discussion regarding the different effective material properties under different loads, the reader is referred to [16]. The figures also show that the effective medium models correspond well with the numerical experiments in the cases considered. For the case of tensile wave speed when $\theta_0 = 0°$, the analytical equations and the effective media model give higher wave speed predictions than the direct numerical simulations. This is because for tensile waves, when $\theta_0 = 0°$, the cracks in the numerical simulations cause significant energy dispersion as the wave travels along the strip. Therefore, for the same input magnitude, it takes longer for the average stress across the strip to reach the 1% threshold value, resulting in a slightly lower calculated speed for the direct simulations.

Kawahara and Yamashita [30] found analytical solutions for a similar problem containing randomly distributed, aligned cracks under confining pressure. They found that when the crack surfaces are friction free, the phase velocity is nearly independent of k when $1/ka > 1$ and increases monotonically with k when $1/ka < 1$. From the right column of Figs. 8–10 we can see that the wave speed in our numerical experiments follows this same trend and are completely consistent with the ana-

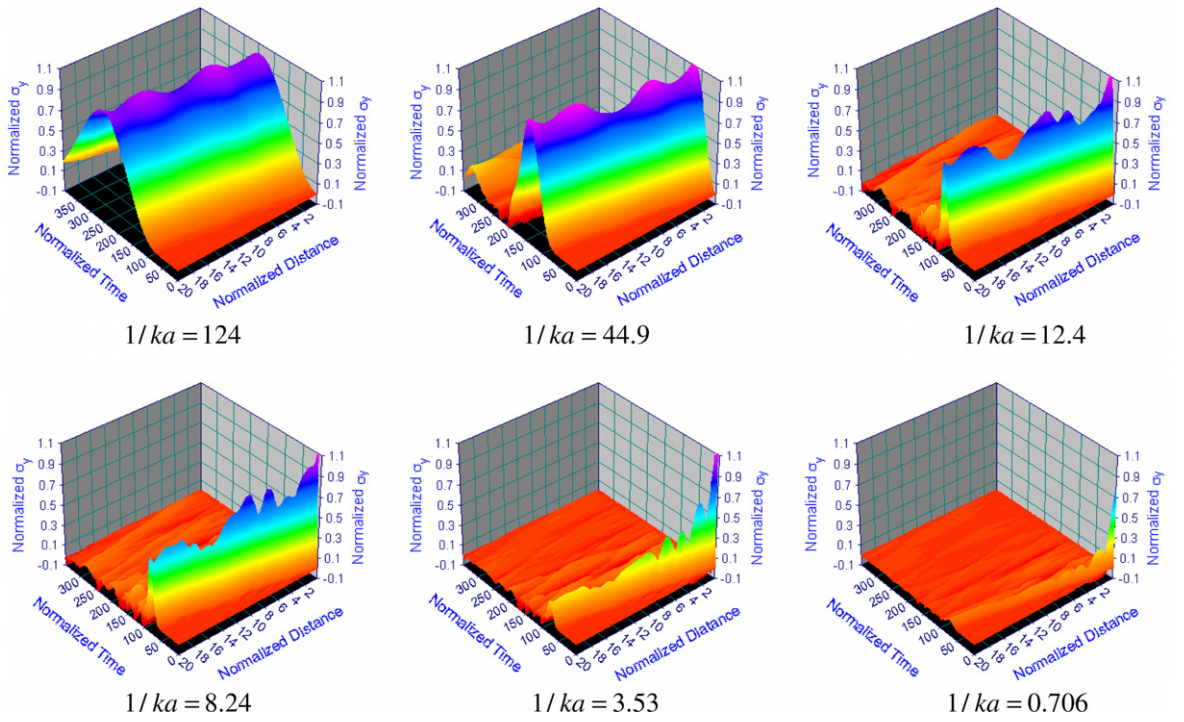

Fig. 11. Tensile waves with different effective wave number traveling in sample 05, $\eta = 0.4$, $\theta_0 = 0°$. Normalized σ_y is the average stress σ_y in the specific cross session normalized by the maximum average stress σ_y at distance equal to zero (the top boundary). The distance from the top is shown in Fig. 2b.

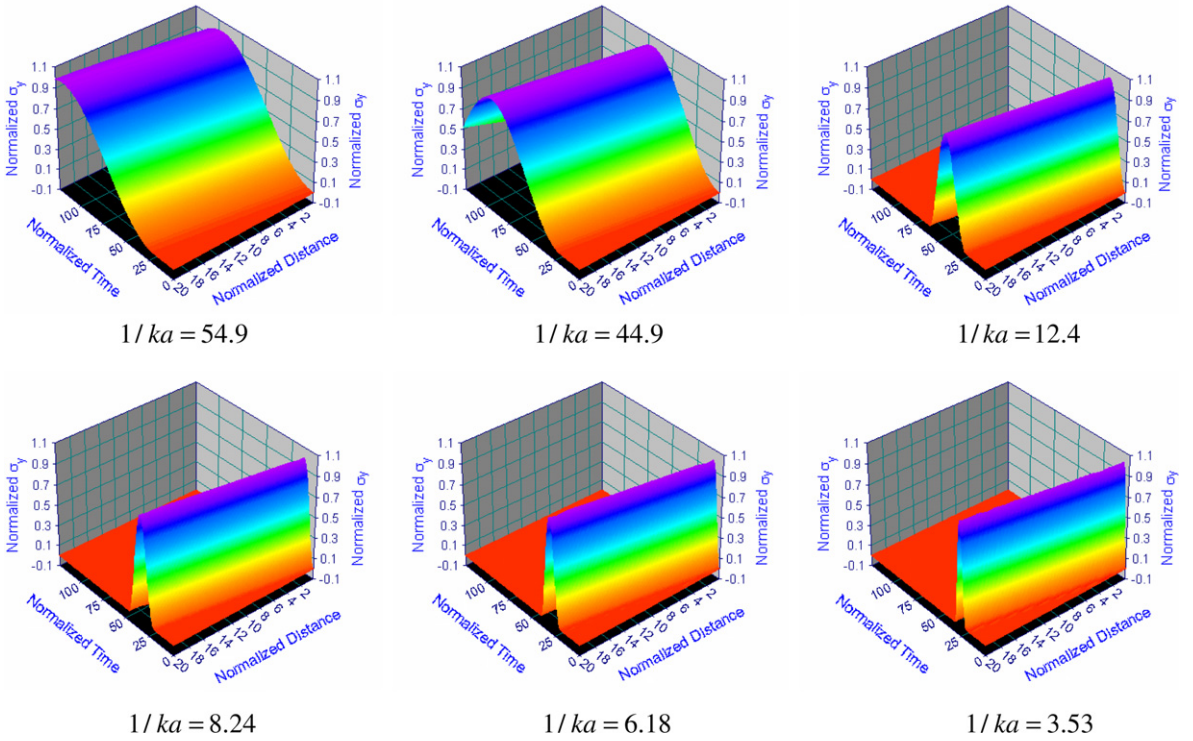

Fig. 12. Compressive waves with different effective wave number traveling in sample 05, $\eta = 0.4$,$\theta_0 = 0°$. Normalized σ_y is the average stress σ_y in the specific cross session normalized by the maximum average stress σ_y at distance equal to zero (the top boundary). The distance from the top is shown in Fig. 2b.

lytical results in Kawahara and Yamasita's paper for cracks under compression. At the same time, from the left column in Figs. 8–10 we see that the tensile wave speed is nearly constant when $1/ka > 60$ and increases monotonically when $1/ka < 60$. Therefore, we can see that the Kawahara and Yamasita's general conclusion still applies to tensile wave propagation in our current study, although the cut off ka (or $1/ka$) value is much different for tensile waves than compressive waves.

4. Signal strength

In the direct numerical simulations, we applied a uniform, time varying load along the top boundary of the finite element models, as shown in Fig. 2b. For a specific time and a specific cross section in the model, we record the average stress component σ_y through this cross section (Fig. 2b) then normalize this value by the maximum average stress σ_y calculated at the top boundary of the model. (Recall that the crack length $2a$ equals 1, except for the cracks that touch the boundary.) The properties of the intact material are $E/\mu = 8/3$, $\nu = 1/3$, where E is Young's modulus, μ is shear modulus and ν is Poisson's ratio. The normalized time is defined as $\widehat{t} = \frac{t}{2a/c_p} = tc_p/(2a)$.

Fig. 11 shows the results for the tensile waves with different effective wave numbers traveling in sample 05. We can see that for tensile waves, when the input wavelength is much larger than the crack length, ($1/ka > 10$), the input signal passes through the damaged medium relatively unattenuated (the first row of the figures). When the input wavelength is smaller, ($1/ka = 8.24$ and 3.53) the cracks show a larger "blocking" effect and the transmitted wave shows smaller stress amplitude. When the input wavelength is about the same as the crack length, ($1/ka = 0.706$) the signal is almost completed blocked by the damage.

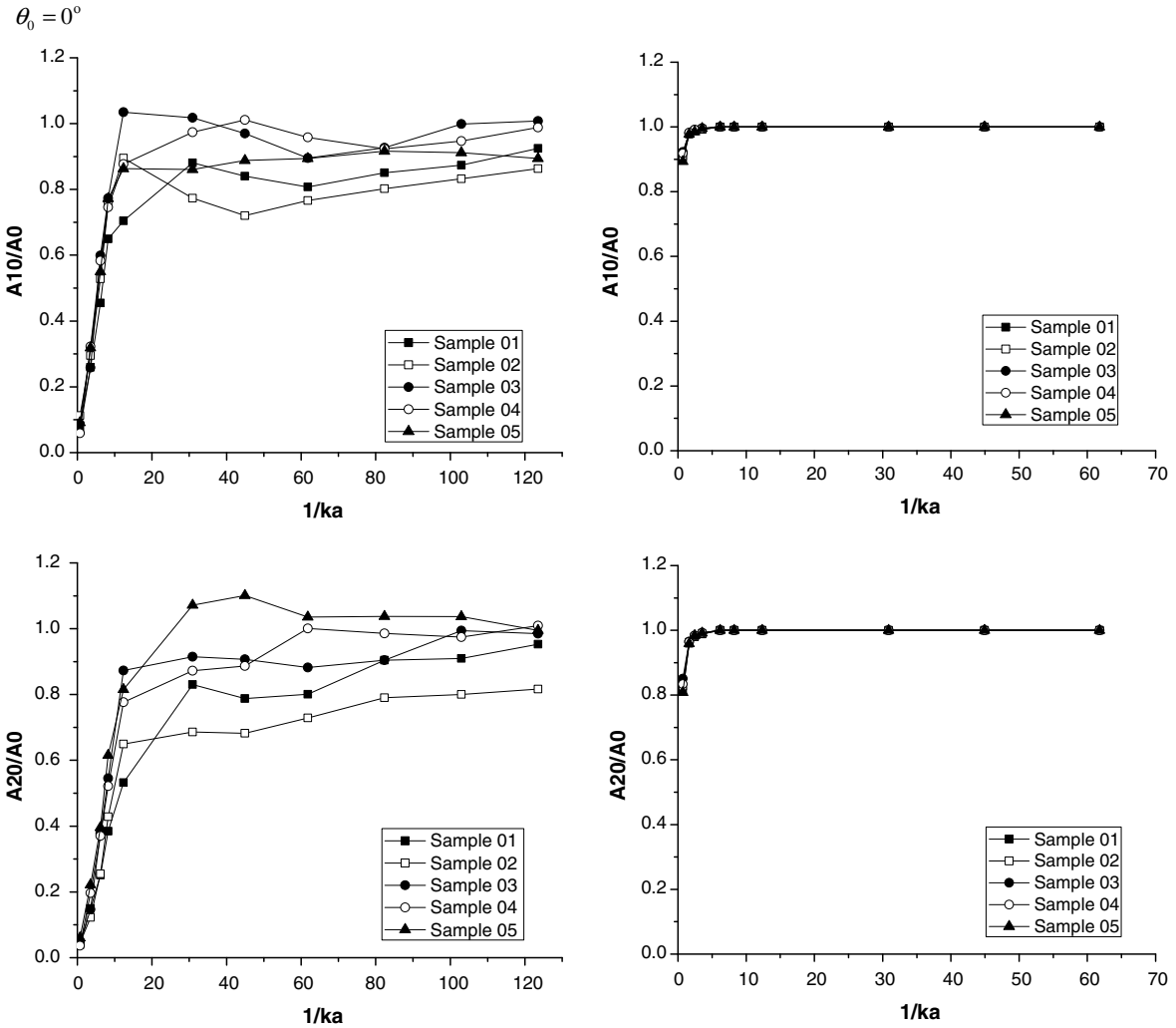

Fig. 13. Output signal strength vs. input effective wave number ($1/ka$) for the models with $\eta = 0.4$, $\theta_0 = 0°$ and $2a = 1$. Left column: Tensile waves output. Right column: Compressive waves output. First row: The normalized peak averaged stress measured at distance equal to 10. Second row: The normalized peak averaged stress measured at distance equal to 20.

Fig. 12 shows the compressive wave propagation through the same model sample 05. Comparing Fig. 11 with Fig. 12, we can see that the compressive wave signal does not decrease appreciably, even when the input wavelength $(1/ka)$ is relatively small. This is because when tensile waves pass through the sample, the cracks are opened and parts of the waves are reflected by the open crack surfaces, causing the output signal to decrease. Yet, when compressive waves travel in the model, all the cracks remain closed and therefore have almost no effect on the wave propagation in this situation.

5. Output signal strength

5.1. Uniform crack length

In this section, we show how the peak stress values at different cross sections change with varying input wavelength. In Figs. 13–15, A0, A10 and A20 represent the peak average stress σ_y at cross sections with normalized distances of 0, 10 and 20, respectively from the top of the model. Fig. 13 shows results for the models with an aligned array of cracks $\theta_0 = 0°$ and Figs. 14 and 15 contain the models with cracks oriented between the values $\theta_0 = \pm 30°$ and $\theta_0 = \pm 60°$ respectively. As before, the left column in each figure shows the results for the tensile waves, while the right column shows the results for the compressive waves.

In Figs. 13–15, the individual lines represent the different model samples. In all of these models $\eta = 0.4$ and $2a = 1$ (except for the cracks that touch the boundaries). All of these models show the same phenomenon observed in the previous section

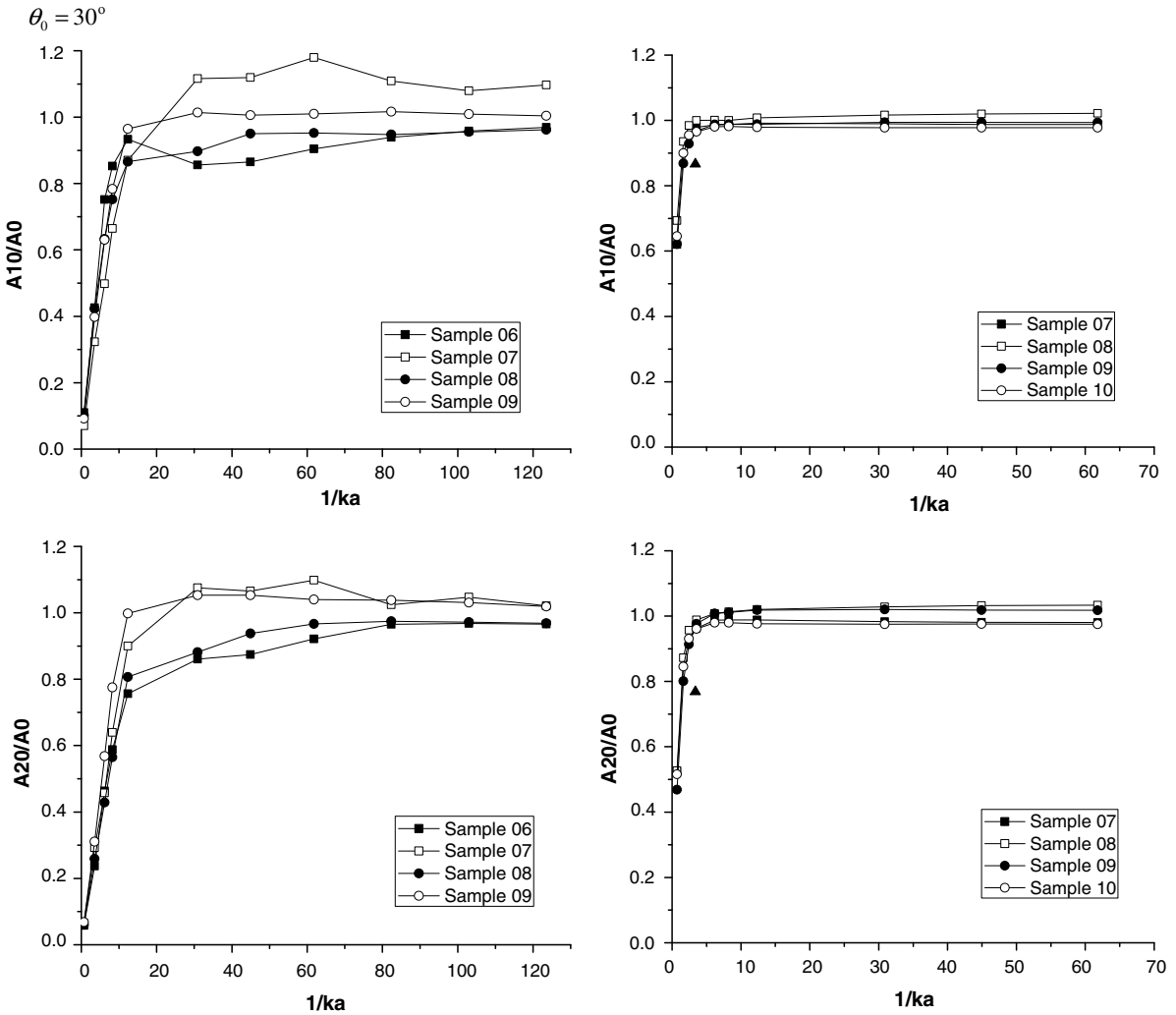

Fig. 14. Output signal strength vs. input wave length number $(1/ka)$ for the models with $\eta = 0.4$, $\theta_0 = 30°$ and $2a = 1$. Left column: Tensile waves output. Right column: Compressive waves output. First row: The normalized peak averaged stress measured at distance equal to 10. Second row: The normalized peak averaged stress measured at distance equal to 20.

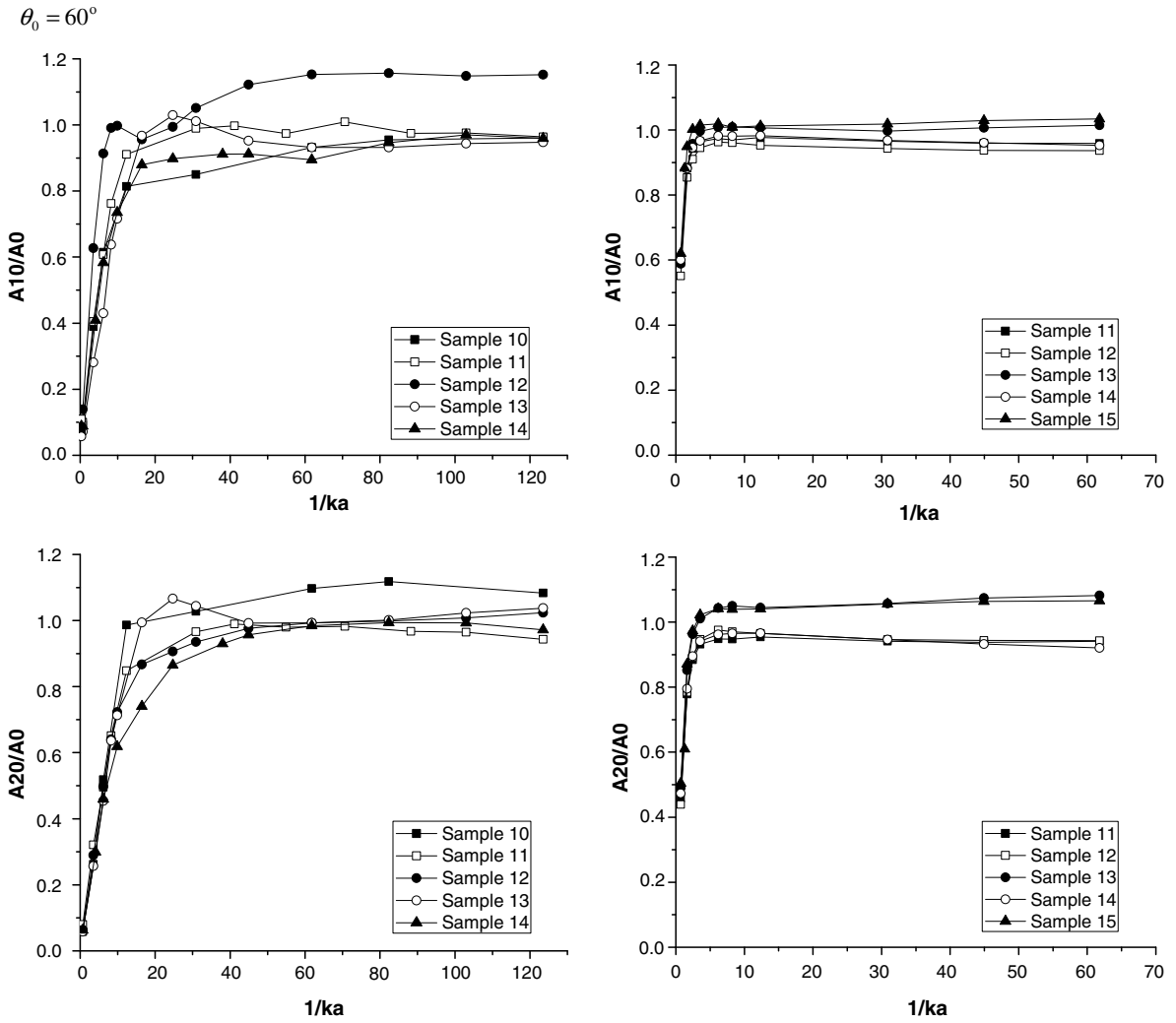

Fig. 15. Output signal strength vs. input wave length number $(1/ka)$ for the models with $\eta = 0.4$, $\theta_0 = 60^\circ$ and $2a = 1$. Left column: Tensile waves output. Right column: Compressive waves output. First row: The normalized peak averaged stress measured at distance equal to 10. Second row: The normalized peak averaged stress measured at distance equal to 20.

when we discussed the results of sample 05. What these figures bring out, is the variability from the different arrays of cracks (different experimental samples) as well as more clearly delineating the signal strength–wavelength relationship.

For tensile waves, when the input wave length is much larger than the crack length ($1/ka > 20$), the input signal passes through the microcrack damaged medium relatively easily. The output signal strength remains nearly constant for all input wavelengths above ($1/ka > 20$), and the output signal strengths are usually more than 80% of the input signal strength. On the other hand, the cracks show larger "blocking" effect when the input wave length decreases. In the area where $1/ka < 15$, the output signal strength decreases almost linearly with the input $1/ka$ decreases. Therefore, we can think of $1/ka = 15$ as a "cut off" wave length below which tensile waves will not travel through a microcrack damaged medium. When the input wavelength is close to or smaller than the crack length ($1/ka \approx 1$), almost no signal can pass through the medium.

For compressive waves, we can see the similar phenomenon but there are two differences that distinguish the compressive wave output from the tensile wave output. First, when the $1/ka$ number is large, the output signal of the compressive waves is much more uniform than that of the tensile waves. Secondly, the "cut off" wave length for the compressive waves is much smaller than that for the tensile waves. In this study we see that for compressive waves, the output signal decreases only when $1/ka < 5$.

These results suggest that there is a "safe range" for modeling microcrack-damaged media with homogenized effective medium approximations. When the input wavelength is larger than the "cut off" wavelength, the signal can travel relatively unattenuated through the medium. In this range, the effective medium FE models give a very good approximation to the actual medium with damage. On the other hand, applying the homogenized methods in the range with input wavelength

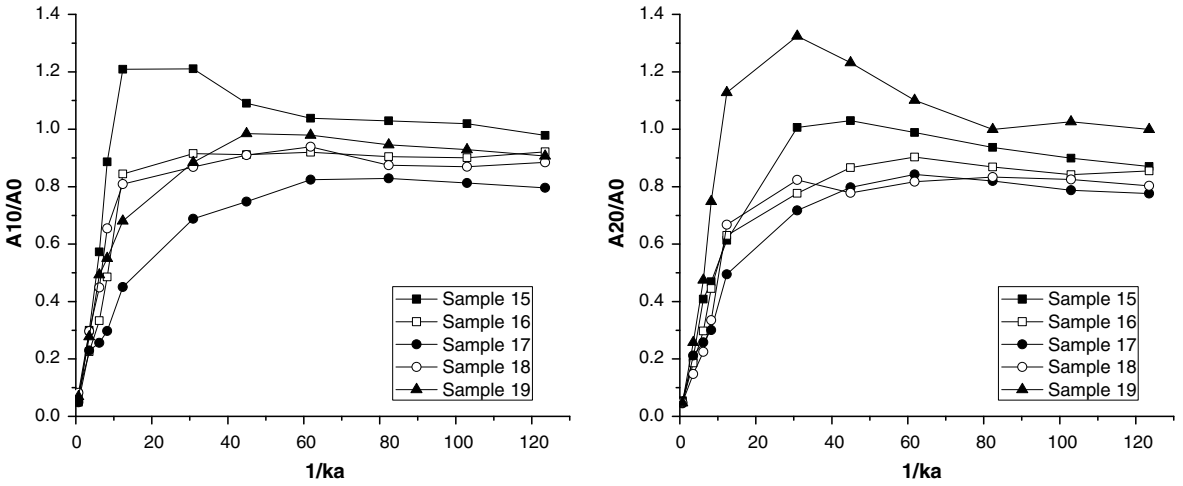

Fig. 16. Output signal strength v.s. $1/ka$ for tensile waves in the models with $\theta_0 = 0°$. The crack length $2a$ is evenly distributed between 0.6 and 1.4, with average of 1.0. Left figure: The normalized peak averaged stress measured at distance equal to 10. Right figure: The normalized peak averaged stress measured at distance equal to 20.

below the "cut off" wavelength is inappropriate, unless we modify the homogenized methods to take the wave length dependent energy dissipation into account.

We also expect the "cut off" $1/ka$ to decrease when the crack density decreases. This is because when the crack density decreases, there are fewer cracks per unit area. Therefore, less energy will be dissipated by the cracks when the wave passes through the media.

On a PC with a Pentium 4, 2.0 GHz CPU and 1GB RAM, it took from 3 to 30 h for a single point in the tensile Figs. 13–16 depending on the crack distribution and the time frame of simulation for the wave propagation. For the compressive cases, the time varied from 2 to 5 h.

5.2. Distributed crack lengths

Fig. 16 shows the output signal strength as a function of $1/ka$ for a set of models with $\theta_0 = 0°$ and average crack length $2a$. These are different than the previous models however, because the individual crack length is variable. For simplicity, we choose an even distribution of crack lengths between 0.6 and 1.4 with the average of 1.0, (again, except for the cracks that touch the boundaries). Comparing Fig. 13 with Fig. 16, we can see that for the models with distributed crack lengths, the signal strength values have a wider band for the range of $10 < 1/ka < 60$. Outside of this region, the results in Figs. 13 and 16 are quite similar to each other. We can conclude from this result, that a distributed crack length will not have a large effect on the "cut off" wavelength and the "safe range" for using the homogenized effective medium calculations.

From the above figures we can see that in most of the cases the output signal strength is weaker than the input signal strength. The reason is obvious: the reflection and diffusion between the cracks reduce the average signal strength. However, in some regions of several samples, we see that the output signal is actually stronger than the input signal. This can be explained by the random distribution of the cracks. When the wave travels through a field of cracks in the direct numerical simulations, part of the wave is reflected by the crack surfaces and interferes with other components of the wave which follow. Therefore, the local distributions of the cracks in the models can actually increase the local stress wave amplitude in some regions.

6. Conclusions and discussion

In this paper, we performed direct numerical simulations of waves traveling in micro-crack damaged media and compared these to results using a homogenized effective medium calculation. For the numerical simulations, we built several models with different crack distributions for each of three angular distributions; $\theta_0 = 0°$, $\theta_0 = 30°$ and $\theta_0 = 60°$. We studied the wave speed variation as a function of the input wavelength in each model for both tensile waves and compressive waves. The results for wave speed in the effective medium models are close to the numerical simulation results.

When a plane wave approaches an obstacle, the obstacle will reflect (or block) a portion of the advancing wave energy. If the obstacle is small with respect to the wavelength of the advancing wave, there will be a small disturbance in the wave front, but the majority of the energy will pass. Essentially, the wave travels around the obstacle. However, if the obstacle is large with respect to the wavelength, it will reflect a significant portion of the wave, detracting from the energy remaining in the transmitted wave. These observations are supported by Eringen's [34] analytical solutions of scattering of a plane

wave with a single cylindrical obstacle. Eringen found that the total scattered power increases with decreasing wavelength ($ka = 2\pi a/\lambda$) of the incident plane wave. Here, a is the radius of the cylinder and λ is the wavelength of the incident plane wave. For incident waves with large wavelengths (large $1/ka$) the scattered elastic energy approaches zero and the wave does not "see" the obstacle; we have determined that for crack systems modeled using our finite element approach this occurs for $1/ka > 60$ for media in tension, and $1/ka > 10$ for those in compression. In the case of distributed obstacles (such as the microcracks in the present study), the effect is more evident since the plane wave energy that passes by the obstacles (cracks), will be further blocked by other obstacles behind the first ones.

We also studied the relationships between the input wavelength and output signal strength. These results show that for both tensile and compressive waves, there is a "cut off" wavelength above which the wave can easily pass through the damaged medium and that this "cut off" is different in tension and compression. When the input wavelength is shorter than the "cut off" wave length, the output wave strength decreases linearly with the input wavelength. When the input wavelength is close to average crack length, ($1/ka = 1$) the wave is highly diffused. This suggests a "safe range" for using the homogenized effective media methods in studying these problems without considering the wave length dependent energy diffusion.

Acknowledgement

This research was supported by the United States Army Research Laboratory through the Composite Materials Technology cooperative in agreement with the Center for Composite Materials at the University of Delaware.

References

[1] Greengard L, Helsing J. On the numerical evaluation of elastostatic fields in locally isotropic two-dimensional composites. J Mech Phys Sol 1998;46(8):1441–62.
[2] Helsing J. Fast and accurate numerical solution to an elastostatic problem involving ten thousand randomly oriented cracks. Int J Fract 1999;100(4):321–7.
[3] Wang YB, Chau KT. A new boundary element for plane elastic problems involving cracks and holes. Int J Fract 1997;87(1):1–20.
[4] Pan EN. A general boundary element analysis of 2-D linear elastic fracture mechanics. Int J Fract 1997;88(1):41–59.
[5] Kachanov M. Elastic solids with many cracks – a simple method of analysis. Int J Sol Struct 1987;23(1):23–43.
[6] Kachanov M. Effective elastic properties of cracked solids: critical review of some basic concepts. Appl Mech Rev 1992;45(8):304–35.
[7] Huang Y, Chandra A, Jiang ZQ, Wei X, Hu KX. The numerical calculation of two-dimensional effective moduli for microcracked solids. Int J Sol Struct 1996;33(11):1575–86.
[8] Shen LX, Li J. A numerical simulation for effective elastic moduli of plates with various distributions and sizes of cracks. Int J Sol Struct 2004;41(26):7471–92.
[9] Shen LX, Yi S. An effective inclusion model for effective moduli of heterogeneous materials with ellipsoidal inhomogeneities. Int J Sol Struct 2001;38(32–33):5789–805.
[10] Budiansky B, O'Connell RJ. Elastic moduli of a cracked solid. Int J Sol Struct 1976;12(2):81–97.
[11] Gottesman T, Hanshin Z, Brull MA. Effective elastic moduli of cracked fiber composites. In: Bussell AR, editor. Advances in composite materials. Proceedings of the ICCM 3, Pergamon Press, Oxford; 1980. p. 749–58.
[12] Horii H, Nemat-Nasser S. Overall moduli of solids with microcracks: load-induced anisotropy. J Mech Phys Sol 1983;31(2):155–71.
[13] Aboudi J, Benveniste Y. The effective moduli of cracked bodies in plane deformations. Engng Fract Mech 1987;26(2):171–84.
[14] Huang Y, Hu KX, Chandra A. A generalized self-consistent mechanics method for microcracked solids. J Mech Phys Sol 1994;42(8):1273–91.
[15] Santare MH, Crocombe AD, Anlas G. Anisotropic effective moduli of materials with microcracks. Engng Fract Mech 1995;52(5):833–42.
[16] Su D, Santare MH, Gazonas GA. The effect of crack face contact on the anisotropic effective moduli of microcrack damaged media. Engng Fract Mech 2007;74(9):1436–55.
[17] Feltman RS, Santare MH. Anisotropic effective moduli of cracked short-fiber reinforced composites. J Appl Mech–Trans ASME 1999;66(3):709–13.
[18] Mori T, Tanaka K. Average stress in matrix and average elastic energy of materials with misfitting inclusions. Acta Metall 1973;21(5):571–4.
[19] Benveniste Y. On the Mori-Tanaka's method in cracked bodies. Mech Res Commun 1986;13(4):193–201.
[20] Hashin Z. The differential scheme and its application to cracked materials. J Mech Phys Sol 1988;36(6):719–34.
[21] Kachanov M. Elastic solids with many cracks and related problems. In: Hutchinson JW, Te Wu, editors. Advances in applied mechanics. Academic Press; 1993. p. 259–445.
[22] Sayers CM, Kachanov M. Microcrack-induced elastic-wave anisotropy of brittle rocks. J Geophys Res–Sol Earth 1995;100(B3):4149–56.
[23] Schubnel A, Gueguen Y. Dispersion and anisotropy of elastic waves in cracked rocks. J Geophys Res–Sol Earth 2003;108(B2).
[24] Gueguen Y, Schubnel A. Elastic wave velocities and permeability of cracked rocks. Tectonophysics 2003;370(1–4):163–76.
[25] Maurel A, Mercier JF, Lund F. Elastic wave propagation through a random array of dislocations. Phys Rev B 2004;70(2).
[26] Markov MG. Propagation of longitudinal elastic waves in a fluid-saturated porous medium with spherical inclusions. Acoust Phys 2005;51:S115–21.
[27] Levin VM, Markov MG. Elastic properties of inhomogeneous transversely isotropic rocks. Int J Sol Struct 2005;42(2):393–408.
[28] Zhang C, Gross D. Wave attenuation and dispersion in randomly cracked solids. 1. Slit cracks. Int J Engng Sci 1993;31(6):841–58.
[29] Littles JW, Jacobs LJ, Qu JM. Experimental and theoretical investigation of scattering from a distribution of cracks. Ultrasonics 1995;33(1):37–43.
[30] Kawahara J, Yamashita T. Scattering of elastic-waves by a fracture-zone containing randomly distributed cracks. Pure Appl Geophys 1992;139(1):121–44.
[31] Kelner S, Bouchon M, Coutant O. Numerical simulation of the propagation of P waves in fractured media. Geophys J Int 1999;137(1):197–206.
[32] Cemal EA, Suhubi ES. Elastodynamics. Linear theory, vol. II. New York, San Francisco, London: Academic press, INC; 1975.
[33] B.A. Auld, Acoustic fields and waves in solids vol. I. New York, London, Sydney, Toronto;1990.
[34] Eringen AC. Mechanics of continua. R.E. Krieger Publishing Co.; 1989.

Engineering Fracture Mechanics 76 (2009) 1910–1919

Contents lists available at ScienceDirect

Engineering Fracture Mechanics

journal homepage: www.elsevier.com/locate/engfracmech

Anisotropic effective moduli of microcracked materials under antiplane loading

Xu Wang [a], Michael H. Santare [a,*], George A. Gazonas [b]

[a] Department of Mechanical Engineering and Center for Composite Materials, University of Delaware, Newark, DE 19716, USA
[b] US Army Research Laboratory, Weapons and Materials Research Directorate, Aberdeen Proving Ground, MD 21005, USA

ARTICLE INFO

Article history:
Received 27 January 2009
Received in revised form 9 April 2009
Accepted 27 April 2009
Available online 5 May 2009

Keywords:
Anisotropic damage
Crack orientation distribution function
Effective moduli
Generalized self-consistent method

ABSTRACT

This study focuses on the prediction of the anisotropic effective elastic moduli of a solid containing microcracks with an arbitrary degree of alignment by using the generalized self-consistent method (GSCM). The effective elastic moduli pertaining to anti-plane shear deformation are discussed in detail. The undamaged solid can be isotropic as well as anisotropic. When the undamaged solid is isotropic, the GSCM can be realized exactly. When the undamaged solid is anisotropic it is difficult to provide an analytical solution for the crack opening displacement to be used in the GSCM, thus an approximation of the GSCM is pursued in this case. The explicit expressions of coupled nonlinear equations for the unknown effective moduli are obtained. The coupled nonlinear equations are easily solved through iteration.

1. Introduction

Microcracks are common defects in solids and multiple microcracks usually coexist in a single solid. The prediction of the effective elastic properties of a microcracked solid is technically challenging and can find many practical applications. The major methods developed so far to predict the effective elastic moduli of a microcracked solid include the following: the self-consistent method (SCM) in which a crack is embedded directly into an effective medium [1]; the generalized self-consistent method (GSCM) in which a crack is surrounded by an undamaged matrix region, and then embedded in the effective medium [2,3]; the Mori-Tanaka method (MTM) [4]; the differential scheme method (DS) [5–7]; and the modified differential scheme (MDS) [8]. Recently the GSCM in conjunction with a finite element method (FEM) was developed to take into account crack face contact and friction [9]. Most recently the representative unit cell approach was proposed by Kushch et al. [10] to calculate effective elastic properties of a microcracked solid. Here it shall be noted that the effect of crack orientation statistics on the anisotropic effective moduli of a microcracked solid was in fact first investigated by Santare et al. [3] through the introduction of the crack orientation distribution function $\phi(\theta)$ which was later adopted in [11] within the framework of the SCM to study the problem of cracks with an arbitrarily degree of alignment in a material that is originally anisotropic before the damage occurs.

In this research we analytically study the anisotropic effective elastic moduli of a solid containing microcracks with an arbitrary degree of alignment by using the GSCM. Our model is in principle based on the GSCM developed by Santare et al. [3]. In [3] the GSCM was used to predict the anisotropic moduli under plane stress loading. Here we are concerned with the effective elastic moduli pertaining to anti-plane shear deformation. In our model the undamaged material can be isotropic as well as anisotropic. An exact solution to the cracked elliptical inclusion problem, which is essential in the realization of

* Corresponding author. Tel.: +1 302 831 2246; fax: +1 302 831 3619.
E-mail address: santare@udel.edu (M.H. Santare).

0013-7944/$ - see front matter © 2009 Elsevier Ltd. All rights reserved.
doi:10.1016/j.engfracmech.2009.04.010

GSCM, can be derived when the undamaged material is isotropic. On the other hand an approximate analytical solution can still be derived when the undamaged material is anisotropic and when the crack density is not very high.

2. The effective moduli of a microcracked solid

For a microcracked solid, the strain energy relationship between the effective medium and the actual microcracked solid can be expressed as [2,3]

$$\frac{1}{2}S^*_{ijkl}\sigma^0_{kl}\sigma^0_{ij} = \frac{1}{2}S_{ijkl}\sigma^0_{kl}\sigma^0_{ij} + \frac{1}{2V}\sum_{k=1}^{M}\int_{C_k}[u_i]t^0_i \mathrm{d}C_k, \tag{1}$$

where S^*_{ijkl} is the effective compliance of the damaged material, S_{ijkl} is the compliance of the undamaged material and V is the sample volume. The above integral is the energy dissipated through the opening of each microcrack, summed over all M cracks, and σ^0_{ij} is the applied homogeneous stress field while $t^0_i = \sigma^0_{ij}n_j$ is the traction along the crack face if the crack did not exist and $[u_i]$ is the crack opening displacement. In this research we focus on the two dimensional case in which all the cracks penetrate the solid through the x_3-direction. In addition we only discuss the effective elastic moduli pertaining to anti-plane shear deformation. In the following we will address two cases: (i) the undamaged material is isotropic; (ii) the undamaged material is anisotropic.

2.1. Isotropic undamaged material

The degree of crack alignment can be described by the crack orientation distribution function $\phi(\theta)$ with θ, ($|\theta| < \pi/2$) being the angle between an individual crack and the positive x_1-axis [3]. Without losing generality, $\phi(\theta)$ can be taken as an even function of θ since we have assumed that the undamaged solid is isotropic. For simplicity, $\phi(\theta)$ is specifically given by [3,9]

$$\phi(\theta) = \begin{cases} \frac{1}{2\theta_0}, & |\theta| \le \theta_0 \\ 0, & |\theta| > \theta_0 \end{cases} \tag{2}$$

where $\theta_0 \leqslant \pi/2$. The two special cases of perfectly aligned cracks and randomly oriented cracks correspond to $\theta_0 = 0$ and $\theta_0 = \pi/2$, respectively, in Eq. (2).

Once we have introduced $\phi(\theta)$, the summation in the energy relationship Eq. (1) can be written as an integral over orientation angle θ,

$$\frac{1}{2}S^*_{ijkl}\sigma^0_{kl}\sigma^0_{ij} = \frac{1}{2}S_{ijkl}\sigma^0_{kl}\sigma^0_{ij} + \frac{M}{2A}\int_{-\theta_0}^{\theta_0}\phi(\theta)\int_{C_k}[u_i]t^0_i \mathrm{d}C_k \mathrm{d}\theta, \tag{3}$$

where A is a representative area of the sample.

In this study, we assume that the material is under anti-plane shear deformation. As a result the above energy relationship Eq. (3) can be simplified as

$$\frac{(\sigma^0_{31})^2}{2C^*_{55}} + \frac{(\sigma^0_{32})^2}{2C^*_{44}} = \frac{(\sigma^0_{31})^2 + (\sigma^0_{32})^2}{2\mu} + \frac{\eta}{2c^2}\int_{-\theta_0}^{\theta_0}\phi(\theta)\int_{C_k}[u_3]t^0_3 dC_k \mathrm{d}\theta, \tag{4}$$

where σ^0_{31} and σ^0_{32} are the anti-plane, far-field stresses, C^*_{44} and C^*_{55} are the two relevant effective moduli of the damaged material, μ is the shear modulus of the undamaged material, c is the average half crack length and $\eta = Mc^2/A$ is the crack density parameter.

If the crack did not exist, the uniform traction due to the far-field stresses, t^0_3, along the line of the crack face is given by

$$t^0_3 = \cos\theta\sigma^0_{32} - \sin\theta\sigma^0_{31}. \tag{5}$$

Next we introduce the GSCM [3] to approximately take into account the interaction between the cracks, as shown in Fig. 1. The inclusion is assumed to have the properties of the undamaged material with known elastic moduli. The surrounding matrix is composed of the effective orthotropic, damaged material with the principal directions along the x_1 and x_2 axes. The half-length of the crack is c, the semi-major and semi-minor axes of the ellipse are a and b, respectively. The crack density parameter η relates average crack length to the area of the ellipse, but in general, this leaves one of the three parameters a, b and c, unspecified. Therefore, as an additional condition, we will require $a^2 - b^2 = c^2$ to be satisfied. This is the same relationship that was used in [3] for convenience, but here it is necessary in order to make analytical solutions possible. The two-phase composite is subjected to uniform anti-plane shearing σ^0_{31} and σ^0_{32} at infinity.

By using the complex variable method [12,13], the crack opening displacement for the elliptical domain, depicted in Fig. 1, $[u_3]$ can be obtained exactly as

$$[u_3] = \frac{4\sqrt{c^2 - x^2}}{\mu[1 + \Gamma - R^{-2}(1 - \Gamma)]}\left[\frac{a\mu^* + bC^*_{55}}{(a+b)\mu^*}\cos\theta\sigma^0_{32} - \frac{a\mu^* + bC^*_{44}}{(a+b)\mu^*}\sin\theta\sigma^0_{31}\right] \quad (|x| \le c) \tag{6}$$

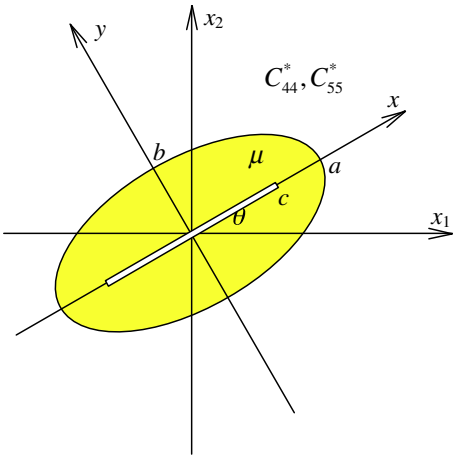

Fig. 1. The generalized self-consistent method.

where $a = \frac{c}{2}(R + R^{-1})$, $b = \frac{c}{2}(R - R^{-1})$, $(R > 1)$, $\Gamma = \mu^*/\mu$ with $\mu^* = \sqrt{C_{44}^* C_{55}^*}$. Here the parameter R, which is introduced during the analysis by using the complex variable method and conformal mapping, can be expressed in terms of a and b as $R = \sqrt{\frac{a+b}{a-b}}$. A detailed derivation can be found in the Appendix.

Consequently the integral in Eq. (4) can also be carried out exactly to arrive at the following expression

$$\frac{(\sigma_{31}^0)^2}{2C_{55}^*} + \frac{(\sigma_{32}^0)^2}{2C_{44}^*} = \frac{(\sigma_{31}^0)^2 + (\sigma_{32}^0)^2}{2\mu} + \frac{\eta}{4\mu}\left[\frac{a\mu^* + bC_{44}^*}{(a+b)\mu^*}\frac{\pi[2\theta_0 - \sin(2\theta_0)](\sigma_{31}^0)^2}{\theta_0[1 + \Gamma - R^{-2}(1-\Gamma)]} + \frac{a\mu^* + bC_{55}^*}{(a+b)\mu^*}\frac{\pi[2\theta_0 + \sin(2\theta_0)](\sigma_{32}^0)^2}{\theta_0[1 + \Gamma - R^{-2}(1-\Gamma)]}\right], \tag{7}$$

which immediately leads to the following two coupled nonlinear equations for C_{44}^* and C_{55}^* by observing the fact that σ_{31}^0 and σ_{32}^0 are arbitrary

$$\begin{aligned} \frac{\mu}{C_{55}^*} &= 1 + \frac{a\mu^* + bC_{44}^*}{(a+b)\mu^*}\frac{\pi\eta[2\theta_0 - \sin(2\theta_0)]}{2\theta_0[1 + \Gamma - R^{-2}(1-\Gamma)]}, \\ \frac{\mu}{C_{44}^*} &= 1 + \frac{a\mu^* + bC_{55}^*}{(a+b)\mu^*}\frac{\pi\eta[2\theta_0 + \sin(2\theta_0)]}{2\theta_0[1 + \Gamma - R^{-2}(1-\Gamma)]}, \end{aligned} \tag{8}$$

where $\eta = \frac{c^2}{\pi ab} = \frac{4}{\pi(R^2 - R^{-2})}$. The above set of nonlinear equations can be solved easily through iteration.

In the following we discuss in more detail some special cases for the above solution.

2.1.1. Aligned cracks ($\theta_0 = 0$)

In the case of aligned cracks, it follows from Eq. (8) that

$$\begin{aligned} C_{55}^* &= \mu, \\ \frac{1}{\Gamma^2} &= 1 + \frac{a\Gamma + b}{(a+b)\Gamma}\frac{2\pi\eta}{1 + \Gamma - R^{-2}(1-\Gamma)}, \end{aligned} \tag{9}$$

which means that there is no reduction in stiffness along the x_1-direction for aligned cracks.

When the crack density parameter is extremely low, i.e., $\eta \ll 1$, Eq. $(9)_2$ further reduces to

$$C_{44}^* = \mu/(1 + \pi\eta), \tag{10}$$

which is exactly the non-interaction approximation (NIA) for aligned cracks described by Kachanov [14].

Fig. 2 illustrates C_{44}^* calculated by using Eq. (9). The dashed line is the result of NIA. We see that the predictions of the GSCM are lower than that of NIA, especially when η is large.

2.1.2. Randomly oriented cracks ($\theta_0 = \pi/2$)

In the case of randomly oriented cracks, it follows from Eq. (8) that

$$\begin{aligned} C_{44}^* &= C_{55}^* = \mu^*, \\ \frac{1}{\Gamma} &= 1 + \frac{\pi\eta}{1 + \Gamma - R^{-2}(1-\Gamma)}, \end{aligned} \tag{11}$$

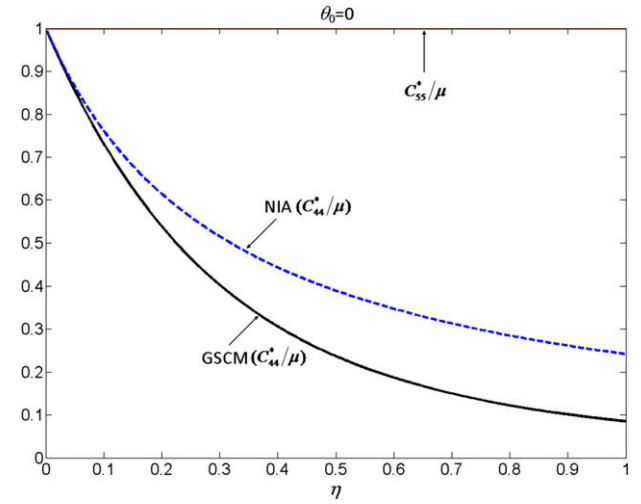

Fig. 2. The calculated C^*_{44} for an isotropic solid with perfectly aligned cracks.

through which Γ can be *exactly* determined as

$$\Gamma = \frac{-(\pi\eta - 2R^{-2}) + \sqrt{\pi^2\eta^2 + 4(1 - \pi\eta R^{-2})}}{2(1 + R^{-2})}. \tag{12}$$

Eq. $(11)_1$ shows that the effective material properties are still *isotropic* when the cracks are randomly oriented. In addition when the crack density parameter is extremely low, i.e., $\eta \ll 1$, Eq. $(11)_2$ further reduces to

$$\mu^* = \mu/(1 + 0.5\pi\eta), \tag{13}$$

which is again, the NIA described by Kachanov, this time for randomly oriented cracks [14].

Fig. 3 shows μ^* calculated by using Eq. (12). The dashed line is the result of NIA. We observe a similar behavior here to that of C^*_{44} for aligned cracks. We also observe that the values of μ^* for a solid with randomly oriented cracks are higher than those of C^*_{44} for a solid with aligned cracks.

2.1.3. An arbitrary degree of alignment ($0 < \theta_0 < \pi/2$)

The present model can be used conveniently to predict the anisotropic effective moduli of a solid containing microcracks with an arbitrary degree of alignment through the introduction of the crack orientation distribution function $\phi(\theta)$.

We demonstrate in Figs. 4 and 5 the predicted values of C^*_{44} and C^*_{55} as functions of η for five different values of $\theta_0 = \pi/16$, $\pi/6$, $\pi/4$, $\pi/3$, $\pi/2$. It is clear from the two figures that a decrease in θ_0 will result in a decrease in C^*_{44} and an increase in C^*_{55}.

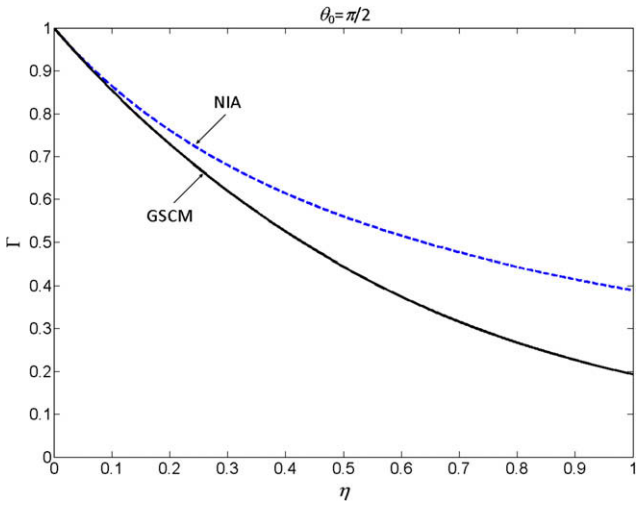

Fig. 3. The calculated $\mu^* = C^*_{44} = C^*_{55}$ for an isotropic solid with randomly oriented cracks.

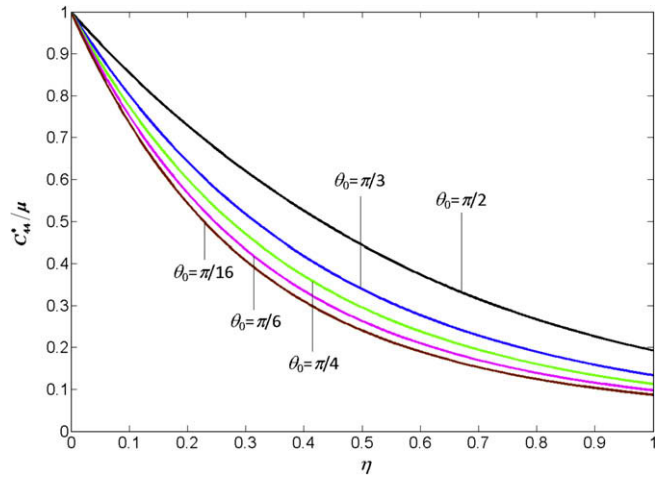

Fig. 4. The predicted values of C^*_{44} for a cracked isotropic solid as a function of η for five different values of θ_0.

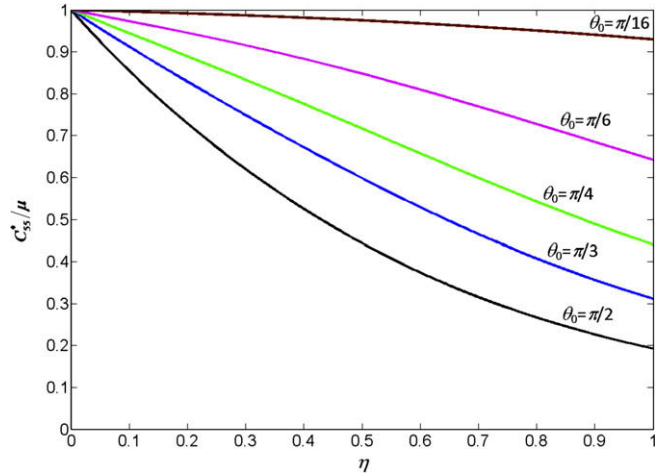

Fig. 5. The predicted values of C^*_{55} for a cracked isotropic solid as a function of η for five different values of θ_0.

The anisotropy of the effective medium monotonically increases as θ_0 decreases from $\pi/2$ (for randomly oriented cracks) to zero (for perfectly aligned cracks).

Due to the fact that the parameter $\mu^* = \sqrt{C^*_{44}C^*_{55}}$ is an invariant under coordinate rotation, it can be considered as a measure of the overall stiffness of the cracked material. Therefore, it is of interest to check how μ^* is influenced by θ_0 and η. We demonstrate in Fig. 6 the predicted values of μ^* as a function of η for four different values of θ_0. It is observed that an increase in θ_0 will cause a decrease in the overall stiffness characterized by μ^*, especially when the crack density η is large. This fact can be more clearly observed in Fig. 7 in which μ^* is plotted as a function of θ_0 for six different values of η. Figs. 6 and 7 demonstrate that for a microcracked solid, randomly oriented cracks ($\theta_0 = \pi/2$) gives the *lowest stiffness* among all possible crack orientation distributions, while aligned cracks ($\theta_0 = 0$) gives the *greatest stiffness*.

2.2. Anisotropic undamaged material

In the previous discussion we have assumed that the undamaged material is isotropic. Next we consider the more complex situation in which the undamaged material is anisotropic. Without losing generality we can assume that the intact material is orthotropic with its principal directions along the x_1 and x_2 axes, respectively. When the intact material is orthotropic, we cannot necessarily take the crack orientation distribution function $\phi(\theta)$ as an even function of θ. Here $\phi(\theta)$ takes the following form

$$\phi(\theta) = \begin{cases} \frac{1}{\theta_2-\theta_1}, & \theta_1 \le \theta \le \theta_2 \\ 0, & \theta > \theta_2 \text{ or } \theta < \theta_1 \end{cases} \tag{14}$$

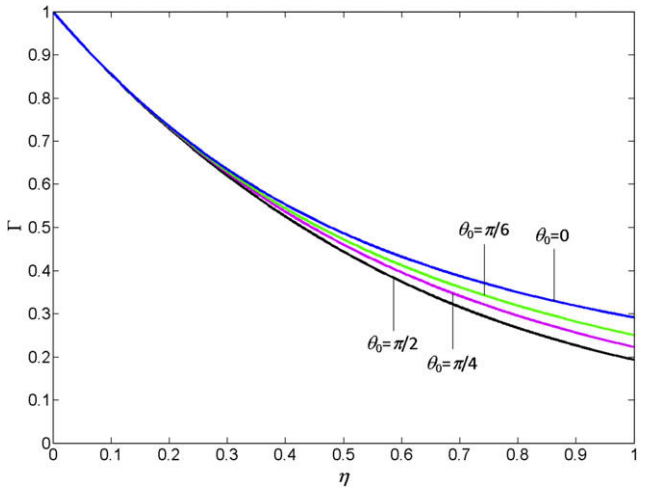

Fig. 6. The predicted values of μ^* for a cracked isotropic solid as a function of η for four different values of θ_0.

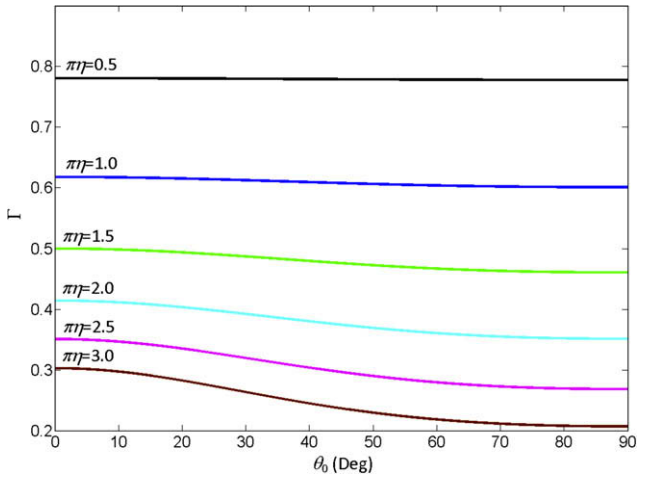

Fig. 7. The predicted values of μ^* for a cracked isotropic solid as a function of θ_0 for six different values of η.

where $|\theta_1|$, $|\theta_2| \leqslant \pi$ and $\theta_2 - \theta_1 \leqslant \pi$. The definition region of θ in Eq. (14) has been enlarged relative to Eq. (2), to $|\theta| \leqslant \pi$ to incorporate the complex situation in which the average orientation of the cracks $\theta = (\theta_1 + \theta_2)/2$ may be *arbitrary* with respect to the x_1, x_2 axes. In this case, perfectly aligned cracks and randomly oriented cracks correspond to $\theta_1 = \theta_2$ and $\theta_2 = -\theta_1 = \pi/2$ (or more generally but equivalently $\theta_2 - \theta_1 = \pi$), respectively, in Eq. (14).

Now we can write the energy relationship in Eq. (3) as follows

$$\frac{C^*_{44}(\sigma^0_{31})^2}{2\mu^{*2}} - \frac{C^*_{45}\sigma^0_{31}\sigma^0_{32}}{\mu^{*2}} + \frac{C^*_{55}(\sigma^0_{32})^2}{2\mu^{*2}} = \frac{(\sigma^0_{31})^2}{2C_{55}} + \frac{(\sigma^0_{32})^2}{2C_{44}} + \frac{\eta}{2c^2}\int_{\theta_1}^{\theta_2}\phi(\theta)\int_{C_k}[u_3]t^0_3 dC_k \mathrm{d}\theta, \tag{15}$$

where σ^0_{31} and σ^0_{32} are the anti-plane, far-field stresses, C^*_{44}, C^*_{55} and C^*_{45} are the three relevant effective moduli of the damaged material, $\mu^* = \sqrt{C^*_{44}C^*_{55} - C^{*2}_{45}} > 0$ and C_{44} and C_{55} are the two material moduli of the undamaged material. When the undamaged material is anisotropic, it may very well be impossible to calculate exact values for $[u_3]$ using the boundary-value problem shown in Fig. 1. Therefore, in the following we use an approximation to the BVP to calculate $[u_3]$. When the crack density parameter is relatively low, we have $R \gg 1$ or equivalently $a \approx b \gg c$. As a result, $[u_3]$ can be obtained approximately through the following method: (i) first calculate the uniform stress field within an uncracked *circular* inclusion with material moduli C_{44} and C_{55} surrounded by the effective medium with material moduli C^*_{44}, C^*_{55} and C^*_{45} [15,16]; (ii) then solve the problem of a crack in an infinite homogeneous material with material moduli C_{44} and C_{55} subjected to the remote loading which is equal to the internal uniform stress field obtained in (i). By using this method we obtain the following approximate expression of $[u_3]$

$$[u_3] = \frac{2\sqrt{c^2-x^2}}{\mu}\left[\frac{2C_{44}}{\mu+C_{44}}\frac{(\mu^*+C^*_{55})\sigma^0_{32}-C^*_{45}\sigma^0_{31}}{\mu^*[1+\Gamma+\rho(1-\Gamma)]}\cos\theta - \frac{2\mu}{\mu+C_{44}}\frac{(\mu^*+C^*_{44})\sigma^0_{31}-C^*_{45}\sigma^0_{32}}{\mu^*[1+\Gamma-\rho(1-\Gamma)]}\sin\theta\right] \quad (|x|\le c) \tag{16}$$

where $\rho = \frac{\sqrt{C_{44}}-\sqrt{C_{55}}}{\sqrt{C_{44}}+\sqrt{C_{55}}}$, $\mu = \sqrt{C_{44}C_{55}}$ and $\Gamma = \mu^*/\mu$.

The integral in Eq. (15) can now be carried out to arrive at the following relationship

$$\begin{aligned}
&\frac{C^*_{44}(\sigma^0_{31})^2}{2\mu^{*2}} - \frac{C^*_{45}\sigma^0_{31}\sigma^0_{32}}{\mu^{*2}} + \frac{C^*_{55}(\sigma^0_{32})^2}{2\mu^{*2}} = \frac{(\sigma^0_{31})^2}{2C_{55}} + \frac{(\sigma^0_{32})^2}{2C_{44}} + \frac{\pi\eta}{2\mu(\theta_2-\theta_1)}\\
&\times\left[\frac{C_{44}}{2(\mu+C_{44})}\frac{(\mu^*+C^*_{55})(\sigma^0_{32})^2 - C^*_{45}\sigma^0_{31}\sigma^0_{32}}{\mu^*[1+\Gamma+\rho(1-\Gamma)]}[2(\theta_2-\theta_1)+\sin(2\theta_2)-\sin(2\theta_1)]\right.\\
&+\frac{\mu}{2(\mu+C_{44})}\frac{(\mu^*+C^*_{44})(\sigma^0_{31})^2 - C^*_{45}\sigma^0_{31}\sigma^0_{32}}{\mu^*[1+\Gamma-\rho(1-\Gamma)]}[2(\theta_2-\theta_1)-\sin(2\theta_2)+\sin(2\theta_1)]\\
&\left.-\left[\frac{\mu}{\mu+C_{44}}\frac{(\mu^*+C^*_{44})\sigma^0_{31}\sigma^0_{32} - C^*_{45}(\sigma^0_{32})^2}{\mu^*[1+\Gamma-\rho(1-\Gamma)]} + \frac{C_{44}}{\mu+C_{44}}\frac{(\mu^*+C^*_{55})\sigma^0_{31}\sigma^0_{32} - C^*_{45}(\sigma^0_{31})^2}{\mu^*[1+\Gamma+\rho(1-\Gamma)]}\right][\sin^2\theta_2-\sin^2\theta_1]\right].
\end{aligned} \tag{17}$$

In view of the fact that σ^0_{31} and σ^0_{32} are arbitrary, we arrive at the following three coupled, nonlinear equations for C^*_{44}, C^*_{55} and C^*_{45}

$$\begin{aligned}
\frac{C^*_{44}}{\mu^{*2}} &= \frac{1}{C_{55}} + \frac{\pi\eta}{\mu^*(\theta_2-\theta_1)(\mu+C_{44})}\left[\frac{(\mu^*+C^*_{44})[2(\theta_2-\theta_1)-\sin(2\theta_2)+\sin(2\theta_1)]}{2[1+\Gamma-\rho(1-\Gamma)]} + \frac{C_{44}C^*_{45}[\sin^2\theta_2-\sin^2\theta_1]}{\mu[1+\Gamma+\rho(1-\Gamma)]}\right],\\
\frac{C^*_{55}}{\mu^{*2}} &= \frac{1}{C_{44}} + \frac{\pi\eta}{\mu^*(\theta_2-\theta_1)(\mu+C_{44})}\left[\frac{C_{44}(\mu^*+C^*_{55})[2(\theta_2-\theta_1)+\sin(2\theta_2)-\sin(2\theta_1)]}{2\mu[1+\Gamma+\rho(1-\Gamma)]} + \frac{C^*_{45}[\sin^2\theta_2-\sin^2\theta_1]}{1+\Gamma-\rho(1-\Gamma)}\right],\\
\frac{C^*_{45}}{\mu^{*2}} &= \frac{\pi\eta}{2\mu^*(\theta_2-\theta_1)(\mu+C_{44})}\left[\frac{C_{44}C^*_{45}[2(\theta_2-\theta_1)+\sin(2\theta_2)-\sin(2\theta_1)]}{2\mu[1+\Gamma+\rho(1-\Gamma)]} + \frac{C^*_{45}[2(\theta_2-\theta_1)-\sin(2\theta_2)+\sin(2\theta_1)]}{2[1+\Gamma-\rho(1-\Gamma)]}\right.\\
&\quad\left.+\left[\frac{\mu^*+C^*_{44}}{1+\Gamma-\rho(1-\Gamma)} + \frac{C_{44}(\mu^*+C^*_{55})}{\mu[1+\Gamma+\rho(1-\Gamma)]}\right][\sin^2\theta_2-\sin^2\theta_1]\right],
\end{aligned} \tag{18}$$

which can also be solved easily through iteration. We see from Eq. (18) that when $\phi(\theta)$, defined by Eq. (14), is an even function of θ, i.e., $\theta_1 = -\theta_2$, then the effective medium will be orthotropic with $C^*_{45} = 0$. In other words, when the average orientation of the cracks is zero the undamaged material and the effective medium will possess the same principal axes. In the following we concentrate our discussion on the effective elastic moduli of a solid containing perfectly aligned cracks and one containing randomly oriented cracks, respectively.

2.2.1. Aligned cracks ($\theta_1 = \theta_2$)

When the cracks are perfectly aligned, we have $\theta_1 = \theta_2$ and both the numerator and denominator in the right hand side of Eq. (18) vanish. In this case applying the L'Hospital's rule to Eq. (18) when $\theta_2 \to \theta_1$ yields the following:

$$\begin{aligned}
\frac{C^*_{44}}{\mu^{*2}} &= \frac{1}{C_{55}} + \frac{\pi\eta}{\mu^*(\mu+C_{44})}\left[\frac{(\mu^*+C^*_{44})[1-\cos(2\theta_1)]}{1+\Gamma-\rho(1-\Gamma)} + \frac{C_{44}C^*_{45}\sin(2\theta_1)}{\mu[1+\Gamma+\rho(1-\Gamma)]}\right],\\
\frac{C^*_{55}}{\mu^{*2}} &= \frac{1}{C_{44}} + \frac{\pi\eta}{\mu^*(\mu+C_{44})}\left[\frac{C_{44}(\mu^*+C^*_{55})[1+\cos(2\theta_1)]}{\mu[1+\Gamma+\rho(1-\Gamma)]} + \frac{C^*_{45}\sin(2\theta_1)}{1+\Gamma-\rho(1-\Gamma)}\right],\\
\frac{C^*_{45}}{\mu^{*2}} &= \frac{\pi\eta}{2\mu^*(\mu+C_{44})}\left[\frac{C_{44}C^*_{45}[1+\cos(2\theta_1)]}{\mu[1+\Gamma+\rho(1-\Gamma)]} + \frac{C^*_{45}[1-\cos(2\theta_1)]}{1+\Gamma-\rho(1-\Gamma)} + \left[\frac{\mu^*+C^*_{44}}{1+\Gamma-\rho(1-\Gamma)} + \frac{C_{44}(\mu^*+C^*_{55})}{\mu[1+\Gamma+\rho(1-\Gamma)]}\right]\sin(2\theta_1)\right].
\end{aligned} \tag{19}$$

Now, we can further look into two special cases of the above formulation: the cracks are aligned horizontally ($\theta_1 = \theta_2 = 0$) and the cracks are aligned vertically ($\theta_1 = \theta_2 = \pi/2$). When $\theta_1 = \theta_2 = 0$, it follows from Eq. (19) that

$$\begin{aligned}
&C^*_{45} = 0, \quad C^*_{55} = C_{55},\\
&\frac{1}{C^*_{44}} = \frac{1}{C_{44}} + \frac{2\pi\eta C_{44}(\mu^*+C_{55})}{\mu^*\mu(\mu+C_{44})[1+\Gamma+\rho(1-\Gamma)]},
\end{aligned} \tag{20}$$

which means that there is no reduction in stiffness along the x_1-direction for horizontally aligned cracks.

On the other hand when $\theta_1 = \theta_2 = \pi/2$, it follows from Eq. (19) that

$$\begin{aligned}
&C^*_{45} = 0, \quad C^*_{44} = C_{44},\\
&\frac{1}{C^*_{55}} = \frac{1}{C_{55}} + \frac{2\pi\eta(\mu^*+C_{44})}{\mu^*(\mu+C_{44})[1+\Gamma-\rho(1-\Gamma)]},
\end{aligned} \tag{21}$$

which means that there is no reduction in stiffness along the x_2-direction for vertically aligned cracks.

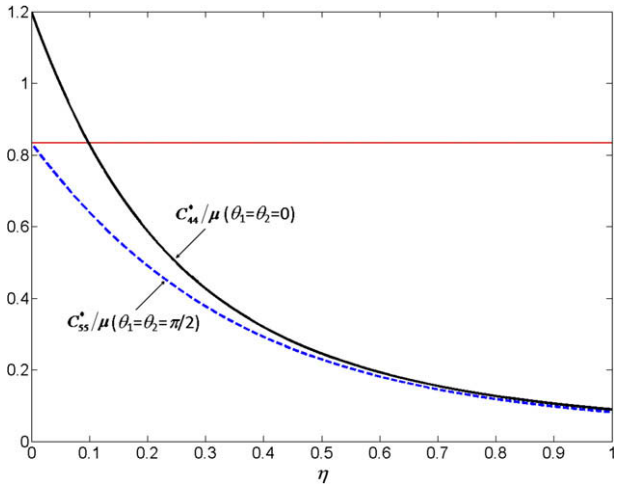

Fig. 8. The variations of C^*_{44} ($\theta_1 = \theta_2 = 0$) and C^*_{55} ($\theta_1 = \theta_2 = \pi/2$) for an orthotropic solid $C_{44} = 1.2\mu$ and $C_{55} = 0.8333\mu$ containing perfectly aligned cracks as functions of η.

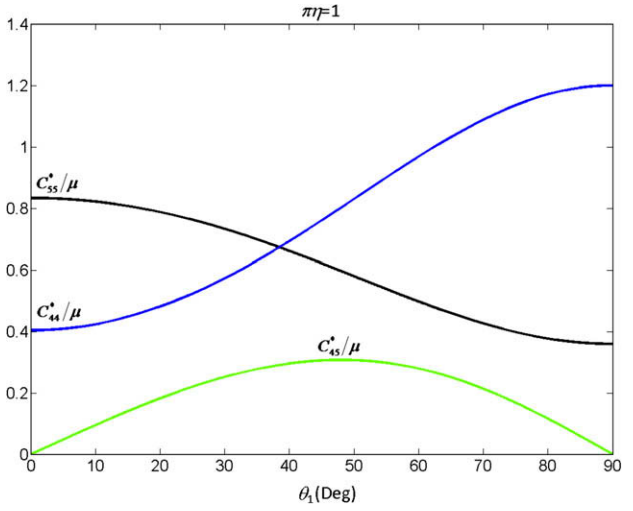

Fig. 9. The variations of C^*_{44}, C^*_{55} and C^*_{45} as functions of θ_1 ($=\theta_2$) for an orthotropic solid $C_{44} = 1.2\mu$ and $C_{55} = 0.8333\mu$ containing perfectly aligned cracks with $\eta = 1/\pi$.

Fig. 8 illustrates the variations of C^*_{44} for $\theta_1 = \theta_2 = 0$ and C^*_{55} for $\theta_1 = \theta_2 = \pi/2$ as functions of η. To plot the results on one graph, the undamaged anisotropic moduli are specifically chosen as $C_{44} = 1.2\mu$ and $C_{55} = 0.8333\mu$. It is interesting to observe that C^*_{44} for $\theta_1 = \theta_2 = 0$ and C^*_{55} for $\theta_1 = \theta_2 = \pi/2$, both of which are decreasing functions of η, converge to basically the same value as $\eta \to 1$. We also observe that the effective material is *isotropic* ($C^*_{44} = C^*_{55} = 0.8333\mu$) at low crack density $\eta \approx 0.10$ for horizontally aligned cracks ($\theta_1 = \theta_2 = 0$).

We can also see from Eq. (19) that when the cracks are not aligned horizontally or vertically, the principal directions of the anisotropic effective medium are no longer the same as those of the undamaged material. We illustrate in Fig. 9, the variations of C^*_{44}, C^*_{55} and C^*_{45} as functions of θ_1 ($=\theta_2$) for an orthotropic solid with undamaged moduli, $C_{44} = 1.2\mu$ and $C_{55} = 0.8333\mu$ containing aligned cracks with $\eta = 1/\pi$. We observe from Fig. 9 that: (i) C^*_{45} attains a maximum value of $C^*_{45} = 0.3073\mu$ at $\theta_1 = 48^\circ$ (the reason why C^*_{45} does not attain its maximum value at 45° is due to the anisotropy of the undamaged material); (ii) C^*_{44} is an increasing function and C^*_{55} is a decreasing function of θ_1. As expected $C^*_{44} = C_{44} = 1.2\mu$ for vertically aligned cracks ($\theta_1 = 90^\circ$) and $C^*_{55} = C_{55} = 0.8\mu$ for horizontally aligned cracks ($\theta_1 = 0$). More interestingly, our numerical results also verify that the effective compliance constants $\widetilde{S}^*_{45} = -\widetilde{C}^*_{45}/\mu^{*2}$ and $\widetilde{S}^*_{55} = \widetilde{C}^*_{44}/\mu^{*2}$ in the Cartesian coordinate system (x'_1, x'_2), which is rotated by the crack alignment angle θ_1 with respect to the principal coordinate system (x_1, x_2), are exactly the same as the compliance constants $\widetilde{S}_{45} = -\widetilde{C}_{45}/\mu^2$ and $\widetilde{S}_{55} = \widetilde{C}_{44}/\mu^2$ for the undamaged material in the same coordinate system (x'_1, x'_2) .

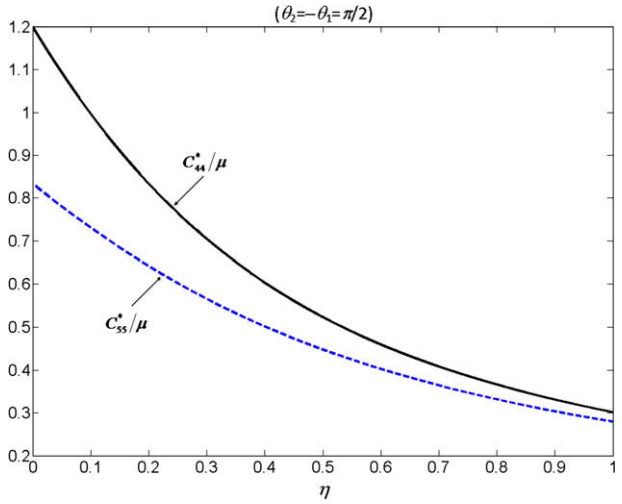

Fig. 10. The variations of C^*_{44} and C^*_{55} for an orthotropic solid $C_{44} = 1.2\mu$ and $C_{55} = 0.8333\mu$ containing randomly oriented cracks as functions of η.

2.2.2. Randomly oriented cracks ($\theta_2 = -\theta_1 = \pi/2$)

When the cracks are randomly oriented, Eq. (18) reduces to

$$\begin{aligned} C^*_{45} &= 0, \\ \frac{1}{C^*_{55}} &= \frac{1}{C_{55}} + \frac{\pi\eta(\mu^* + C^*_{44})}{\mu^*(\mu + C_{44})[1 + \Gamma - \rho(1-\Gamma)]}, \\ \frac{1}{C^*_{44}} &= \frac{1}{C_{44}} + \frac{\pi\eta C_{44}(\mu^* + C^*_{55})}{\mu^*\mu(\mu + C_{44})[1 + \Gamma + \rho(1-\Gamma)]}. \end{aligned} \tag{22}$$

From the above expressions, we can see that $C^*_{44} \neq C^*_{55}$ when $C_{44} \neq C_{55}$ even when the cracks are randomly oriented. To illustrate this fact more clearly we present in Fig. 10, the variations of C^*_{44} and C^*_{55} for an orthotropic solid containing randomly oriented cracks as functions of η. The undamaged anisotropic moduli are chosen as $C_{44} = 1.2\mu$ and $C_{55} = 0.8333\mu$. It is clear that $C^*_{44} > C^*_{55}$, and in addition the difference in C^*_{44} and C^*_{55} decreases as the crack density increases.

Finally it is of interest to point out that when the undamaged material is *isotropic*, our calculations show that the result by using the approximation of the GSCM always lies between that by using the exact GSCM and that by using NIA. In view of the fact that the GSCM is only an approximate scheme to account for crack interactions, the predictions derived by using the GSCM are not necessarily more *accurate* than those derived by using an approximation to the GSCM.

3. Conclusions

By means of the GSCM, we analytically investigated the anisotropic effective moduli of a cracked solid subjected to anti-plane shear deformation. When the undamaged solid is isotropic, the two coupled, nonlinear equations for the two effective moduli C^*_{44} and C^*_{55} were obtained and shown in Eq. (8). When the undamaged solid is anisotropic, the three coupled nonlinear equations for the three effective moduli C^*_{44}, C^*_{55} and C^*_{45} were derived and shown in Eq. (18). Detailed numerical results were presented to illustrate how the anisotropic effective moduli are influenced by various degrees of crack alignment (characterized by θ_0 for the isotropic undamaged material or θ_1 and θ_2 for the anisotropic undamaged material) and crack density (characterized by η).

Acknowledgements

The three referees' comments and suggestions on revising the initial manuscript are highly appreciated. This research was supported by the United States Army Research Laboratory through the Composite Materials Technology cooperative agreement with the Center for Composite Materials at the University of Delaware.

Appendix A. Detailed derivation of Eq. (6)

It is convenient to solve the boundary-value problem in the Cartesian coordinate system (x, y, z) with $z = x_3$, as shown in Fig. 1. First the remote uniform loading σ^0_{zx} and σ^0_{zy} can be written as

$$\begin{aligned}\sigma^0_{zx} &= \sigma^0_{31}\cos\theta + \sigma^0_{32}\sin\theta,\\ \sigma^0_{zy} &= \sigma^0_{32}\cos\theta - \sigma^0_{31}\sin\theta.\end{aligned} \tag{A1}$$

Secondly the effective moduli of the damaged material in the (x, y, z) coordinate system, $\widetilde{C}^*_{44}$, $\widetilde{C}^*_{55}$ and $\widetilde{C}^*_{45}$ can be derived as

$$\begin{aligned}\widetilde{C}^*_{55} &= C^*_{55}\cos^2\theta + C^*_{44}\sin^2\theta,\\ \widetilde{C}^*_{44} &= C^*_{44}\cos^2\theta + C^*_{55}\sin^2\theta,\\ \widetilde{C}^*_{45} &= (C^*_{44} - C^*_{55})\cos\theta\sin\theta.\end{aligned} \tag{A2}$$

Due to the fact that the cracked elliptical inclusion is isotropic, if one is only concerned with the field within the inclusion, it is sufficient to treat the matrix as *isotropic* with shear modulus μ^* subject to *virtual* remote uniform shear stresses $\tilde{\sigma}^0_{zx}$ and $\tilde{\sigma}^0_{zy}$ such that [13]

$$\tilde{\sigma}^0_{zx} - \mathrm{i}\tilde{\sigma}^0_{zy} = \frac{(a - \mathrm{i}pb)(\sigma^0_{zx} + \bar{p}\sigma^0_{zy})}{(a+b)\mathrm{Im}\{p\}}, \tag{A3}$$

where the complex constant p is given by

$$p = \frac{-\widetilde{C}^*_{45} + \mathrm{i}\mu^*}{\widetilde{C}^*_{44}} = \frac{(C^*_{55} - C^*_{44})\cos\theta\sin\theta + \mathrm{i}\sqrt{C^*_{44}C^*_{55}}}{C^*_{44}\cos^2\theta + C^*_{55}\sin^2\theta}. \tag{A4}$$

Here we are only interested in the expression for $\tilde{\sigma}^0_{zy}$ since the loading $\tilde{\sigma}^0_{zx}$ will not induce any crack opening displacement. It follows from Eqs. (A1), (A3), and (A4) that

$$\begin{aligned}\tilde{\sigma}^0_{zy} &= \frac{b\mathrm{Re}\{p\}\sigma^0_{31} + [a\mathrm{Im}\{p\} + b|p|^2]\sigma^0_{32}}{(a+b)\mathrm{Im}\{p\}}\cos\theta + \frac{b\mathrm{Re}\{p\}\sigma^0_{32} - [a\mathrm{Im}\{p\} + b|p|^2]\sigma^0_{31}}{(a+b)\mathrm{Im}\{p\}}\sin\theta\\ &= \frac{a\mu^* + bC^*_{55}}{(a+b)\mu^*}\cos\theta\sigma^0_{32} - \frac{a\mu^* + bC^*_{44}}{(a+b)\mu^*}\sin\theta\sigma^0_{31}.\end{aligned} \tag{A5}$$

On the other hand it can be deduced from Ref. [12] that the crack opening displacement $[u_3]$ due to remote uniform loading $\tilde{\sigma}^0_{zy}$ can be expressed as

$$[u_3] = \frac{4\tilde{\sigma}^0_{zy}\sqrt{c^2 - x^2}}{\mu[1 + \Gamma - R^{-2}(1-\Gamma)]} \quad (|x| \le c). \tag{A6}$$

Starting with Eqs. (A5) and (A6), we can easily arrive at Eq. (6).

References

[1] Budiansky B, O'Connel RJ. Elastic moduli of a cracked solid. Int J Solid Struct 1976;12:81–97.
[2] Aboudi J, Benveniste Y. The effective moduli of cracked bodies in plane deformations. Engng Fract Mech 1987;26(2):171–84.
[3] Santare MH, Crocombe AD, Anlas G. Anisotropic effective moduli of materials with microcracks. Engng Fract Mech 1995;52(5):833–42.
[4] Benveniste Y. On the Mori-Tanaka's method in cracked bodies. Mech Res Commun 1986;13:193–201.
[5] Salganik RL. Mechanics of bodies with many cracks. Mech Solid 1973;8:135–43 [English translation].
[6] Zimmerman RW. The effect of microcracks on the elastic moduli of brittle materials. J Mater Sci-Lett 1985;4:1457–60.
[7] Hashin Z. The differential scheme and its application to cracked materials. J Mech Phys Solid 1988;13:193–201.
[8] Sayers C, Kachanov M. A simple technique for finding effective elastic constants of cracked solids for arbitrary crack orientation statistics. Int J Solid Struct 1991;7:671–80.
[9] Su D, Santare MH, Gazonas GA. The effect of crack face contact on the anisotropic effective moduli of microcrack damaged media. Engng Fract Mech 2007;74:1436–55.
[10] Kushch VI, Sevostianov I, Mishnaevsky L. Effect of crack orientation statistics on effective stiffness of microcracked solid. Int J Solid Struct 2009;46:1574–88.
[11] Feltman RS, Santare MH. Anisotropic effective moduli of cracked short fiber reinforced composites. ASME J Appl Mech 1999;66:709–13.
[12] Wu CH, Chen CH. A crack in a confocal elliptic inhomogeneity embedded in an infinite medium. ASME J Appl Mech 1990;57:91–6.
[13] Wang X, Pan E. Antiplane shear deformations of an anisotropic elliptical inhomogeneity with imperfect or viscous interface. Z Angew Math Mech (ZAMM) 2008;88:142–50.
[14] Kachanov M. Effective elastic properties of cracked solids: critical review of some basic concept. Appl Mech Rev 1992;45(8):304–35.
[15] Ting TCT. Anisotropic elasticity—theory and applications. New York: Oxford University Press; 1996.
[16] Kattis MA, Providas E. Two-phase potentials in anisotropic elasticity: antiplane deformation. Int J Engng Sci 1998;36:801–11.

Int J Fract (2009) 158:27–40
DOI 10.1007/s10704-009-9363-2

ORIGINAL PAPER

On the effective electroelastic properties of microcracked generally anisotropic solids

Xu Wang · George A. Gazonas · Michael H. Santare

Received: 9 March 2009 / Accepted: 20 May 2009 / Published online: 9 June 2009

Abstract In this study we first obtain the explicit expressions for the 15 effective reduced elastic compliances of an elastically anisotropic solid containing multiple microcracks with an arbitrary degree of alignment under two-dimensional deformations within the framework of the non-interaction approximation (NIA). Under special situations, our results can reduce to the classical ones derived by Bristow (J Appl Phys 11: 81–85, 1960), and Mauge and Kachanov (J Mech Phys Solids 42(4):561–584, 1994). Some interesting phenomena are also observed. For example, when the undamaged solid is orthotropic, the effective in-plane shear modulus is dependent on the degree of the crack alignment. The NIA method is then extended to obtain the effective electroelastic properties of an anisotropic piezoelectric solid containing two-dimensional insulating, permeable or conducting microcracks with an arbitrary degree of alignment. We also derive a set of fifteen coupled nonlinear equations for the unknown effective reduced elastic compliances of a microcracked, anisotropic, elastic solid by using the generalized self-consistent method (GSCM). The set of coupled nonlinear equations can be solved through iteration.

Keywords Non-interaction approximation · Effective properties · Microcracks · Elastic material · Piezoelectric material

X. Wang · M. H. Santare
Department of Mechanical Engineering and Center for Composite Materials, University of Delaware, Newark, DE 19716, USA

G. A. Gazonas (✉)
US Army Research Laboratory, Weapons and Materials Research Directorate, Aberdeen Proving Ground, Aberdeen, MD, 21005, USA
e-mail: gazonas@arl.army.mil

1 Introduction

The prediction of the effective elastic properties of anisotropic materials containing microcracks has been a topic of micromechanics for nearly 30 years (see for example, Gottesman et al. 1980; Hashin 1988; Mauge and Kachanov 1994; Feltman and Santare 1999; among others). The limitations of the previous works lie in the following: (i) the two-dimensional, anisotropic matrix studied so far is confined to the special case in which the in-plane deformations and the out-of-plane deformations are decoupled (see for example, Mauge and Kachanov 1994); (ii) in most of the studies the microcracks were assumed to be either perfectly aligned or randomly oriented (Mauge and Kachanov 1994).

In this study we first address the problem of the effective elastic properties of a generally anisotropic elastic matrix containing microcracks with an arbitrary degree of alignment under two-dimensional deformations. Here we consider any degree of crack alignment, from perfectly aligned to completely random, through the introduction of a crack orientation distribution function (Santare et al. 1995). Very concise expressions for

the effective reduced elastic compliances of the cracked material are obtained by making use of energy considerations and by ignoring crack interactions. During the development, we adopt some results (for example, the crack opening displacement) based on the Stroh formalism for two-dimensional anisotropic elasticity (Ting 1996). The current result based on a non-interaction approximation (NIA) still retains accuracy at substantially higher crack densities due to the cancellation of the competing interaction effects of shielding and antishielding (Kachanov 1992; Mauge and Kachanov 1994; Kachanov 2007). The NIA method is then extended to study the effective electroelastic properties of a microcracked, anisotropic, piezoelectric solid. Here the microcracks can be insulating (Pak 1990; Suo et al. 1992), permeable (Suo et al. 1992) or conducting (McMeeking 1987; Suo 1993). It is of interest to point out that the non-convex electric enthalpy used for insulating cracks is different than the convex energy density function used for conducting cracks. The effective elastic moduli of a microcracked, generally anisotropic elastic solid are also discussed within the framework of the generalized self-consistent method (GSCM), which approximately takes into account crack interaction (Aboudi and Benveniste 1987; Santare et al. 1995). It is found that some observations made by using the NIA assumption are no longer valid when using the GSCM.

2 The theory within the framework of NIA

The strain energy balance equation for a microcracked, elastically anisotropic solid can be expressed as (Eshelby 1956; Benveniste 1985; Aboudi and Benveniste 1987)

$$\frac{1}{2}S^*_{ijkl}\sigma^0_{kl}\sigma^0_{ij}=\frac{1}{2}S_{ijkl}\sigma^0_{kl}\sigma^0_{ij}+\frac{1}{2V}\sum_{k=1}^{M}\int_{C_k}[u_i]t^0_i\mathrm{d}C_k, \tag{1}$$

where S^*_{ijkl} is the effective compliance of the damaged material, S_{ijkl} is the compliance of the undamaged material, V is the sample volume, M is the number of microcracks within the solid, σ^0_{ij} is the applied homogeneous stress field while $t^0_i = \sigma^0_{ij}n_j$ is the traction along the crack face if the crack did not exist and $[u_i]$ is the crack opening displacement.

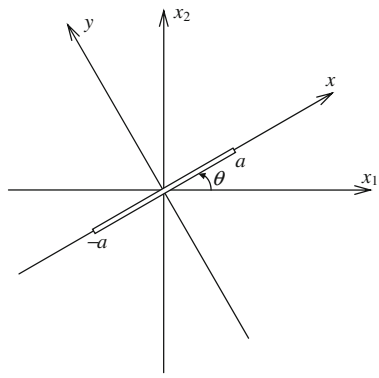

Fig. 1 A crack of half crack length a oriented at an angle θ to the positive x_1-axis

In this study we assume that all the cracks penetrate the solid through the x_3-axis. The degree of crack alignment can be described by the crack orientation distribution function $\phi(\theta)$ with θ, $(|\theta| < \pi/2)$ being the angle between an individual crack and the positive x_1-axis as shown in Fig. 1 (Santare et al. 1995). Without losing generality, $\phi(\theta)$ can be taken as an even function of θ such that the average orientation is parallel to the x_1-axis. For simplicity, $\phi(\theta)$ is specifically given by (Santare et al. 1995; Wang et al. 2009)

$$\phi(\theta) = \begin{cases} \frac{1}{2\theta_0}, & |\theta| \le \theta_0 \\ 0, & |\theta| > \theta_0 \end{cases} \tag{2}$$

where $\theta_0 \le \pi/2$. The two special cases of perfectly aligned cracks and randomly oriented cracks correspond to $\theta_0 = 0$ and $\theta_0 = \pi/2$, respectively in Eq. 2.

As a result, under two-dimensional deformations in which the displacements depend on x_1 and x_2 only, Eq. 1 can be further expressed as (Santare et al. 1995; Ting 1996)

$$\frac{1}{2}(\boldsymbol{\sigma}^0)^T\mathbf{S}'^*\boldsymbol{\sigma}^0 = \frac{1}{2}(\boldsymbol{\sigma}^0)^T\mathbf{S}'\boldsymbol{\sigma}^0 + \frac{M}{2A}\int_{-\theta_0}^{\theta_0}\phi(\theta)\int_{C_k}(\mathbf{t}^0)^T[\mathbf{u}]\mathrm{d}C_k\mathrm{d}\theta, \tag{3}$$

where A is the sample area, and

$$\boldsymbol{\sigma}^0 = \left[\sigma^0_{11}\quad \sigma^0_{22}\quad \sigma^0_{23}\quad \sigma^0_{13}\quad \sigma^0_{12}\right]^T, \tag{4}$$

$$\mathbf{S}' = \begin{bmatrix} S'_{11} & S'_{12} & S'_{14} & S'_{15} & S'_{16} \\ S'_{12} & S'_{22} & S'_{24} & S'_{25} & S'_{26} \\ S'_{14} & S'_{24} & S'_{44} & S'_{45} & S'_{46} \\ S'_{15} & S'_{25} & S'_{45} & S'_{55} & S'_{56} \\ S'_{16} & S'_{26} & S'_{46} & S'_{56} & S'_{66} \end{bmatrix}, \tag{5}$$

$$\mathbf{S}'^{*} = \begin{bmatrix} S'^{*}_{11} & S'^{*}_{12} & S'^{*}_{14} & S'^{*}_{15} & S'^{*}_{16} \\ S'^{*}_{12} & S'^{*}_{22} & S'^{*}_{24} & S'^{*}_{25} & S'^{*}_{26} \\ S'^{*}_{14} & S'^{*}_{24} & S'^{*}_{44} & S'^{*}_{45} & S'^{*}_{46} \\ S'^{*}_{15} & S'^{*}_{25} & S'^{*}_{45} & S'^{*}_{55} & S'^{*}_{56} \\ S'^{*}_{16} & S'^{*}_{26} & S'^{*}_{46} & S'^{*}_{56} & S'^{*}_{66} \end{bmatrix}, \tag{6}$$

$$\mathbf{t}^0 = \begin{bmatrix} t^0_1 & t^0_2 & t^0_3 \end{bmatrix}^T, \quad [\mathbf{u}] = [[u_1]\ [u_2]\ [u_3]]^T. \tag{7}$$

We add that $S'_{\alpha\beta} = S_{\alpha\beta} - S_{\alpha 3}S_{3\beta}/S_{33}$ in Eq. 5 are the reduced elastic compliances of the undamaged solid, and $S'^{*}_{\alpha\beta} = S^{*}_{\alpha\beta} - S^{*}_{\alpha 3}S^{*}_{3\beta}/S^{*}_{33}$ in Eq. 6 are the effective reduced elastic compliances of the cracked solid (Ting 1996).

The traction vector $\mathbf{t}^0$ is given by

$$\mathbf{t}^0 = \begin{bmatrix} \sigma^0_{12}\cos\theta - \sigma^0_{11}\sin\theta \\ \sigma^0_{22}\cos\theta - \sigma^0_{12}\sin\theta \\ \sigma^0_{23}\cos\theta - \sigma^0_{13}\sin\theta \end{bmatrix}. \tag{8}$$

If we ignore the crack interactions, i.e., $\eta \ll 1$, then the crack opening displacement vector $[\mathbf{u}] = [[u_1]\ [u_2]\ [u_3]]^T$ can be simply given by (Ting 1996)

$$[\mathbf{u}] = 2\sqrt{a^2 - x^2}\mathbf{L}^{-1}\mathbf{t}^0, \quad (|x| \le a) \tag{9}$$

where a is the half crack length, the 3×3 real and symmetric Barnett–Lothe tensor $\mathbf{L}$ for the undamaged solid is positive definite and $\mathbf{L}^{-1}$ is further written in the following form for the convenience of the following theoretical development

$$\mathbf{L}^{-1} = \begin{bmatrix} Y_{11} & Y_{12} & Y_{13} \\ Y_{12} & Y_{22} & Y_{23} \\ Y_{13} & Y_{23} & Y_{33} \end{bmatrix}. \tag{10}$$

We stress here that in writing Eq. 9 we have employed the property of the second-order tensor $\mathbf{L}$ under coordinate rotation (also see Fig. 114 on page 421 in Ting 1996).

Substituting Eqs. 2, 8 and 9 into Eq. 3, we can arrive at

$$\frac{1}{2}(\boldsymbol{\sigma}^0)^T\mathbf{S}'^{*}\boldsymbol{\sigma}^0 = \frac{1}{2}(\boldsymbol{\sigma}^0)^T\mathbf{S}'\boldsymbol{\sigma}^0 + \frac{\eta}{2a^2\theta_0} \left[\int_{-a}^{a}\sqrt{a^2 - x^2}\,\mathrm{d}x\right]\left[\int_{-\theta_0}^{\theta_0}(\mathbf{t}^0)^T\mathbf{L}^{-1}\mathbf{t}^0\,\mathrm{d}\theta\right], \tag{11}$$

where $\eta = Ma^2/A$ is the crack density parameter.

We can clearly observe from the above expression that $\mathbf{S}'^{*}$ is also positive definite due to the fact that the value of the second term on the right hand side of Eq. 11 is always positive (i.e., the elastic energy density is always *increased* through the introduction of the microcracks). The two integrals in Eq. 11 can be exactly carried out as

$$\int_{-a}^{a}\sqrt{a^2 - x^2}\,\mathrm{d}x = \frac{\pi a^2}{2}, \tag{12}$$

and

$$\begin{aligned} \int_{-\theta_0}^{\theta_0}(\mathbf{t}^0)^T\mathbf{L}^{-1}\mathbf{t}^0\,\mathrm{d}\theta = {} & \frac{Y_{11}}{2}[2\theta_0 - \sin(2\theta_0)](\sigma^0_{11})^2 \\ & + \frac{Y_{22}}{2}[2\theta_0 + \sin(2\theta_0)](\sigma^0_{22})^2 \\ & + \frac{Y_{33}}{2}[2\theta_0 + \sin(2\theta_0)](\sigma^0_{23})^2 \\ & + \frac{Y_{33}}{2}[2\theta_0 - \sin(2\theta_0)](\sigma^0_{13})^2 \\ & + \frac{1}{2}\{Y_{11}[2\theta_0 + \sin(2\theta_0)] \\ & + Y_{22}[2\theta_0 - \sin(2\theta_0)]\}(\sigma^0_{12})^2 \\ & + Y_{13}[2\theta_0 - \sin(2\theta_0)]\sigma^0_{11}\sigma^0_{13} \\ & + Y_{12}[2\theta_0 - \sin(2\theta_0)]\sigma^0_{11}\sigma^0_{12} \\ & + Y_{23}[2\theta_0 + \sin(2\theta_0)]\sigma^0_{22}\sigma^0_{23} \\ & + Y_{12}[2\theta_0 + \sin(2\theta_0)]\sigma^0_{22}\sigma^0_{12} \\ & + Y_{13}[2\theta_0 + \sin(2\theta_0)]\sigma^0_{23}\sigma^0_{12} \\ & + Y_{23}[2\theta_0 - \sin(2\theta_0)]\sigma^0_{13}\sigma^0_{12}. \end{aligned} \tag{13}$$

In view of the fact that the applied homogeneous stresses $\sigma^0_{11}, \sigma^0_{22}, \sigma^0_{23}, \sigma^0_{13}$ and σ^0_{12} can be *arbitrary*, then we obtain the following expressions for the effective reduced elastic compliances

$$\begin{aligned} S'^{*}_{11} &= S'_{11} + \frac{\pi\eta Y_{11}}{4\theta_0}[2\theta_0 - \sin(2\theta_0)], \\ S'^{*}_{22} &= S'_{22} + \frac{\pi\eta Y_{22}}{4\theta_0}[2\theta_0 + \sin(2\theta_0)], \\ S'^{*}_{44} &= S'_{44} + \frac{\pi\eta Y_{33}}{4\theta_0}[2\theta_0 + \sin(2\theta_0)], \\ S'^{*}_{55} &= S'_{55} + \frac{\pi\eta Y_{33}}{4\theta_0}[2\theta_0 - \sin(2\theta_0)], \\ S'^{*}_{66} &= S'_{66} + \frac{\pi\eta}{4\theta_0}\{Y_{11}[2\theta_0 + \sin(2\theta_0)] \\ &\quad + Y_{22}[2\theta_0 - \sin(2\theta_0)]\}, \end{aligned}$$

$$
\begin{aligned}
S'^{*}_{12} &= S'_{12},\\
S'^{*}_{14} &= S'_{14},\\
S'^{*}_{15} &= S'_{15} + \frac{\pi\eta Y_{13}}{4\theta_0}[2\theta_0 - \sin(2\theta_0)],\\
S'^{*}_{16} &= S'_{16} + \frac{\pi\eta Y_{12}}{4\theta_0}[2\theta_0 - \sin(2\theta_0)],\\
S'^{*}_{24} &= S'_{24} + \frac{\pi\eta Y_{23}}{4\theta_0}[2\theta_0 + \sin(2\theta_0)],\\
S'^{*}_{25} &= S'_{25},\\
S'^{*}_{26} &= S'_{26} + \frac{\pi\eta Y_{12}}{4\theta_0}[2\theta_0 + \sin(2\theta_0)],\\
S'^{*}_{45} &= S'_{45},\\
S'^{*}_{46} &= S'_{46} + \frac{\pi\eta Y_{13}}{4\theta_0}[2\theta_0 + \sin(2\theta_0)],\\
S'^{*}_{56} &= S'_{56} + \frac{\pi\eta Y_{23}}{4\theta_0}[2\theta_0 - \sin(2\theta_0)].
\end{aligned}
\tag{14}
$$

Equation 14 indicates that the four compliance components S'^{*}_{12}, S'^{*}_{14}, S'^{*}_{25} and S'^{*}_{45} are equal to the corresponding ones for the undamaged material and that $S'^{*}_{ii} \geq S'_{ii}$, $(i = 1, 2, 4, 5, 6)$ since $Y_{11}, Y_{22}, Y_{33} > 0$. It is of interest to notice that the present result of $S'^{*}_{12} = S'_{12}$ is consistent with the observation by Mauge and Kachanov (1994) that $\nu^{*}_{12}/E^{*}_{1} = \nu_{12}/E_1$ for an orthotropic solid containing perfectly aligned or randomly oriented cracks under plane stress deformation. The result we obtain is valid for generally anisotropic materials containing cracks with an arbitrary degree of alignment.

When the undamaged material is orthotropic, it follows from the above expression that

$$
\frac{1}{\mu^{*}_{12}} = \frac{1}{\mu_{12}} + \frac{\pi\eta}{4\theta_0} \times \left[\frac{2\theta_0 + \sin(2\theta_0)}{L_{11}} + \frac{2\theta_0 - \sin(2\theta_0)}{L_{22}}\right], \tag{15}
$$

which clearly demonstrates that the effective in-plane shear modulus μ^{*}_{12} depends on the degree of crack alignment characterized by θ_0 when $L_{11} \neq L_{22}$. Furthermore when the undamaged material is isotropic such that $L_{11} = L_{22} = \frac{\mu}{1-\nu}$, with μ and ν being the shear modulus and the Poisson's ratio, respectively, then Eq. 15 reduces to

$$
\mu^{*}_{12} = \frac{\mu}{1 + \pi\eta(1-\nu)}, \tag{16}
$$

which is the classical NIA result obtained by Bristow (1960), and is independent of the degree of crack alignment (Kachanov 1992). We illustrate in Fig. 2 the variation of μ^{*}_{12} as a function of θ_0 by using Eq. 15 for three different values of $L_{11}/L_{22} = 0.5, 1.0, 1.5$ with $\pi\eta\mu_{12}/L_{11} = 0.25$. We observe from Fig. 2 that μ^{*}_{12} is an increasing function of θ_0 when $L_{11} < L_{22}$; whereas it is a decreasing function of θ_0 when $L_{11} > L_{22}$.

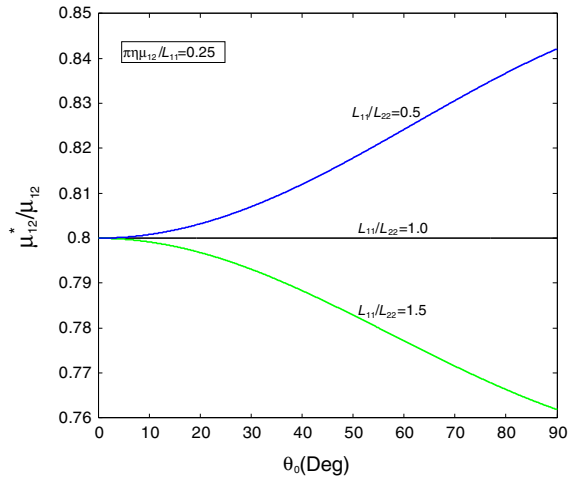

Fig. 2 The variations of μ^{*}_{12} of a cracked orthotropic elastic material as a function of θ_0 by using Eq. 15 for three different values of $L_{11}/L_{22} = 0.5, 1.0, 1.5$ with $\pi\eta\mu_{12}/L_{11} = 0.25$

In the following we discuss two typical cases for the crack orientations:

2.1 Perfectly aligned cracks

When the microcracks are perfectly aligned, we have $\theta_0 = 0$. Consequently it follows from Eq. 14 that

$$
\begin{aligned}
S'^{*}_{11} &= S'_{11},\\
S'^{*}_{22} &= S'_{22} + \pi\eta Y_{22},\\
S'^{*}_{44} &= S'_{44} + \pi\eta Y_{33},\\
S'^{*}_{55} &= S'_{55},\\
S'^{*}_{66} &= S'_{66} + \pi\eta Y_{11},\\
S'^{*}_{12} &= S'_{12},\\
S'^{*}_{14} &= S'_{14},\\
S'^{*}_{15} &= S'_{15},\\
S'^{*}_{16} &= S'_{16},\\
S'^{*}_{24} &= S'_{24} + \pi\eta Y_{23},\\
S'^{*}_{25} &= S'_{25},\\
S'^{*}_{26} &= S'_{26} + \pi\eta Y_{12},
\end{aligned}
$$

$$
\begin{aligned}
S'^{*}_{45} &= S'_{45},\\
S'^{*}_{46} &= S'_{46} + \pi\eta Y_{13},\\
S'^{*}_{56} &= S'_{56}.
\end{aligned}
\tag{17}
$$

In addition, if the undamaged material is orthotropic, Eq. 17 further reduces to Eq. 27 derived by Mauge and Kachanov (1994) in view of the fact that Y_{11} and Y_{22} for orthotropic materials are explicitly given by (Suo 1990)

$$
\begin{aligned}
Y_{11} &= \sqrt{S'_{11}}\left[2\sqrt{S'_{11}S'_{22}} + 2S'_{12} + S'_{66}\right]^{\frac{1}{2}},\\
Y_{22} &= \sqrt{S'_{22}}\left[2\sqrt{S'_{11}S'_{22}} + 2S'_{12} + S'_{66}\right]^{\frac{1}{2}}.
\end{aligned}
\tag{18}
$$

Here it should be noticed that Mauge and Kachanov (1994) discussed the plane stress problem.

2.2 Randomly oriented cracks

When the microcracks are oriented randomly, we have $\theta_0 = \pi/2$. Consequently it follows from Eq. 14 that

$$
\begin{aligned}
S'^{*}_{11} &= S'_{11} + \frac{1}{2}\pi\eta Y_{11},\\
S'^{*}_{22} &= S'_{22} + \frac{1}{2}\pi\eta Y_{22},\\
S'^{*}_{44} &= S'_{44} + \frac{1}{2}\pi\eta Y_{33},\\
S'^{*}_{55} &= S'_{55} + \frac{1}{2}\pi\eta Y_{33},\\
S'^{*}_{66} &= S'_{66} + \frac{1}{2}\pi\eta (Y_{11} + Y_{22}),\\
S'^{*}_{12} &= S'_{12},\\
S'^{*}_{14} &= S'_{14},\\
S'^{*}_{15} &= S'_{15} + \frac{1}{2}\pi\eta Y_{13},\\
S'^{*}_{16} &= S'_{16} + \frac{1}{2}\pi\eta Y_{12},\\
S'^{*}_{24} &= S'_{24} + \frac{1}{2}\pi\eta Y_{23},\\
S'^{*}_{25} &= S'_{25},\\
S'^{*}_{26} &= S'_{26} + \frac{1}{2}\pi\eta Y_{12},\\
S'^{*}_{45} &= S'_{45},\\
S'^{*}_{46} &= S'_{46} + \frac{1}{2}\pi\eta Y_{13},\\
S'^{*}_{56} &= S'_{56} + \frac{1}{2}\pi\eta Y_{23}.
\end{aligned}
\tag{19}
$$

In addition if the undamaged material is orthotropic, Eq. 19 reduces to Eq. 32 derived by Mauge and Kachanov (1994). It seems that the factor '$\pi/4$' appearing in the third expression of Eq. 32 in Mauge and Kachanov (1994) should read '$\pi/2$'. Furthermore it follows from Eq. 19 that the overall effective elastic properties will be transversely isotropic for an originally isotropic material containing randomly oriented cracks ($\theta_0 = \pi/2$).

Once the effective reduced elastic compliances have been obtained, the effective stiffnesses can be conveniently obtained as

$$
\mathbf{C}^{0*} = (\mathbf{S}'^{*})^{-1},
\tag{20}
$$

where

$$
\mathbf{C}^{0*} = \begin{bmatrix}
C^*_{11} & C^*_{12} & C^*_{14} & C^*_{15} & C^*_{16}\\
C^*_{12} & C^*_{22} & C^*_{24} & C^*_{25} & C^*_{26}\\
C^*_{14} & C^*_{24} & C^*_{44} & C^*_{45} & C^*_{46}\\
C^*_{15} & C^*_{25} & C^*_{45} & C^*_{55} & C^*_{56}\\
C^*_{16} & C^*_{26} & C^*_{46} & C^*_{56} & C^*_{66}
\end{bmatrix}.
\tag{21}
$$

3 Extension to piezoelectric solids

In the previous section we have derived the effective reduced elastic compliances of a purely elastic solid containing microcracks. In fact, the energy method can also be conveniently adopted to derive the effective electroelastic properties of a piezoelectric solid containing insulating, permeable or conducting microcracks.

3.1 A piezoelectric solid containing insulating microcracks

In this case, the energy balance relationship for two-dimensional problems, in which the displacements u_i and the electric potential ϕ depend on x_1 and x_2 only, can be expressed in the following form when the piezoelectric solid containing insulating microcracks is subjected to the homogeneous stresses σ^0_{ij} and the homogeneous electric displacements D^0_i (Suo et al. 1992)

$$
\begin{aligned}
\frac{1}{2}(\tilde{\boldsymbol{\sigma}}^0)^T(\tilde{\mathbf{C}}^{0*})^{-1}\tilde{\boldsymbol{\sigma}}^0 &= \frac{1}{2}(\tilde{\boldsymbol{\sigma}}^0)^T(\tilde{\mathbf{C}}^0)^{-1}\tilde{\boldsymbol{\sigma}}^0\\
&\quad + \frac{M}{2A}\int_{-\theta_0}^{\theta_0}\phi(\theta)\int_{C_k}(\tilde{\mathbf{t}}^0)^T[\tilde{\mathbf{u}}]\mathrm{d}C_k\mathrm{d}\theta,
\end{aligned}
\tag{22}
$$

where

$$\tilde{\boldsymbol{\sigma}}^0 = [\sigma_{11}^0 \quad \sigma_{22}^0 \quad \sigma_{23}^0 \quad \sigma_{13}^0 \quad \sigma_{12}^0 \quad D_1^0 \quad D_2^0]^T, \tag{23}$$

$$[\tilde{\mathbf{u}}] = [[u_1] \quad [u_2] \quad [u_3] \quad [\varphi]]^T, \tag{24}$$

$$\tilde{\mathbf{C}}^0 = \begin{bmatrix} C_{11} & C_{12} & C_{14} & C_{15} & C_{16} & e_{11} & e_{21} \\ C_{12} & C_{22} & C_{24} & C_{25} & C_{26} & e_{12} & e_{22} \\ C_{14} & C_{24} & C_{44} & C_{45} & C_{46} & e_{14} & e_{24} \\ C_{15} & C_{25} & C_{45} & C_{55} & C_{56} & e_{15} & e_{25} \\ C_{16} & C_{26} & C_{46} & C_{56} & C_{66} & e_{16} & e_{26} \\ e_{11} & e_{12} & e_{14} & e_{15} & e_{16} & -\epsilon_{11} & -\epsilon_{12} \\ e_{21} & e_{22} & e_{24} & e_{25} & e_{26} & -\epsilon_{12} & -\epsilon_{22} \end{bmatrix}, \tag{25}$$

$$\tilde{\mathbf{C}}^{0*} = \begin{bmatrix} C_{11}^* & C_{12}^* & C_{14}^* & C_{15}^* & C_{16}^* & e_{11}^* & e_{21}^* \\ C_{12}^* & C_{22}^* & C_{24}^* & C_{25}^* & C_{26}^* & e_{12}^* & e_{22}^* \\ C_{14}^* & C_{24}^* & C_{44}^* & C_{45}^* & C_{46}^* & e_{14}^* & e_{24}^* \\ C_{15}^* & C_{25}^* & C_{45}^* & C_{55}^* & C_{56}^* & e_{15}^* & e_{25}^* \\ C_{16}^* & C_{26}^* & C_{46}^* & C_{56}^* & C_{66}^* & e_{16}^* & e_{26}^* \\ e_{11}^* & e_{12}^* & e_{14}^* & e_{15}^* & e_{16}^* & -\epsilon_{11}^* & -\epsilon_{12}^* \\ e_{21}^* & e_{22}^* & e_{24}^* & e_{25}^* & e_{26}^* & -\epsilon_{12}^* & -\epsilon_{22}^* \end{bmatrix}, \tag{26}$$

$$\tilde{\mathbf{t}}^0 = \begin{bmatrix} \sigma_{12}^0 \cos\theta - \sigma_{11}^0 \sin\theta \\ \sigma_{22}^0 \cos\theta - \sigma_{12}^0 \sin\theta \\ \sigma_{23}^0 \cos\theta - \sigma_{13}^0 \sin\theta \\ D_2^0 \cos\theta - D_1^0 \sin\theta \end{bmatrix}. \tag{27}$$

In Eqs. 25 and 26, C_{ij}, e_{ij} and ϵ_{ij} are the elastic, piezoelectric and dielectric constants of the undamaged solid, while C_{ij}^*, e_{ij}^* and ϵ_{ij}^* are the corresponding (unknown) constants for the damaged solid. The energy expression in Eq. 22 is in fact the electric enthalpy (Suo et al. 1992). When ignoring crack interactions and assuming that the crack surfaces are traction-free and charge-free (Pak 1990; Suo et al. 1992), the jump in displacement and electric potential across the crack surface can be simply given by

$$[\tilde{\mathbf{u}}] = 2\sqrt{a^2 - x^2}\tilde{\mathbf{L}}^{-1}\tilde{\mathbf{t}}^0, \quad (|x| \le a) \tag{28}$$

where $\tilde{\mathbf{L}}$ is the 4×4 real and symmetric Barnett–Lothe tensor for the undamaged piezoelectric solid (Ting 1996). We add that $\tilde{\mathbf{L}}$ is not positive definite and can be further expressed as

$$\tilde{\mathbf{L}} = \begin{bmatrix} \mathbf{L}_{11} & \mathbf{L}_{14} \\ \mathbf{L}_{14}^T & -L_{44} \end{bmatrix}, \tag{29}$$

where the 3×3 symmetric matrix $\mathbf{L}_{11}$ is positive definite and $L_{44} > 0$.

Substituting the above results into Eq. 22, we finally arrive at a concise expression for the effective electroelastic properties of the microcracked piezoelectric solid

$$(\tilde{\mathbf{C}}^{0*})^{-1} = (\tilde{\mathbf{C}}^0)^{-1} + \frac{\pi\eta[2\theta_0 - \sin(2\theta_0)]}{4\theta_0}\tilde{\mathbf{J}}_1^T\tilde{\mathbf{L}}^{-1}\tilde{\mathbf{J}}_1 + \frac{\pi\eta[2\theta_0 + \sin(2\theta_0)]}{4\theta_0}\tilde{\mathbf{J}}_2^T\tilde{\mathbf{L}}^{-1}\tilde{\mathbf{J}}_2, \tag{30}$$

where

$$\tilde{\mathbf{J}}_1 = \begin{bmatrix} 1 & 0 & 0 & 0 & 0 & 0 & 0 \\ 0 & 0 & 0 & 0 & 1 & 0 & 0 \\ 0 & 0 & 0 & 1 & 0 & 0 & 0 \\ 0 & 0 & 0 & 0 & 0 & 1 & 0 \end{bmatrix}, \quad \tilde{\mathbf{J}}_2 = \begin{bmatrix} 0 & 0 & 0 & 0 & 1 & 0 & 0 \\ 0 & 1 & 0 & 0 & 0 & 0 & 0 \\ 0 & 0 & 1 & 0 & 0 & 0 & 0 \\ 0 & 0 & 0 & 0 & 0 & 0 & 1 \end{bmatrix}. \tag{31}$$

It can be easily verified from Eqs. 29 and 30 that both $\mathbf{C}^{0*}$ defined by Eq. 21 and $\begin{bmatrix} \epsilon_{11}^* & \epsilon_{12}^* \\ \epsilon_{12}^* & \epsilon_{22}^* \end{bmatrix}$ are positive definite. It can also be observed from Eq. 30 that the eighteen components (12) = (21), (13) = (31), (24) = (42), (34) = (43), (26) = (62), (36) = (63), (17) = (71), (47) = (74) and (67) = (76) of $(\tilde{\mathbf{C}}^{0*})^{-1}$ do not change due to the introduction of the insulating microcracks within the framework of NIA.

For a hexagonal piezoelectric solid with its poling direction along the x_3-axis, it follows from Eq. 30 that the effective electroelastic properties of the microcracked, piezoelectric solid pertaining to the antiplane deformation and in-plane electric fields can be explicitly given by

$$\begin{aligned} \frac{C_{55}^*}{C_{44}} &= \frac{e_{15}^*}{e_{15}} = \frac{\epsilon_{11}^*}{\epsilon_{11}} = \frac{1}{1 + \frac{\pi\eta[2\theta_0 - \sin(2\theta_0)]}{4\theta_0}}, \\ \frac{C_{44}^*}{C_{44}} &= \frac{e_{24}^*}{e_{15}} = \frac{\epsilon_{22}^*}{\epsilon_{11}} = \frac{1}{1 + \frac{\pi\eta[2\theta_0 + \sin(2\theta_0)]}{4\theta_0}}, \\ C_{45}^* &= e_{14}^* = e_{25}^* = \epsilon_{12}^* = 0. \end{aligned} \tag{32}$$

For a hexagonal piezoelectric solid with its poling direction along the x_2-axis, it follows from Eq. 30 that the effective electroelastic properties of the microcracked, piezoelectric solid pertaining to the in-plane deformation and in-plane electric fields can be explicitly given by

$$\begin{bmatrix} C_{11}^* & C_{12}^* & e_{21}^* \\ C_{12}^* & C_{22}^* & e_{22}^* \\ e_{21}^* & e_{22}^* & -\epsilon_{22}^* \end{bmatrix}^{-1} = \begin{bmatrix} C_{11} & C_{12} & e_{21} \\ C_{12} & C_{22} & e_{22} \\ e_{21} & e_{22} & -\epsilon_{22} \end{bmatrix}^{-1}$$

$$+\frac{\pi\eta\,[2\theta_0-\sin(2\theta_0)]}{4\theta_0}\begin{bmatrix}\frac{1}{C_L}&0&0\\0&0&0\\0&0&0\end{bmatrix}$$

$$+\frac{\pi\eta\,[2\theta_0+\sin(2\theta_0)]}{4\theta_0}\begin{bmatrix}0&0&0\\0&\frac{1}{C_T}&\frac{1}{e}\\0&\frac{1}{e}&-\frac{1}{\epsilon}\end{bmatrix},$$

$$\begin{bmatrix}C^*_{66}&e^*_{16}\\e^*_{16}&-\epsilon^*_{11}\end{bmatrix}^{-1}=\begin{bmatrix}C_{66}&e_{16}\\e_{16}&-\epsilon_{11}\end{bmatrix}^{-1}$$

$$+\frac{\pi\eta\,[2\theta_0-\sin(2\theta_0)]}{4\theta_0}\begin{bmatrix}\frac{1}{C_T}&\frac{1}{e}\\\frac{1}{e}&-\frac{1}{\epsilon}\end{bmatrix}$$

$$+\frac{\pi\eta\,[2\theta_0+\sin(2\theta_0)]}{4\theta_0}\begin{bmatrix}\frac{1}{C_L}&0\\0&0\end{bmatrix},$$

$$C^*_{16}=C^*_{26}=e^*_{11}=e^*_{12}=e^*_{26}=\epsilon^*_{12}=0, \tag{33}$$

where

$$\mathrm{Re}\,\{\mathbf{Y}\}=\begin{bmatrix}\frac{1}{C_L}&0&0\\0&\frac{1}{C_T}&\frac{1}{e}\\0&\frac{1}{e}&-\frac{1}{\epsilon}\end{bmatrix}, \tag{34}$$

has been defined in Eq. C12 by Suo et al. (1992). The elements in Eq. 34 have to be determined numerically for the specific piezoelectric material. We illustrate in Figs. 3, 4, 5 the variations of the effective electroelastic moduli as functions of θ_0 with $\eta = 0.2$ for a micro-cracked piezoelectric material $BaTiO_3$ with its material properties given by (Pan 2001)

$$C_{11}=C_{33}=166\times10^9\,\mathrm{N/m^2},$$
$$C_{13}=77\times10^9\,\mathrm{N/m^2},$$
$$C_{12}=C_{23}=78\times10^9\,\mathrm{N/m^2},$$
$$C_{22}=162\times10^9\,\mathrm{N/m^2},$$
$$C_{44}=C_{66}=43\times10^9\,\mathrm{N/m^2},$$
$$C_{55}=44.5\times10^9\,\mathrm{N/m^2},$$
$$e_{21}=e_{23}=-4.4\,\mathrm{C/m^2},$$
$$e_{22}=18.6\,\mathrm{C/m^2},$$
$$e_{34}=e_{16}=11.6\,\mathrm{C/m^2},$$
$$\epsilon_{11}=\epsilon_{33}=11.2\times10^{-9}\,\mathrm{C^2/(Nm^2)},$$
$$\epsilon_{22}=12.6\times10^{-9}\,\mathrm{C^2/(Nm^2)}.$$

It can be observed from the three figures that the degree of the crack alignment characterized by θ_0 has a significant influence on most of the effective electroelastic moduli except C^*_{66} due to the fact that the ratio $C_T/C_L = 1.0736$ for $BaTiO_3$ is very close to unity. We also observe that all the effective electroelastic moduli are monotonically increasing or decreasing

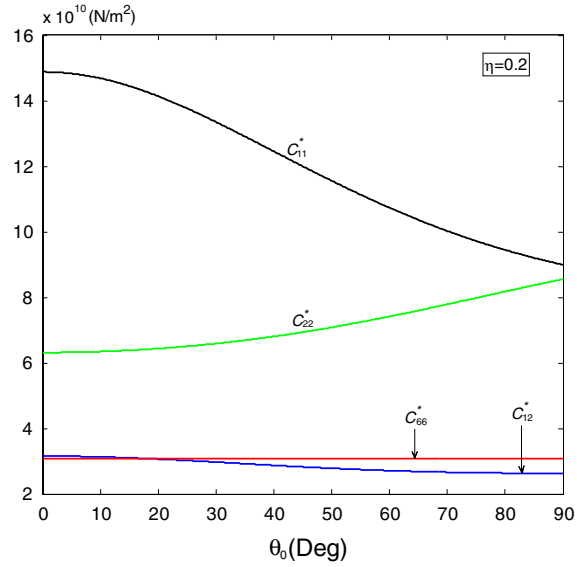

Fig. 3 The variations of the four effective elastic constants $C^*_{11}, C^*_{22}, C^*_{12}$ and C^*_{66} as functions of θ_0 with $\eta = 0.2$ for a piezoelectric material $BaTiO_3$ containing two-dimensional insulating microcracks. The poling direction of the piezoelectric solid is along the x_2-axis

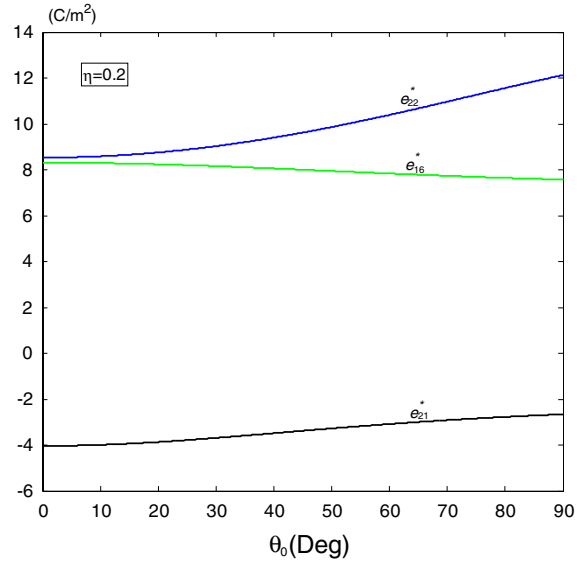

Fig. 4 The variations of the three effective piezoelectric constants e^*_{22}, e^*_{21} and e^*_{16} as functions of θ_0 with $\eta = 0.2$ for a piezoelectric material $BaTiO_3$ containing two-dimensional insulating microcracks. The poling direction of the piezoelectric solid is along the x_2-axis

functions of θ_0 at a fixed crack density η. It can be clearly seen from Fig. 3 that the effective elastic anisotropy decreases as θ_0 increases from zero for perfectly

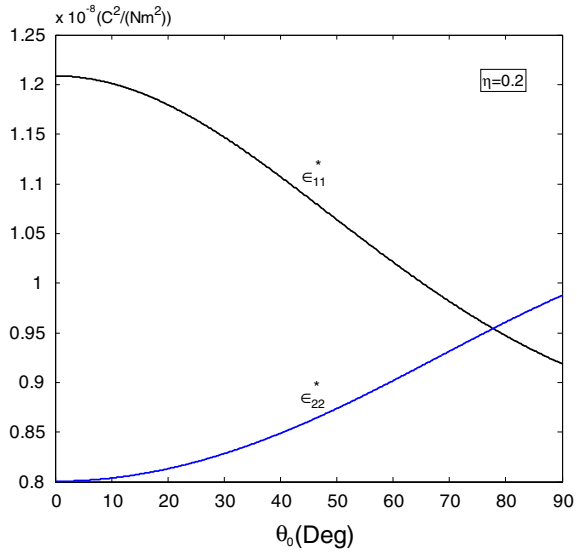

Fig. 5 The variations of the two effective dielectric constants ϵ_{11}^* and ϵ_{22}^* as functions of θ_0 with $\eta = 0.2$ for a piezoelectric material $BaTiO_3$ containing two-dimensional insulating microcracks. The poling direction of the piezoelectric solid is along the x_2-axis

aligned microcracks to 90° for randomly oriented microcracks. When $\theta_0 = 90°$, $C_{11}^* \approx C_{22}^*$ and $C_{66}^* \approx \frac{1}{2}\left(C_{11}^* - C_{12}^*\right)$. We observe from Fig. 5 that $\epsilon_{11}^* > \epsilon_{11}$ when $\theta_0 < 40°$. This observation indicates that the piezoelectric effect plays an important role in the effective dielectric properties of a microcracked piezoelectric solid. On the other hand our results show that some of the effective piezoelectric and dielectric moduli at a certain fixed θ_0 can be rather complex functions of η. This complex phenomenon is demonstrated in Figs. 6 and 7 for e_{21}^* and ϵ_{11}^* as functions of η for four different values of $\theta_0 = 0, \pi/8, \pi/4, \pi/2$. We can see from Fig. 6 that when θ_0 is below a certain value (the detailed results show that this value is $\theta_0 = \pi/3.03$), e_{21}^* can attain its minimum value at an extremely low crack density η (for example when $\theta_0 = \pi/8$, e_{21}^* attains its minimum value of $-4.5851\,\mathrm{C/m^2}$ at $\eta = 0.04$); on the other hand when $\pi/3.03 < \theta_0 \leq \pi/2$, e_{21}^* is a monotonically increasing function of η. Our detailed results also show that depending on the value of θ_0, there exist three possible distributions of ϵ_{11}^*: (i) a monotonically increasing function of η when $\theta_0 = 0$; (ii) a function with its maximum value at a certain value of η when $0 < \theta_0 \leq \pi/4.09$ (for example as shown in Fig. 7 when $\theta_0 = \pi/8$, ϵ_{11}^* attains its maximum value of $11.86 \times 10^{-9}\,\mathrm{C^2/(Nm^2)}$ at $\eta = 0.436$); (iii) a monotonically decreasing function of η when $\theta_0 > \pi/4.09$. We add

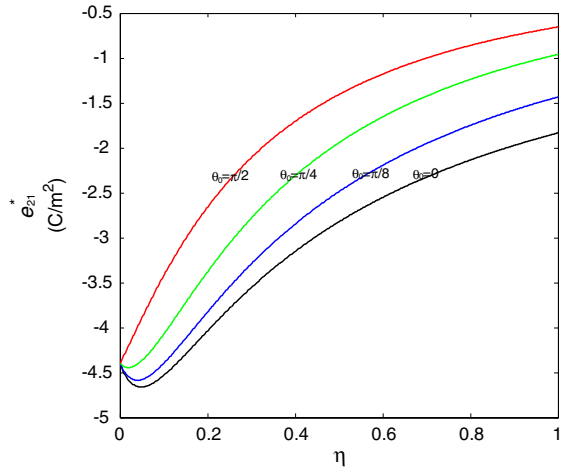

Fig. 6 The variations of e_{21}^* as a function of η at four different values of $\theta_0 = 0, \pi/8, \pi/4, \pi/2$ for a piezoelectric material $BaTiO_3$ containing two-dimensional insulating microcracks. The poling direction of the piezoelectric solid is along the x_2-axis

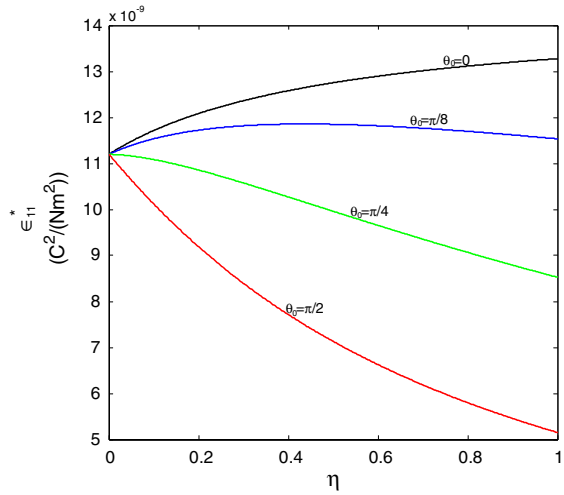

Fig. 7 The variations of ϵ_{11}^* as a function of η at four different values of $\theta_0 = 0, \pi/8, \pi/4, \pi/2$ for a piezoelectric material $BaTiO_3$ containing two-dimensional insulating microcracks. The poling direction of the piezoelectric solid is along the x_2-axis

that this unexpected phenomenon is caused by the coupling effect between the mechanical field and the electric field (or the piezoelectric effect). For example when there exists no piezoelectric effect, $\epsilon_{11}^* \equiv \epsilon_{11}$ for perfectly aligned microcracks ($\theta_0 = 0$).

3.2 A piezoelectric solid containing permeable microcracks

The effective electroelastic properties of a piezoelectric solid containing permeable microcracks (i.e., $\varphi^+ =$

φ^-, $D_n^+ = D_n^-$ across the crack surface, see Suo et al. 1992) can be simply derived as

$$(\tilde{\mathbf{C}}^{0*})^{-1} = (\tilde{\mathbf{C}}^{0})^{-1} + \frac{\pi\eta\,[2\theta_0 - \sin(2\theta_0)]}{4\theta_0}\mathbf{J}_3^T\mathbf{L}_{11}^{-1}\mathbf{J}_3 + \frac{\pi\eta\,[2\theta_0 + \sin(2\theta_0)]}{4\theta_0}\mathbf{J}_4^T\mathbf{L}_{11}^{-1}\mathbf{J}_4, \tag{35}$$

where the 3×3 symmetric matrix $\mathbf{L}_{11}$ has been defined in Eq. 29 and

$$\mathbf{J}_3 = \begin{bmatrix} 1 & 0 & 0 & 0 & 0 & 0 & 0 \\ 0 & 0 & 0 & 0 & 1 & 0 & 0 \\ 0 & 0 & 0 & 1 & 0 & 0 & 0 \end{bmatrix},$$

$$\mathbf{J}_4 = \begin{bmatrix} 0 & 0 & 0 & 0 & 1 & 0 & 0 \\ 0 & 1 & 0 & 0 & 0 & 0 & 0 \\ 0 & 0 & 1 & 0 & 0 & 0 & 0 \end{bmatrix}. \tag{36}$$

We see from Eq. 35 that the thirty-two components (12)=(21), (13)=(31), (24)=(42), (34)=(43), (ij)=(ji), (i=1-7, j=6,7) of $(\tilde{\mathbf{C}}^{0*})^{-1}$ do not change due to the introduction of the permeable microcracks within the framework of NIA. For a hexagonal piezoelectric solid with its poling direction along the x_3-axis, it follows from Eq. 35 that the effective electroelastic properties of the microcracked, piezoelectric solid pertaining to the antiplane deformation and in-plane electric fields can be explicitly given by

$$\frac{C_{55}^*}{C_{44}} = \frac{e_{15}^*}{e_{15}} = \frac{1}{1 + \frac{\pi\eta[2\theta_0 - \sin(2\theta_0)]}{4\theta_0}},$$
$$\frac{\epsilon_{11}^*}{\epsilon_{11}} = 1 + \frac{\pi k_1\eta\,[2\theta_0 - \sin(2\theta_0)]}{4\theta_0 + \pi\eta\,[2\theta_0 - \sin(2\theta_0)]} \geq 1,$$
$$\frac{C_{44}^*}{C_{44}} = \frac{e_{24}^*}{e_{15}} = \frac{1}{1 + \frac{\pi\eta[2\theta_0 + \sin(2\theta_0)]}{4\theta_0}},$$
$$\frac{\epsilon_{22}^*}{\epsilon_{11}} = 1 + \frac{\pi k_1\eta\,[2\theta_0 + \sin(2\theta_0)]}{4\theta_0 + \pi\eta\,[2\theta_0 + \sin(2\theta_0)]} \geq 1,$$
$$C_{45}^* = e_{14}^* = e_{25}^* = \epsilon_{12}^* = 0, \tag{37}$$

where $k_1 = e_{15}^2/(\epsilon_{11}C_{44}) < 1$ is the electromechanical coupling factor.

We observe from the above expression that only the expressions for ϵ_{11}^* and ϵ_{22}^* are different from the corresponding ones in Eq. 32 for insulating microcracks. When θ_0 is fixed, ϵ_{11}^* and ϵ_{22}^* for permeable microcracks are increasing functions of η; whereas those for insulating microcracks are decreasing functions of η.

Similarly, for a hexagonal piezoelectric solid with its poling direction along the x_2-axis, it follows from Eq. 35 that the effective electroelastic properties of the microcracked piezoelectric solid pertaining to the in-plane deformation and in-plane electric fields can be explicitly given by

$$\begin{bmatrix} C_{11}^* & C_{12}^* & e_{21}^* \\ C_{12}^* & C_{22}^* & e_{22}^* \\ e_{21}^* & e_{22}^* & -\epsilon_{22}^* \end{bmatrix}^{-1} = \begin{bmatrix} C_{11} & C_{12} & e_{21} \\ C_{12} & C_{22} & e_{22} \\ e_{21} & e_{22} & -\epsilon_{22} \end{bmatrix}^{-1} + \frac{\pi\eta}{4\theta_0}\begin{bmatrix} \frac{2\theta_0 - \sin(2\theta_0)}{C_L} & 0 & 0 \\ 0 & \frac{(1+k_2)[2\theta_0 + \sin(2\theta_0)]}{k_2 C_T} & 0 \\ 0 & 0 & 0 \end{bmatrix},$$
$$\begin{bmatrix} C_{66}^* & e_{16}^* \\ e_{16}^* & -\epsilon_{11}^* \end{bmatrix}^{-1} = \begin{bmatrix} C_{66} & e_{16} \\ e_{16} & -\epsilon_{11} \end{bmatrix}^{-1} + \frac{\pi\eta}{4\theta_0}\left[\frac{(1+k_2)\,[2\theta_0 - \sin(2\theta_0)]}{k_2 C_T} + \frac{2\theta_0 + \sin(2\theta_0)}{C_L}\right]\begin{bmatrix} 1 & 0 \\ 0 & 0 \end{bmatrix},$$
$$C_{16}^* = C_{26}^* = e_{11}^* = e_{12}^* = e_{26}^* = \epsilon_{12}^* = 0, \tag{38}$$

where $k_2 = e^2/(\epsilon C_T)$.

3.3 A piezoelectric solid containing conducting microcracks

The effective electroelastic properties of a piezoelectric solid containing conducting microcracks (McMeeking 1987; Suo 1993) can also be similarly derived. The energy balance relationship for two-dimensional problems can be expressed in the following form when the piezoelectric solid containing conducting microcracks is subjected to the homogeneous stresses σ_{ij}^0 and the homogeneous electric fields E_i^0 (Suo 1993)

$$\frac{1}{2}(\hat{\boldsymbol{\sigma}}^0)^T(\hat{\mathbf{C}}^{0*})^{-1}\hat{\boldsymbol{\sigma}}^0 = \frac{1}{2}(\hat{\boldsymbol{\sigma}}^0)^T(\hat{\mathbf{C}}^{0})^{-1}\hat{\boldsymbol{\sigma}}^0 + \frac{M}{2A}\int_{-\theta_0}^{\theta_0}\phi(\theta)\int_{C_k}(\hat{\mathbf{t}}^0)^T[\hat{\mathbf{u}}]\mathrm{d}C_k\mathrm{d}\theta, \tag{39}$$

where

$$\hat{\boldsymbol{\sigma}}^0 = \begin{bmatrix} \sigma_{11}^0 & \sigma_{22}^0 & \sigma_{23}^0 & \sigma_{13}^0 & \sigma_{12}^0 & E_1^0 & E_2^0 \end{bmatrix}^T, \tag{40}$$

$$[\hat{\mathbf{u}}] = [[u_1] \quad [u_2] \quad [u_3] \quad [\xi]]^T, \tag{41}$$

$$\hat{\mathbf{C}}^0 = \begin{bmatrix} C_{11} & C_{12} & C_{14} & C_{15} & C_{16} & h_{11} & h_{21} \\ C_{12} & C_{22} & C_{24} & C_{25} & C_{26} & h_{12} & h_{22} \\ C_{14} & C_{24} & C_{44} & C_{45} & C_{46} & h_{14} & h_{24} \\ C_{15} & C_{25} & C_{45} & C_{55} & C_{56} & h_{15} & h_{25} \\ C_{16} & C_{26} & C_{46} & C_{56} & C_{66} & h_{16} & h_{26} \\ h_{11} & h_{12} & h_{14} & h_{15} & h_{16} & \beta_{11} & \beta_{12} \\ h_{21} & h_{22} & h_{24} & h_{25} & h_{26} & \beta_{12} & \beta_{22} \end{bmatrix}, \quad (42)$$

$$\hat{\mathbf{C}}^{0*} = \begin{bmatrix} C_{11}^* & C_{12}^* & C_{14}^* & C_{15}^* & C_{16}^* & h_{11}^* & h_{21}^* \\ C_{12}^* & C_{22}^* & C_{24}^* & C_{25}^* & C_{26}^* & h_{12}^* & h_{22}^* \\ C_{14}^* & C_{24}^* & C_{44}^* & C_{45}^* & C_{46}^* & h_{14}^* & h_{24}^* \\ C_{15}^* & C_{25}^* & C_{45}^* & C_{55}^* & C_{56}^* & h_{15}^* & h_{25}^* \\ C_{16}^* & C_{26}^* & C_{46}^* & C_{56}^* & C_{66}^* & h_{16}^* & h_{26}^* \\ h_{11}^* & h_{12}^* & h_{14}^* & h_{15}^* & h_{16}^* & \beta_{11}^* & \beta_{12}^* \\ h_{21}^* & h_{22}^* & h_{24}^* & h_{25}^* & h_{26}^* & \beta_{12}^* & \beta_{22}^* \end{bmatrix}, \quad (43)$$

$$\hat{\mathbf{t}}^0 = \begin{bmatrix} \sigma_{12}^0 \cos\theta - \sigma_{11}^0 \sin\theta \\ \sigma_{22}^0 \cos\theta - \sigma_{12}^0 \sin\theta \\ \sigma_{23}^0 \cos\theta - \sigma_{13}^0 \sin\theta \\ E_1^0 \cos\theta + E_2^0 \sin\theta \end{bmatrix}. \quad (44)$$

In Eq. 41, ξ is defined such that $D_1 = \xi_{,2}, D_2 = -\xi_{,1}$. In Eqs. 42 and 43, C_{ij}, h_{ij} and β_{ij} are the elastic, piezoelectric and dielectric constants of the undamaged solid, while C_{ij}^*, h_{ij}^* and β_{ij}^* are the corresponding (unknown) constants for the damaged solid. Here we have adopted the material constant notations in Suo (1993). When ignoring crack interactions, the jump in displacement and ξ across the crack surfaces can be simply given by (Suo 1993)

$$[\hat{\mathbf{u}}] = 2\sqrt{a^2 - x^2}\hat{\mathbf{L}}^{-1}\hat{\mathbf{t}}^0, \quad (|x| \le a) \quad (45)$$

where $\hat{\mathbf{L}}$ is a 4×4 real and symmetric, positive definite matrix.

Substituting the above results into Eq. 22, we finally arrive at a concise expression for the effective electroelastic properties of the microcracked piezoelectric solid

$$(\hat{\mathbf{C}}^{0*})^{-1} = (\hat{\mathbf{C}}^0)^{-1} + \frac{\pi\eta[2\theta_0 - \sin(2\theta_0)]}{4\theta_0}\hat{\mathbf{J}}_1^T\hat{\mathbf{L}}^{-1}\hat{\mathbf{J}}_1 + \frac{\pi\eta[2\theta_0 + \sin(2\theta_0)]}{4\theta_0}\hat{\mathbf{J}}_2^T\hat{\mathbf{L}}^{-1}\hat{\mathbf{J}}_2, \quad (46)$$

where

$$\hat{\mathbf{J}}_1 = \begin{bmatrix} 1 & 0 & 0 & 0 & 0 & 0 & 0 \\ 0 & 0 & 0 & 0 & 1 & 0 & 0 \\ 0 & 0 & 0 & 1 & 0 & 0 & 0 \\ 0 & 0 & 0 & 0 & 0 & 0 & -1 \end{bmatrix},$$

$$\hat{\mathbf{J}}_2 = \begin{bmatrix} 0 & 0 & 0 & 0 & 1 & 0 & 0 \\ 0 & 1 & 0 & 0 & 0 & 0 & 0 \\ 0 & 0 & 1 & 0 & 0 & 0 & 0 \\ 0 & 0 & 0 & 0 & 0 & 1 & 0 \end{bmatrix}. \quad (47)$$

It is apparent that the energy density function always *increases* through the introduction of conducting microcracks, and that $\hat{\mathbf{C}}^{0*}$ is positive definite in view of the fact that both $\hat{\mathbf{C}}^0$ and $\hat{\mathbf{L}}$ are positive definite. Interestingly, this result is very similar to the situation when the matrix is purely elastic. We stress that the convex energy density function used here for conducting cracks is different than the non-convex electric enthalpy used for insulating cracks.

For a hexagonal piezoelectric solid with its poling direction along the x_3-axis, it follows from Eq. 46 that the effective electroelastic properties of the microcracked piezoelectric solid pertaining to the antiplane deformation and in-plane electric fields can be explicitly given by

$$\frac{C_{55}^*}{C_{44}\left[1 + \frac{\pi\eta[2\theta_0 - \sin(2\theta_0)]}{4\theta_0}\right]} = \frac{\beta_{11}^*}{\beta_{11}\left[1 + \frac{\pi\eta[2\theta_0 - \sin(2\theta_0)]}{4\theta_0}\right]} = \frac{h_{15}^*}{h_{15}} = \frac{C_{44}\beta_{11} - h_{15}^2}{C_{44}\beta_{11}\left[1 + \frac{\pi\eta[2\theta_0 - \sin(2\theta_0)]}{4\theta_0}\right]^2 - h_{15}^2},$$

$$\frac{C_{44}^*}{C_{44}\left[1 + \frac{\pi\eta[2\theta_0 + \sin(2\theta_0)]}{4\theta_0}\right]} = \frac{\beta_{22}^*}{\beta_{11}\left[1 + \frac{\pi\eta[2\theta_0 + \sin(2\theta_0)]}{4\theta_0}\right]} = \frac{h_{24}^*}{h_{15}} = \frac{C_{44}\beta_{11} - h_{15}^2}{C_{44}\beta_{11}\left[1 + \frac{\pi\eta[2\theta_0 + \sin(2\theta_0)]}{4\theta_0}\right]^2 - h_{15}^2},$$

$$C_{45}^* = h_{14}^* = h_{25}^* = \beta_{12}^* = 0, \quad (48)$$

where $C_{44}\beta_{11} > h_{15}^2$. Apparently $C_{44}^*, C_{55}^*, \beta_{11}^*, \beta_{22}^* > 0$ and $C_{55}^*\beta_{11}^* > h_{15}^{*2}, C_{44}^*\beta_{22}^* > h_{24}^{*2}$.

For a hexagonal piezoelectric solid with its poling direction along the x_2-axis, it follows from Eq. 46 that the effective electroelastic properties of the microcracked, piezoelectric solid pertaining to the in-plane deformation and in-plane electric fields can be explicitly given by

$$\begin{bmatrix} C_{11}^* & C_{12}^* & h_{21}^* \\ C_{12}^* & C_{22}^* & h_{22}^* \\ h_{21}^* & h_{22}^* & -\beta_{22}^* \end{bmatrix}^{-1} = \begin{bmatrix} C_{11} & C_{12} & h_{21} \\ C_{12} & C_{22} & h_{22} \\ h_{21} & h_{22} & -\beta_{22} \end{bmatrix}^{-1} + \frac{\pi\eta\,[2\theta_0 - \sin(2\theta_0)]}{4\theta_0}\begin{bmatrix} S_1 & 0 & -d \\ 0 & 0 & 0 \\ -d & 0 & \epsilon \end{bmatrix} + \frac{\pi\eta\,[2\theta_0 + \sin(2\theta_0)]}{4\theta_0}\begin{bmatrix} 0 & 0 & 0 \\ 0 & S_3 & 0 \\ 0 & 0 & 0 \end{bmatrix},$$

$$\begin{bmatrix} C_{66}^* & h_{16}^* \\ h_{16}^* & -\beta_{11}^* \end{bmatrix}^{-1} = \begin{bmatrix} C_{66} & h_{16} \\ h_{16} & -\beta_{11} \end{bmatrix}^{-1}$$

$$+\frac{\pi\eta\,[2\theta_0-\sin(2\theta_0)]}{4\theta_0}\begin{bmatrix}S_3 & 0\\ 0 & 0\end{bmatrix}$$
$$+\frac{\pi\eta\,[2\theta_0+\sin(2\theta_0)]}{4\theta_0}\begin{bmatrix}S_1 & d\\ d & \epsilon\end{bmatrix},$$
$$C^*_{16}=C^*_{26}=h^*_{11}=h^*_{12}=h^*_{26}=\beta^*_{12}=0, \quad (49)$$

where

$$\mathrm{Re}\,\{\mathbf{Y}\}=\begin{bmatrix}S_1 & 0 & d\\ 0 & S_3 & 0\\ d & 0 & \epsilon\end{bmatrix}, \quad (50)$$

has been defined by Suo (1993). Similar to the case of insulating cracks, the elements in Eq. 50 have to be computed numerically. Apparently both $\begin{bmatrix}C^*_{11} & C^*_{12} & h^*_{21}\\ C^*_{12} & C^*_{22} & h^*_{22}\\ h^*_{21} & h^*_{22} & \beta^*_{22}\end{bmatrix}$ and $\begin{bmatrix}C^*_{66} & h^*_{16}\\ h^*_{16} & \beta^*_{11}\end{bmatrix}$ are positive definite.

3.4 A special distribution of the insulating microcracks

Next we discuss a special distribution of the microcracks: all the insulating microcracks with common half-length a are distributed along the x_1-axis in a homogeneous piezoelectric solid subjected to the homogeneous stresses σ^0_{ij} and the homogeneous electric displacements D^0_i. As pointed out by Fan and Sze (2001), we may merge the microcracks along the x_1-axis into a continuously damaged interface such that

$$\langle\tilde{\mathbf{t}}_2\rangle=\tilde{\mathbf{k}}\langle[\tilde{\mathbf{u}}]\rangle, \quad \text{on} \quad x_2=0 \quad (51)$$

where $\langle*\rangle$ stands for the average over an area of a scale much greater than the dimension of the microcracks, $\tilde{\mathbf{t}}_2=[\sigma_{12}\ \ \sigma_{22}\ \ \sigma_{32}\ \ D_2]^T$ and $[\tilde{\mathbf{u}}]$ being defined by Eq. 24. In addition $\langle\tilde{\mathbf{t}}_2\rangle=\tilde{\mathbf{t}}^0_2=\left[\sigma^0_{12}\ \ \sigma^0_{22}\ \ \sigma^0_{32}\ \ D^0_2\right]^T$. Equation 51 can be termed the generalized, spring-type, imperfect interface model with the 4×4 symmetric matrix $\tilde{\mathbf{k}}$ being the generalized stiffness matrix to be determined. When ignoring the crack interactions and noticing Eqs. 12 and 28 with $\theta=0$, we can easily obtain the following

$$\langle[\tilde{\mathbf{u}}]\rangle=\frac{\pi a\rho}{2}\tilde{\mathbf{L}}^{-1}\tilde{\mathbf{t}}^0_2, \quad (52)$$

where $\rho=Ma/L$ with M being the number of microcracks within the sample of half-length L taken out of the x_1-axis. Comparison of Eq. 52 with Eq. 51 will immediately lead to the following closed-form expression of $\tilde{\mathbf{k}}$ as

$$\tilde{\mathbf{k}}=\frac{2}{\pi a\rho}\tilde{\mathbf{L}}, \quad (53)$$

which remains valid when $\rho\ll1$. We see from the above expression that the structure of $\tilde{\mathbf{k}}$ is exactly the same as that of $\tilde{\mathbf{L}}$ described in Eq. 29.

3.4.1 Remark

Fan and Sze (2001) derived a closed-form expression in (2.9) for the spring constant k for two-dimensional non-interacting cracks. In fact, the expression for k in three-dimensions for penny-shaped, non-interacting cracks can also be similarly derived as

$$k=\frac{3\pi C}{8a}\frac{1}{\rho^2}, \quad (54)$$

which matches quite well the finite element results in Table 2 in Fan and Sze (2001) up to $\rho=0.5$.

4 An approximation of the GSCM

We point out that the problem in Sect. 2 can also be discussed within the framework of the generalized self-consistent method (GSCM), which approximately takes into account crack interaction (Aboudi and Benveniste 1987; Santare et al. 1995). Here we can adopt a simplified version of the GSCM for a microcracked, elastically anisotropic solid: first calculate the uniform stress field $\tilde{\sigma}^0_{ij}$ within an intact *circular* inclusion with undamaged material properties surrounded by the effective medium with (unknown) material properties subjected to remote uniform stresses σ^0_{ij} (Ting 1996); second solve the problem of a crack in an infinite homogeneous material with undamaged material properties subjected to remote uniform loading $\tilde{\sigma}^0_{ij}$ obtained in step 1. After adopting the above, simplified version of the GSCM, the crack opening displacement can be finally obtained as

$$[\mathbf{u}]=2\sqrt{a^2-x^2}\mathbf{L}^{-1}\tilde{\mathbf{t}}, \quad (|x|\le a) \quad (55)$$

where

$$\tilde{\mathbf{t}}=\mathbf{L}(\mathbf{E}_1\mathbf{t}^0_1+\mathbf{E}_2\mathbf{t}^0_2)\cos\theta-\mathbf{L}(\mathbf{F}_1\mathbf{t}^0_1+\mathbf{F}_2\mathbf{t}^0_2)\sin\theta, \quad (56)$$

with

$$\begin{aligned}&\mathbf{t}^0_1=[\sigma^0_{11}\ \ \sigma^0_{21}\ \ \sigma^0_{31}]^T,\\ &\mathbf{t}^0_2=[\sigma^0_{12}\ \ \sigma^0_{22}\ \ \sigma^0_{32}]^T,\\ &[\mathbf{E}_1\ \ \mathbf{E}_2]=\mathbf{L}^{-1}[\mathbf{0}_{3\times3}\ \ \mathbf{I}_{3\times3}](\tilde{\mathbf{N}}^*+\mathbf{N})^{-1}\\ &\times(\tilde{\mathbf{N}}^*+\mathbf{N}^*)\begin{bmatrix}\mathbf{q}_2 & \mathbf{q}_2\mathbf{N}^{*T}_1\\ \mathbf{0}_{3\times3} & \mathbf{I}_{3\times3}\end{bmatrix},\end{aligned} \quad (57)$$

$$[\mathbf{F}_1 \quad \mathbf{F}_2] = -\mathbf{L}^{-1}[\mathbf{N}_3 \quad \mathbf{N}_1^T](\tilde{\mathbf{N}}^* + \mathbf{N})^{-1} \times (\tilde{\mathbf{N}}^* + \mathbf{N}^*) \begin{bmatrix} \mathbf{q}_2 & \mathbf{q}_2\mathbf{N}_1^{*T} \\ \mathbf{0}_{3\times3} & \mathbf{I}_{3\times3} \end{bmatrix}, \tag{58}$$

and

$$\mathbf{N} = \begin{bmatrix} \mathbf{N}_1 & \mathbf{N}_2 \\ \mathbf{N}_3 & \mathbf{N}_1^T \end{bmatrix}, \quad \tilde{\mathbf{N}} = \begin{bmatrix} \mathbf{S} & \mathbf{H} \\ -\mathbf{L} & \mathbf{S}^T \end{bmatrix}, \tag{59}$$

$$\mathbf{q}_2 = \begin{bmatrix} S'^*_{11} & 0 & S'^*_{15} \\ 0 & 0 & 0 \\ S'^*_{15} & 0 & S'^*_{55} \end{bmatrix}. \tag{60}$$

In the above expressions the quantities attached with the superscript * are those pertaining to the effective medium. Here we point out that the above derivations are based on the elliptic inclusion and crack solutions in Ting (1996) and more detailed structures and identities of $\mathbf{N}_1, \mathbf{N}_2, \mathbf{N}_3, \mathbf{S}, \mathbf{H}$ and $\mathbf{L}$, all of which can be explicitly expressed in terms of the reduced elastic compliances, can be found in Chapter 6 of Ting (1996). The Barnett–Lothe tensor, $\mathbf{S}$, should not be confused with the elastic compliance. It can be easily verified from the above expressions that $\tilde{\mathbf{t}} = \mathbf{t}_2^0 \cos\theta - \mathbf{t}_1^0 \sin\theta$ when the circular inclusion and the surrounding matrix possess exactly the same material properties. Substituting the above results into the energy balance expression, Eq. 3, we finally arrive at the following set of fifteen coupled, nonlinear equations for the fifteen unknown effective reduced elastic compliances:

$$\begin{aligned}
S'^*_{11} &= S'_{11} + \frac{\pi\eta F^{(1)}_{11}}{4\theta_0}\left[2\theta_0 - \sin(2\theta_0)\right], \\
S'^*_{22} &= S'_{22} + \frac{\pi\eta E^{(2)}_{22}}{4\theta_0}\left[2\theta_0 + \sin(2\theta_0)\right], \\
S'^*_{44} &= S'_{44} + \frac{\pi\eta E^{(2)}_{33}}{4\theta_0}\left[2\theta_0 + \sin(2\theta_0)\right], \\
S'^*_{55} &= S'_{55} + \frac{\pi\eta F^{(1)}_{33}}{4\theta_0}\left[2\theta_0 - \sin(2\theta_0)\right], \\
S'^*_{66} &= S'_{66} + \frac{\pi\eta}{4\theta_0}\left\{\left(E^{(1)}_{12} + E^{(2)}_{11}\right)\left[2\theta_0 + \sin(2\theta_0)\right] + \left(F^{(1)}_{22} + F^{(2)}_{21}\right)\left[2\theta_0 - \sin(2\theta_0)\right]\right\}, \\
S'^*_{12} &= S'_{12} + \frac{\pi\eta}{8\theta_0} \times \left\{E^{(1)}_{21}\left[2\theta_0 + \sin(2\theta_0)\right] + F^{(2)}_{12}\left[2\theta_0 - \sin(2\theta_0)\right]\right\}, \\
S'^*_{14} &= S'_{14} + \frac{\pi\eta}{8\theta_0} \times \left\{E^{(1)}_{31}\left[2\theta_0 + \sin(2\theta_0)\right] + F^{(2)}_{13}\left[2\theta_0 - \sin(2\theta_0)\right]\right\},
\end{aligned} \tag{61}$$

$$\begin{aligned}
S'^*_{15} &= S'_{15} + \frac{\pi\eta(F^{(1)}_{13} + F^{(1)}_{31})}{8\theta_0}\left[2\theta_0 - \sin(2\theta_0)\right], \\
S'^*_{16} &= S'_{16} + \frac{\pi\eta}{8\theta_0}\left\{E^{(1)}_{11}\left[2\theta_0 + \sin(2\theta_0)\right] + \left(F^{(1)}_{12} + F^{(1)}_{21} + F^{(2)}_{11}\right)\left[2\theta_0 - \sin(2\theta_0)\right]\right\},
\end{aligned} \tag{62}$$

$$\begin{aligned}
S'^*_{24} &= S'_{24} + \frac{\pi\eta\left(E^{(2)}_{23} + E^{(2)}_{32}\right)}{8\theta_0}\left[2\theta_0 + \sin(2\theta_0)\right], \\
S'^*_{25} &= S'_{25} + \frac{\pi\eta}{8\theta_0}\left\{E^{(1)}_{23}\left[2\theta_0 + \sin(2\theta_0)\right] + F^{(2)}_{32}\left[2\theta_0 - \sin(2\theta_0)\right]\right\}, \\
S'^*_{26} &= S'_{26} + \frac{\pi\eta}{8\theta_0}\left\{\left(E^{(1)}_{22} + E^{(2)}_{12} + E^{(2)}_{21}\right)\left[2\theta_0 + \sin(2\theta_0)\right] + F^{(2)}_{22}\left[2\theta_0 - \sin(2\theta_0)\right]\right\}, \\
S'^*_{45} &= S'_{45} + \frac{\pi\eta}{8\theta_0}\left\{E^{(1)}_{33}\left[2\theta_0 + \sin(2\theta_0)\right] + F^{(2)}_{33}\left[2\theta_0 - \sin(2\theta_0)\right]\right\}, \\
S'^*_{46} &= S'_{46} + \frac{\pi\eta}{8\theta_0}\left\{\left(E^{(1)}_{32} + E^{(2)}_{13} + E^{(2)}_{31}\right)\left[2\theta_0 + \sin(2\theta_0)\right] + F^{(2)}_{23}\left[2\theta_0 - \sin(2\theta_0)\right]\right\}, \\
S'^*_{56} &= S'_{56} + \frac{\pi\eta}{8\theta_0}\left\{E^{(1)}_{13}\left[2\theta_0 + \sin(2\theta_0)\right] + \left(F^{(1)}_{23} + F^{(1)}_{32} + F^{(2)}_{31}\right)\left[2\theta_0 - \sin(2\theta_0)\right]\right\},
\end{aligned} \tag{63}$$

where $E^{(1)}_{ij}$, $E^{(2)}_{ij}$, $F^{(1)}_{ij}$ and $F^{(2)}_{ij}$, all of which are functions of the unknown effective reduced elastic compliances, are the components of four 3×3 matrices $\mathbf{E}_1, \mathbf{E}_2, \mathbf{F}_1$ and $\mathbf{F}_2$ respectively.

Equations 61–63 can be solved through iteration (Santare et al. 1995; Wang et al. 2009). During specific iteration for the unknowns, it is more convenient to adopt the following equivalent matrix expression

$$\begin{aligned}
\mathbf{S}'^* = \mathbf{S}' &+ \frac{\pi\eta\left[2\theta_0 + \sin(2\theta_0)\right]}{8\theta_0} \times \left[\mathbf{J}_2^T\begin{bmatrix}\mathbf{E}_1 & \mathbf{E}_2\end{bmatrix}\begin{bmatrix}\mathbf{J}_1 \\ \mathbf{J}_2\end{bmatrix} + \begin{bmatrix}\mathbf{J}_1^T & \mathbf{J}_2^T\end{bmatrix}\begin{bmatrix}\mathbf{E}_1^T \\ \mathbf{E}_2^T\end{bmatrix}\mathbf{J}_2\right] \\
&+ \frac{\pi\eta\left[2\theta_0 - \sin(2\theta_0)\right]}{8\theta_0} \times \left[\mathbf{J}_1^T\begin{bmatrix}\mathbf{F}_1 & \mathbf{F}_2\end{bmatrix}\begin{bmatrix}\mathbf{J}_1 \\ \mathbf{J}_2\end{bmatrix} + \begin{bmatrix}\mathbf{J}_1^T & \mathbf{J}_2^T\end{bmatrix}\begin{bmatrix}\mathbf{F}_1^T \\ \mathbf{F}_2^T\end{bmatrix}\mathbf{J}_1\right],
\end{aligned} \tag{64}$$

where

$$\mathbf{J}_1=\begin{bmatrix}1&0&0&0&0\\0&0&0&0&1\\0&0&0&1&0\end{bmatrix},\quad \mathbf{J}_2=\begin{bmatrix}0&0&0&0&1\\0&1&0&0&0\\0&0&1&0&0\end{bmatrix}. \tag{65}$$

We observe that when using the GSCM, the fifteen effective, reduced elastic compliances will, in general, be different from the corresponding compliances for the undamaged material. Thus the result that $S'^{*}_{12} = S'_{12}, S'^{*}_{14} = S'_{14}, S'^{*}_{25} = S'_{25}, S'^{*}_{45} = S'_{45}$ (see Eq. 14) is only valid for NIA.

5 Effective thermal conductivities of a solid containing insulated penny-shaped cracks

In the above, the crack orientation distribution function $\phi(\theta)$ has been introduced for two-dimensional cracks. In fact, the crack orientation distribution function can also be adopted to describe three-dimensional cracks. As an illustration, we consider the effective thermal conductivities of a solid containing insulated penny-shaped cracks with an arbitrary degree of alignment. Within the framework of steady-state heat conduction, we consider insulated penny-shaped cracks of radius a with an arbitrary degree of alignment, distributed in a homogeneous and isotropic medium with thermal conductivity κ. The orientation of the penny-shaped crack can be described by the azimuth angle θ ($|\theta| \le \pi/2$) and the zenith angle ϕ ($0 \le \phi \le \pi$) which define the direction of the unit normal of the crack surface as shown in Fig. 8 (Yang and Turner 2003). The crack orientation distribution function $\phi(\theta, \phi)$ on a unit sphere can be given by

$$\phi(\theta,\varphi) = \begin{cases} \dfrac{1}{4\theta_0 \sin\varphi_0}, & |\theta| \le \theta_0 \text{ and } \frac{\pi}{2}-\varphi_0 \le \varphi \le \frac{\pi}{2}+\varphi_0 \\ 0, & \text{else} \end{cases} \tag{66}$$

where $\theta_0, \varphi_0 \le \pi/2$. By adopting the energy method and ignoring the crack interactions, closed-form expressions for the effective thermal conductivities can be derived as

$$\kappa^*_{11} = \frac{\kappa}{1+\frac{2\eta[2\theta_0+\sin(2\theta_0)]}{3\theta_0}\left(1-\frac{\sin^2\varphi_0}{3}\right)},$$

$$\kappa^*_{22} = \frac{\kappa}{1+\frac{2\eta[2\theta_0-\sin(2\theta_0)]}{3\theta_0}\left(1-\frac{\sin^2\varphi_0}{3}\right)},$$

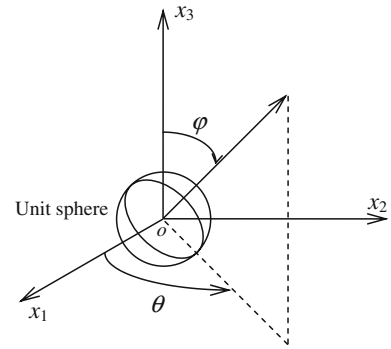

Fig. 8 Geometry of a penny-shaped crack

$$\kappa^*_{33} = \frac{\kappa}{1+\frac{8\eta\sin^2\varphi_0}{9}}, \tag{67}$$

where $\eta = Ma^3/V$ is the crack density parameter and $\kappa^*_{ij} = 0, (i \ne j)$, which implies that the three principal directions of the effective medium are along the x_1, x_2 and x_3 axes. The above derivation uses the following expression for the temperature jump $[T]$ across the insulated crack surfaces (Barber 1975)

$$[T] = -\frac{4q_0\sqrt{a^2-r^2}}{\pi\kappa}, \quad (0 \le r \le a) \tag{68}$$

where q_0 is the uniform heat flow prescribed on the crack face.

If all the microcracks are randomly oriented, i.e., $\varphi_0 = \theta_0 = \pi/2$, then we have

$$\kappa^*_{11} = \kappa^*_{22} = \kappa^*_{33} = \frac{\kappa}{1+\frac{8}{9}\eta}, \tag{69}$$

which means that the effective property is still isotropic.

If the unit normals of all the microcracks lie in the $x_1 - x_2$ plane, i.e., $\varphi_0 = 0$, then we have

$$\kappa^*_{11} = \frac{\kappa}{1+\frac{2\eta[2\theta_0+\sin(2\theta_0)]}{3\theta_0}},$$

$$\kappa^*_{22} = \frac{\kappa}{1+\frac{2\eta[2\theta_0-\sin(2\theta_0)]}{3\theta_0}},$$

$$\kappa^*_{33} = \kappa, \tag{70}$$

which indicates that the effective thermal conductivity κ^*_{33} is not influenced by the existence of the microcracks. Furthermore, if the unit normals, which lie in the $x_1 - x_2$ plane, have a random distribution, i.e., $\theta_0 = \pi/2$ (or the so called uniaxially aligned cracks, see Yang and Turner 2003), then it follows from Eq. 70 that

$$\kappa^*_{11} = \kappa^*_{22} = \frac{\kappa}{1+\frac{4}{3}\eta}, \quad \kappa^*_{33} = \kappa, \tag{71}$$

which indicates that the effective property is transversely isotropic with the x_3-axis taken as the uniaxial symmetry axis. Alternatively, if the unit normals lying in the $x_1 - x_2$ plane are along the x_1-axis, i.e., $\theta_0 = 0$ (i.e, the so-called perfectly aligned cracks, see Yang and Turner 2005), then it follows from Eq. 70 that

$$\kappa_{11}^* = \frac{\kappa}{1 + \frac{8}{3}\eta}, \quad \kappa_{22}^* = \kappa_{33}^* = \kappa, \tag{72}$$

which indicates that the effective property is also transversely isotropic, but now with the x_1-axis as the uniaxial symmetry axis.

6 Conclusions

We first derived in Eq. 14 the closed-form expressions for the fifteen effective reduced elastic compliances of a microcracked, elastically anisotropic solid by using NIA. Then we further obtained in Eqs. 30, 35 and 46 the concise expressions for the effective electroelastic properties of a piezoelectric solid containing insulating, permeable or conducting microcracks by extending the NIA for purely elastic materials. We also derived a set of coupled nonlinear Eq. 64 for the unknown effective reduced elastic compliances by using the GSCM. Finally the crack orientation distribution function was introduced to investigate the effective thermal conductivities of a solid containing insulated penny-shaped cracks with an arbitrary degree of alignment, and the effective thermal conductivities were derived in Eq. 67.

Acknowledgement The authors wish to thank the two referees for their comments and suggestions on revising the initial manuscript. This research was supported by the United States Army Research Laboratory through the Composite Materials Technology cooperative agreement with the Center for Composite Materials at the University of Delaware.

References

Aboudi J, Benveniste Y (1987) The effective moduli of cracked bodies in plane deformations. Eng Fract Mech 26(2):171–184. doi:10.1016/0013-7944(87)90195-0

Barber JR (1975) Steady-state thermal stresses in an elastic solid containing an insulated penny-shaped crack. J Strain Anal 10(1):19–24. doi:10.1243/03093247V101019

Benveniste Y (1985) The effective mechanical behavior of composite materials with imperfect contact between the constituents. Mech Mater 4(2):197–208. doi:10.1016/0167-6636(85)90016-X

Bristow JR (1960) Microcracks, and the static and dynamic elastic constants of annealed heavily cold-worked metals. Br J Appl Phys 11:81–85. doi:10.1088/0508-3443/11/2/309

Eshelby JD (1956) The continuum theory of lattice defects. In: Seitz F, Turnbull D (eds) Progress in solid state physics. Academic Press, New York p 79

Fan H, Sze KY (2001) A micro-mechanics model for imperfect interface in dielectric materials. Mech Mater 33:363–370. doi:10.1016/S0167-6636(01)00053-9

Feltman RS, Santare MH (1999) Anisotropic effective moduli of cracked short fiber reinforced composites. ASME J Appl Mech 66:709–713

Gottesman T, Hashin Z, Brull MA (1980) Effective elastic moduli of cracked fiber composites. In: Bunsell et al (ed) Advance in composites materials. Pergamon Press, Oxford pp 749–758

Hashin Z (1988) The differential scheme and its application to cracked materials. J Mech Phys Solids 36:719–734. doi:10.1016/0022-5096(88)90005-1

Kachanov M (1992) Effective elastic properties of cracked solids: critical review of some basic concepts. Appl Mech Rev 45(8):305–336. doi:10.1115/1.3119761

Kachanov M (2007) On the effective elastic properties of cracked solids—editor's comments. Int J Fract 146:295–299. doi:10.1007/s10704-007-9170-6

Mauge C, Kachanov M (1994) Effective elastic properties of an anisotropic material with arbitrarily oriented interacting cracks. J Mech Phys Solids 42(4):561–584. doi:10.1016/0022-5096(94)90052-3

McMeeking RM (1987) On mechanical stresses at cracks in dielectrics with application to dielectric-breakdown. J Appl Phys 62(8):3116–3122. doi:10.1063/1.339361

Pak YE (1990) Crack extension force in a piezoelectric material. ASME J Appl Mech 57:647–653

Pan E (2001) Exact solution for simply supported and multilayered magneto-electro-elastic plates. ASME J Appl Mech 68:608–618

Santare MH, Crocombe AD, Anlas G (1995) Anisotropic effective moduli of materials with microcracks. Eng Fract Mech 52(5):833–842. doi:10.1016/0013-7944(95)00059-5

Suo Z (1990) Singularities, interfaces and cracks in dissimilar anisotropic materials. Proc R Soc Lond A Math Phys Sci 427:331–358. doi:10.1098/rspa.1990.0016

Suo Z (1993) Models for breakdown-resistant dielectric and ferroelectric ceramics. J Mech Phys Solids 41:1155–1176. doi:10.1016/0022-5096(93)90088-W

Suo Z, Kuo CM, Barnett DM, Willis JR (1992) Fracture mechanics for piezoelectric ceramics. J Mech Phys Solids 40:739–765. doi:10.1016/0022-5096(92)90002-J

Ting TCT (1996) Anisotropic elasticity-theory and applications. Oxford University Press, New York

Wang X, Santare MH, Gazonas GA (2009) Anisotropic effective moduli of microcracked materials under antiplane loading. Eng Fract Mech (in press)

Yang LY, Turner JA (2003) Elastic wave propagation and scattering in solids with uniaxially aligned cracks. J Acoust Soc Am 114(2):591–600. doi:10.1121/1.1592158

Yang LY, Turner JA (2005) Wave attenuations in solids with perfectly aligned cracks. Acoust Res Lett Online 6(2):99–105. doi:10.1121/1.1861092

NO. OF
COPIES ORGANIZATION

1 (PDF only) DEFENSE TECHNICAL INFORMATION CTR
DTIC OCA
8725 JOHN J KINGMAN RD
STE 0944
FORT BELVOIR VA 22060-6218

1 DIRECTOR
US ARMY RESEARCH LAB
IMNE ALC HRR
2800 POWDER MILL RD
ADELPHI MD 20783-1197

1 DIRECTOR
US ARMY RESEARCH LAB
RDRL CIM L
2800 POWDER MILL RD
ADELPHI MD 20783-1197

1 DIRECTOR
US ARMY RESEARCH LAB
RDRL CIM P
2800 POWDER MILL RD
ADELPHI MD 20783-1197

ABERDEEN PROVING GROUND

1 DIR USARL
RDRL CIM G (BLDG 4600)

NO. OF COPIES	ORGANIZATION
1 (CD only)	DPTY ASSIST SCT FOR R&T SARD TT ASA (ACT) J PARMENTOLA THE PENTAGON RM 3E479 WASHINGTON DC 20310-1714
1	PRIN DPTY FOR TCHNLGY HQ US ARMY MATCOM AMCDCGR R PRICE 9301 CHAPEK RD FT BELVOIR VA 22060-5527
3	AIR FORCE ARMAMENT LAB AFATL DLJW W COOK D BELK J FOSTER EGLIN AFB FL 32542
2	NSF S MCKNIGHT G PAULINO 4201 WILSON BLVD STE 545 ARLINGTON VA 22230-0002
1	DARPA W COBLENZ 3701 N FAIRFAX DR ARLINGTON VA 22203-1714
1	DIRECTOR US ARMY ARDEC AMSRD AAR AEE W E BAKER BLDG 3022 PICATINNY ARSENAL NJ 07806-5000
2	US ARMY TARDEC AMSTRA TR R MS 263 K BISHNOI D TEMPLETON MS 263 WARREN MI 48397-5000
1	COMMANDER US ARMY RSRCH OFC AMSRD ARL RO EN B LAMATTINA PO BOX 12211 RESEARCH TRIANGLE PARK NC 27709-2211

NO. OF COPIES	ORGANIZATION
1	COMMANDER US ARMY RSRCH OFC AMSRD ARL RO MM J LAVERY PO BOX 12211 RESEARCH TRIANGLE PARK NC 27709-2211
1	COMMANDER US ARMY RSRCH OFC AMSRD ARL RO EM D STEPP PO BOX 12211 RESEARCH TRIANGLE PARK NC 27709-2211
5	NAVAL RESEARCH LAB E R FRANCHI CODE 7100 M H ORR CODE 7120 J A BUCARO CODE 7130 J S PERKINS CODE 7140 S A CHIN BING CODE 7180 4555 OVERLOOK AVE SW WASHINGTON DC 20375
1	DTRA M GILTRUD 8725 JOHN J KINGMAN RD FORT BELVOIR VA 22060
1	ERDC US ARMY CORPS OF ENGRS USACEGSL P PAPADOS 7701 TELEGRAPH RD ALEXANDRIA VA 22315
1	AFOSR NL F FAHROO 875 N RANDOLPH ST STE 325 RM 3112 ARLINGTON VA 22203
1	CLEMSON UNIV DEPT MECH ENGR M GRUJICIC 241 ENGRG INNOVATION BLDG CLEMSON SC 29634-0921
1	UNIV OF CALIFORNIA CTR OF EXCELLENCE FOR ADV MATLS S NEMAT NASSER SAN DIEGO CA 92093-0416

NO. OF COPIES ORGANIZATION

5 DIRECTOR
LANL
P MAUDLIN
R GRAY
W R THISSELL
A ZUREK
F ADDESSIO
PO BOX 1663
LOS ALAMOS NM 87545

7 DIRECTOR
SANDIA NATL LABS
J BISHOP MS 0346
E S HERTEL JR MS 0382
W REINHART MS 1181
T VOGLER MS 1181
L CHHABILDAS MS 1811
M FURNISH MS 1168
M KIPP MS 0378
PO BOX 5800
ALBUQUERQUE NM 87185-0307

1 DIRECTOR
LLNL
M J MURPHY
PO BOX 808
LIVERMORE CA 94550

3 CALTECH
M ORTIZ MS 105 50
G RAVICHANDRAN
T J AHRENS MS 252 21
1201 E CALIFORNIA BLVD
PASADENA CA 91125

5 SOUTHWEST RSRCH INST
C ANDERSON
K DANNEMANN
T HOLMQUIST
G JOHNSON
J WALKER
PO DRAWER 28510
SAN ANTONIO TX 78284

1 TEXAS A&M UNIV
DEPT OF MATH
J WALTON
COLLEGE STATION TX 77843

1 WORCESTER POLYTECHNIC INST
MATHEMATICAL SCI
K LURIE
WORCESTER MA 01609

NO. OF COPIES ORGANIZATION

2 SRI INTERNATIONAL
D CURRAN
D SHOCKEY
333 RAVENSWOOD AVE
MENLO PARK CA 94025

1 VIRGINIA POLYTECHNIC INST
COLLEGE OF ENGRG
R BATRA
BLACKSBURG VA 24061-0219

8 UNIV OF NEBRASKA
DEPT OF ENGRG MECH
D ALLEN
F BOBARU
Y DZENIS
G GOGOS
M NEGAHBAN
R FENG
J TURNER
Z ZHANG
LINCOLN NE 68588

1 JOHNS HOPKINS UNIV
DEPT OF MECH ENGRG
K T RAMESH
LATROBE 122
BALTIMORE MD 21218

4 UNIV OF UTAH
DEPT OF MATH
A CHERKAEV
E CHERKAEV
E S FOLIAS
R BRANNON
SALT LAKE CITY UT 84112

1 PENN STATE UNIV
DEPT OF ENGRG SCI & MECH
F COSTANZO
UNIVERSITY PARK PA 168023

3 UNIV OF DELAWARE
DEPT OF MECH ENGRG
T BUCHANAN
T W CHOU
M SANTARE
126 SPENCER LAB
NEWARK DE 19716

1 UNIV OF DELAWARE
CTR FOR COMPST MATRLS
J GILLESPIE
NEWARK DE 19716

NO. OF COPIES	ORGANIZATION
1	COMPUTATIONAL MECH CONSULTANTS J A ZUKAS PO BOX 11314 BALTIMORE MD 21239-0314
1	LOUISIANA STATE UNIV R LIPTON 304 LOCKETT HALL BATON ROUGE LA 70803-4918
1	INST OF ADVANCED TECH UNIV OF TX AUSTIN S BLESS 3925 W BRAKER LN STE 400 AUSTIN TX 78759-5316
1	APPLIED RSCH ASSOC D E GRADY 4300 SAN MATEO BLVD NE STE A220 ALBUQUERQUE NM 87110
1	INTERNATIONAL RSRCH ASSOC INC D L ORPHAL 4450 BLACK AVE PLEASANTON CA 94566
3	ORNL ENVIRONMENTAL SCI DIV W DOLL T GAMEY L BEARD PO BOX 2008 OAK RIDGE TN 37831
1	UNIV OF ILLINOIS DEPT OF MECHL SCI & ENGRG A F VAKAKIS 1206 W GREEN ST MC 244 URBANA CHAMPAIGN IL 61801
1	UNIV OF ILLINOIS ARSPC ENGRG J LAMBROS 104 S WRIGHT ST MC 236 URBANA CHAMPAIGN IL 61801
2	WASHINGTON ST UNIV INST OF SHOCK PHYSICS Y M GUPTA J ASAY PULLMAN WA 99164-2814

NO. OF COPIES	ORGANIZATION
1	NORTHWESTERN UNIV DEPT OF CIVIL & ENVIRON ENGRG Z BAZANT 2145 SHERIDAN RD A135 EVANSTON IL 60208-3109
1	UNIV OF DAYTON RSRCH INST N S BRAR 300 COLLEGE PARK MS SPC 1911 DAYTON OH 45469
2	TEXAS A&M UNIV DEPT OF GEOPHYSICS MS 3115 F CHESTER T GANGI COLLEGE STATION TX 778431
1	UNIV OF SAN DIEGO DEPT OF MATH & CMPTR SCI A VELO 5998 ALCALA PARK SAN DIEGO CA 92110
1	NATIONAL INST OF STANDARDS & TECHLGY BLDG & FIRE RSRCH LAB J MAIN 100 BUREAU DR MS 8611 GAITHERSBURG MD 20899-8611
1	MIT DEPT ARNTCS ASTRNTCS R RADOVITZKY 77 MASSACHUSETTS AVE CAMBRIDGE MA 02139
1	UNIV OF DELAWARE DEPT ELECTRICAL & CMPTR ENGRG D WEILE NEWARK DE 19716
3	DIR USARL RDRL D V WEISS RDRL SE J PELLEGRINO RDRL SES P A EDELSTEIN 2800 POWDER MILL RD ADELPHI MD 20783-1197

NO. OF
COPIES ORGANIZATION

2 MATERIALS SCI CORP
A CAIAZZO
R LAVERTY
181 GIBRALTAR RD
HORSHAM PA 19044

1 UNIV OF MISSISSIPPI
DEPT OF MECH ENGRG
A M RAJENDRAN
201 B CARRIER HALL
UNIVERSITY MS 38677

ABERDEEN PROVING GROUND

67 DIR USARL
RDRL WM
B FORCH
S KARNA
J MCCAULEY
P PLOSTINS
J SMITH
RDRL WML
J NEWILL
M ZOLTOSKI
RDRL WML B
I BATYREV
B RICE
N WEINGARTEN
RDRL WML D
P CONROY
M NUSCA
RDRL WML G
J ANDZELM
M BERMAN
W DRYSDALE
A RAWLETT
RDRL WML H
D SCHEFFLER
S SCHRAML
B SCHUSTER
RDRL WMM
R DOWDING
J ZABINSKI
RDRL WMM A
M MAHER
J TZENG
E WETZEL
RDRL WMM B
T BOGETTI
B CHEESEMAN
C FOUNTZOULAS

NO. OF
COPIES ORGANIZATION

D HOPKINS
B POWERS
C RANDOW
M VANLANDINGHAM
R WILDMAN
C F YEN
RDRL WMM D
E CHIN
K CHO
R HOWELL
RDRL WMM E
M COLE
T JESSEN
J LASALVIA
J SANDS
RDRL WMM F
L KECSKES
S MATHAUDHU
RDRL WMP
P BAKER
S SCHOENFELD
RDRL WMP B
R BECKER
S BILYK
D CASEM
J CLAYTON
C HOPPEL
M GREENFIELD
R KRAFT
B LEAVY
B LOVE
M SCHEIDLER
T WEERASOORIYA
RDRL WMP C
T BJERKE
S SEGLETES
RDRL WMP D
R DONEY
J RUNYEON
B SCOTT
RDRL WMP E
M BURKINS
RDRL WMP F
M CHOWDHURY
A FRYDMAN
N GNIAZDOWSKI
R GUPTA
RDRL WMP G
D KOOKER
G R PEHRSON